COO-3130TC-30

The Determination of the Weak Neutral Current Coupling Constants and Limits on the Electromagnetic Properties of the Muon Neutrino

FERMILAB
APR 27 1987
LIBRARY

by
John Louis Callas
B.S., Tufts University, 1981
Sc.M., Brown University, 1983

Thesis

Submitted in partial fulfillment of the requirements for the
Degree of Doctor of Philosophy
in the Department of Physics at Brown University

May, 1987

In memory of

L. Johnson Callas

This dissertation by John Louis Callas
is accepted in its present form by the Department of
Physics as satisfying the
dissertation requirement for the degree of Doctor of Philosophy

1-29-87
Date

Robert E. Lanou, Jr.
Professor of Physics

Recommended to the Graduate Council

1-29-87
Date

Stavros Fallieros
Professor of Physics

Jan 29, 1987
Date

Mildred Widgoff
Professor of Physics

Approved by the Graduate Council

2/6/87
Date

Vita

The author was born 9 July 1959 in Newton, Massachusetts. After receiving his diploma from Wellesley Senior High School in 1977, the author attended Tufts University, School of Engineering where he received the degree of Bachelor of Science in 1981. While attending Tufts University, the author worked for three years as a research associate for the Department of Physics. The author then continued his education at Brown University where he received the degree of Master in Science in Physics in 1983 and the degree of Doctor of Philosophy in Physics in 1987. During his study at Brown University, the author work for one year as a teaching assistant and the remaining years as a research assistant.

Acknowledgments

It is always difficult to express appreciation to those who assisted one in a long and difficult journey. One finds that one's life is touched by so many in so many ways. Hopefully those not mentioned here will know my appreciation without words.

First, I would like to thank all our collaborators on E734 including the staff at BNL who made it possible for the experiment to be. I would especially like to thank Hywel White, Mike Murtagh, Fern Coyle, and Ted Erickson of BNL and Dave Hedin of SUNY for their assistance and advice. In addition, I would like to mention the late Phil Connolly. Phil not only showed me how to look for magnetic monopoles but he also introduced me to sailboat racing.

Next I would like to thank Takao Shinkawa, Jan Hoftun, Milind Diwan and Emy Tseng for their assistance in the many phases of the experiment. I would especially like to thank Stan Durkin of the University of Pennsylvania for his tremendous assistance and guidance on the difficult and extensive analysis which made this thesis possible.

Next of course, I would like to express my deep appreciation to my advisors, Dave Cutts and Bob Lanou. Advisors like parents are those who have given you far more than you could ever possibly return.

At this point, I want to express my deep appreciation to my friend and co-conspirator, Eric Stern. Eric became the first and last person to ask a question on anything. And willingly or not, he will always be that to me. Without Eric's help things would have been so much more difficult for me. I would also like to mention my friends, Bryce Morris and Vivian O'Dell, who gave me the support, assistance and friendship necessary for me to pull the whole thing off.

And finally, I would like to mention the taxpayers of the United States of America who bankrolled the whole show

. . . and my mother who gave me life.

This work is partially supported by the U.S. Department of Energy contract DEAC02–76ER03130.

Table of Contents

Chapter 1:

Introduction 1

1. Kinematics and Signature 2
2. The Cross Section 5
3. Electromagnetic Contributions 8
4. Experimental Goals 9

Chapter 2:

Experimental Apparatus 11

1. Neutrino Beam 11
2. Main Detector 23
3. Calorimeter System 26
4. PDT System 27
5. System Control 32
6. Calibrations 35
7. Test Beam 38

Chapter 3:

Data Reduction 43

1. NUE Production Program 44
2. The PDT Filter 45

Chapter 4:

The Electron Analysis 54

1. Eye Scan 54
2. Signal Analysis 57
3. Signal Extraction 71

4. Acceptances and Efficiencies 83

Chapter 5:

Normalization 89

Chapter 6:

Results and Conclusions 96

1. The Cross Section 97

2. The Ratio 103

3. Y-Distribution Fits 108

4. Electromagnetic Effects 112

5. Conclusion 119

Appendix 1:

Eyescan Rules 122

6. First Eyescan Rules 122

7. Second Eyescan Rules 123

Appendix 2:

Monte Carlo 125

References 126

List of Tables

Table 3.1 The electron analysis procedure 44

Table 4.3.1 $E - \theta^2$ fits 78

Table 4.4.1 Electron efficiency factors 88

Table 5.1 Quasi-elastic event selection 89

Table 5.2 Normalization background subtraction 92

Table 5.3 Normalization correction factors 93

Table 6.2.1 Systematic errors for the electron analysis 105

Table 6.3.1 Respective contributions from "flat" and "y" components . . . 112

Table 6.5.1 $\nu_\mu e \rightarrow \nu_\mu e$ cross section measurements 119

Table 6.5.2 $\bar{\nu}_\mu e \rightarrow \bar{\nu}_\mu e$ cross section measurements 119

Table 6.5.3 $\sin^2\theta_W$ determinations 119

Table 6.5.4 Upper bound determinations for the magnetic momnet 120

List of Figures

Fig. 1.1.1 Diagrams for $\nu_\mu e \rightarrow \nu_\mu e$ kinematics 3

Fig. 1.2.1 Cross sections and Ratio versus $\sin^2\theta_W$ 7

Fig. 2.1.1 The AGS at Brookhaven National Laboratory 12

Fig. 2.1.2 The AGS beam time structure 13

Fig. 2.1.3 The layout of the magnetic horn system 14

Fig. 2.1.4 Schematic of the horn current system 15

Fig. 2.1.5 Layout of the neutrino beam line at the AGS 16

Fig. 2.1.6 The measured ν_μ spectrum 19

Fig. 2.1.7 The measured $\bar{\nu}_\mu$ spectrum 20

Fig. 2.1.8 The measured spectra of the wrong helicity neutrinos 22

Fig. 2.1.9 The measured ν_e spectrum 24

Fig. 2.2.1 The E734 neutrino detector 25

Fig. 2.3.1 The PMT electronics 28

Fig. 2.4.1 Construction of the PDT assembly 29

Fig. 2.4.2 The PDT electronics 31

Fig. 2.5.1 The E734 data acquisition system 33

Fig. 2.7.1 Angular resolution for test beam electrons 40

Fig. 2.7.2 Energy resolution for test beam electrons 41

Fig. 3.2.1 An example of an electromagnetic shower 47

Fig. 3.2.2 Sample vertex track patterns 48

Fig. 3.2.3 Multiple Hit Criterion 52

Fig. 4.1.1 Display of a shower candidate from the eyescan 55

Fig. 4.2.1 Plot of the mean dE/dx values for the calorimeters over time . . . 58

Fig. 4.2.2 Distribution of event vertex positions 59

Fig. 4.2.3 Shower energy distribution 60

Fig. 4.2.4 Vertex energy 62

Fig. 4.2.5 Interactive display for shower angle determination 63

Fig. 4.2.6 Graphic event display of the "road" application 65

Fig. 4.2.7 Calorimeter dE/dx deposition after the vertex 67

Fig. 4.2.8 The average PDT dE/dx deposition after the vertex 68

Fig. 4.2.9 θ^2 for the final electron sample 69

Fig. 4.2.10 θ^2 for the final photon sample 70

Fig. 4.3.1 θ^2 distribution for the "stub" sample 72

Fig. 4.3.2 Monte Carlo π^0 events exhibiting the "slope" phenomenon 74

Fig. 4.3.3 θ^2 plot for the hadron enriched sample 76

Fig. 4.3.4 Monte Carlo θ^2 fit to the data 79

Fig. 4.3.5 Energy fit to the data 80

Fig. 4.3.6 Background θ^2 fit to the data 81

Fig. 4.3.7 Background energy fit to the data 82

Fig. 5.1 θ_μ for the normalization sample 90

Fig. 5.2 Systematic errors for the Nomalization 94

Fig. 6.1.1 The acceptance, $A_{210\to 2100}$, as a function of $\sin^2\theta_W$ 99

Fig. 6.1.2 68% confidence level plot of g_V v. g_A 101

Fig. 6.1.3 χ^2 plots for the fits to $\sin^2\theta_W$ 102

Fig. 6.2.1 The Ratio v. $\sin^2\theta_W$ 104

Fig. 6.2.2 68% confidence level plot of g_V v. g_A 107

Fig. 6.3.1 θ^2 distribution for the y dependent term 110

Fig. 6.3.2 θ^2 distribution for the y independent term 111

Fig. 6.3.3 θ^2 fit to the data in 60 bins 113

Fig. 6.3.4 68% confidence level plot of g_V v. g_A for the y dependence fit . 114

Fig. 6.4.1 Plot of χ^2 v. the square of the magnetic moment, f^2 116

Fig. 6.4.2 Plot of χ^2 v. charge radius, $< r^2 >$ 118

Chapter 1.

Introduction

In 1930, Pauli proposed the existence of the neutrino to explain the apparent non-conservation of energy observed in β decay reactions. Not until 1953, was the neutrino directly observed by inverse β decay in reactor experiments [1–2]. Since its proposal the neutrino and the weak interaction have been the subject of great interest for physicists. Fermi, in 1933, proposed the first weak interaction theory in the form of four fermi-type current-current Lagrangian in analogy to electrodynamics. This theory was successful in describing low energy weak interactions. However at energies above 300 GeV, the theory violated unitarity and was not renormalizable. The existence of a massive intermediate vector boson which would mediate the weak interaction was proposed in an attempt to correct the unitary problems of the Fermi current-current theory.

In the 1960's, Weinberg [3], Salam [4], and Glashow [5] proposed the $SU(2)_L \times U(1)$ gauge theory of leptons which unified the electromagnetic and weak interactions into a single Yang-Mills gauge theory. This theory, known as the Standard Model, circumvented the previous problems of unitarity and was shown by t'Hooft in 1971 to be renormalizable [6]. It has proven to be successful in explaining all known weak processes. The remaining dissimilarities between the electromagnetic and weak interactions could be explained as a "spontaneous breakdown" of gauge symmetry.

The Standard Model specifies four gauge bosons, the 3 massive vector bosons of the weak interaction and the photon of the electromagnetic interaction as the carrier of the electroweak force. One of the predictions of the Standard Model is the existance of a weak neutral current interaction mediated by the exchange of a single Z^0 boson. The prediction was verified in 1973 at CERN with the observation of weak neutral current interactions in the Gargamelle bubble chamber [7]. This provided strong experimental evidence as to the validity of the Standard Model. Recently also at CERN [8–9], the three massive intermediate vector bosons were

directly observed in collider experiments further verifying the Standard Model and making it one of the great triumphs of modern physics.

From this, many grand unified theories which unify the strong and the electroweak interactions have arisen. Georgi and Glashow [10] in 1974 developed such a theory based on an $SU(5)$ group which can be spontaneously broken into $SU(3) \times SU(2) \times U(1)$. This theory which was successful in explaining many of the interactions of hadrons and leptons, gave a specific prediction for the electroweak mixing parameter, $\sin^2 \theta_W$. Many other of these theories also give specific values for $\sin^2 \theta_W$. Often the predictions for $\sin^2 \theta_W$ were slightly different. An accurate determination of this parameter from experiment would help to constrain as well as guide many of the attempts at grand unification.

The reaction, $\nu_\mu e \rightarrow \nu_\mu e$ provides one of the best ways to test the Standard Model and to provide a determination of the electroweak mixing parameter, $\sin^2 \theta_W$. This reaction provides several advantages, 1) it is a purely weak interaction uncomplicated by elctromagnetic or strong interactions, 2) it is mediated by a single Z^0 for which the Standard Model gives definite predictions in terms of the electroweak mixing parameter, and 3) the process is an elastic two body interaction which simplifies the necessary kinematic determinations. In addition the Standard Model may also be scrutinized by this reaction for possible modifications, such as electromagnetic properties for the neutrino.

1. Kinematics and Signature

The kinematics for $\nu_\mu e \rightarrow \nu_\mu e$ scattering is straight forward as for any elastic two body scattering (see Fig. 1.1.1). The conservation of energy and momentum can be expressed as

$$k_1 + p_1 = k_2 + p_2$$

where the k_1 and k_2 are the initial and final 4-vectors respectively for the neutrino and p_1 and p_2 are the initial and final 4-vectors respectively for the electron. Rearranging the terms

$$k_1 - p_2 = k_2 - p_1$$

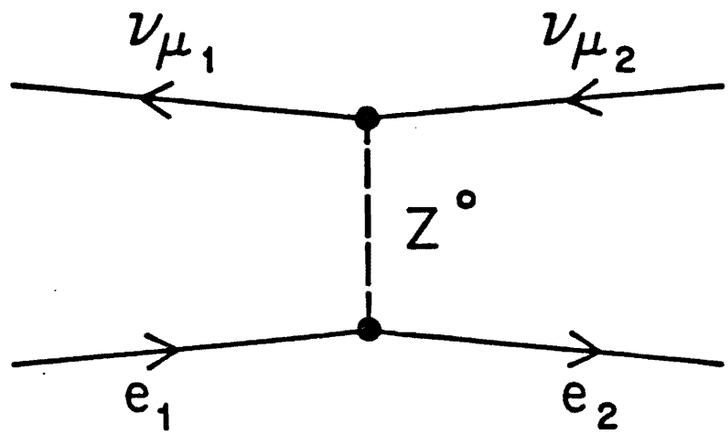

(a)

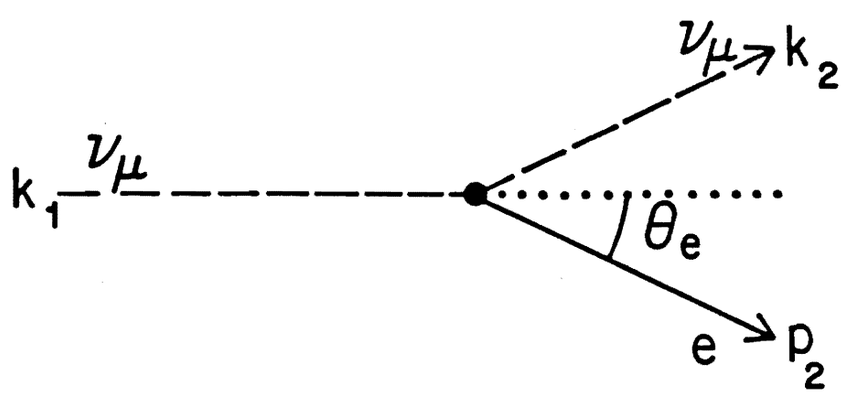

(b)

Figure 1.1.1 a) Feynman diagram for $\nu_\mu e \rightarrow \nu_\mu e$ elastic scattering, b) Kinematics for $\nu_\mu e \rightarrow \nu_\mu e$ elastic scattering

and squaring both sides results in

$$k_1^2 - 2k_1 \cdot p_2 + p_2^2 = k_2^2 - 2k_2 \cdot p_1 + p_2^2.$$

The squares of the 4-vectors are the squares of the particle masses

$$k_1^2 = k_2^2 = 0 \quad \text{and} \quad p_1^2 = p_2^2 = m_e^2$$

which cancel so that

$$k_1 \cdot p_2 = k_2 \cdot p_1.$$

Using lab coordinates, the equation becomes

$$E_\nu E_e - E_\nu P_e \cos\theta = E'_\nu m_e$$

where E_ν is the incident neutrino energy, E_e is the recoil electron energy, θ is the recoil electron angle with respect to the incident beam direction and by conservation of energy, the recoil neutrino energy is

$$E'_\nu = E_\nu + m_e - E_e.$$

The equation then becomes

$$E_\nu(E_e - P_e \cos\theta) = m_e(E_\nu + m_e - E_e).$$

The fraction of energy transfered to the electron, y, is defined as

$$y \equiv (E_e - m_e)/E_\nu.$$

By subsitution and cancelation of the common factor of E_ν, the previous equation reduces to

$$E_e - P_e \cos\theta = m_e(1 - y).$$

For accelerator energies, $E_e >> m_e$ and $E_e \approx P_e$, the equation becomes

$$E_e(1 - \cos\theta) \approx m_e(1 - y).$$

The kinematics dictates that the electron angle, θ, must be small and the approximations, $\theta \approx 0$ and $\cos\theta \approx 1 - \frac{1}{2}\theta^2$ can be made such that

$$E_e\theta^2 \approx 2m_e(1-y)$$

from which follows

$$\theta^2 < \frac{2m_e}{E_e}.$$

This result provides the most striking signature for $\nu_\mu e \rightarrow \nu_\mu e$ scattering. The most obvious way to indentify $\nu_\mu e \rightarrow \nu_\mu e$ events is to look for this signal as a peak at small angles in θ^2. This result together with minimum electron energies in this experiment of approximately 0.2 GeV indicates that $\nu_\mu e \rightarrow \nu_\mu e$ events would be expected to populate the region below $0.005 rad^2$ in θ^2. For this experiment to be successful, the detector must capable of fine angular resolution in the forward beam direction.

2. The Cross Section

For weak interactions [11–12]

$$L = -\frac{G_F}{\sqrt{2}} J_\mu(x) J^{\mu\dagger}(x) + h.c.$$

where

$$J_\mu(x) = \rho J_\mu^{NC}(x) + J_\mu^{CC}(x)$$

is the sum of the neutral current and charged current components. The factor ρ allows for the possibility that the neutral current and charged current interactions have different coupling strengths. For $\nu_\mu e \rightarrow \nu_\mu e$ interactions, the Lagrangian becomes [13]

$$L = \rho^2 \frac{G_F}{\sqrt{2}} \bar{\nu}\gamma_\mu(1+\gamma_5)\nu\bar{e}\gamma_\mu(g_V + g_A\gamma_5)e$$

where g_V and g_A are the vector and axial-vector coupling constants for the electron. The differential cross section for $\nu_\mu e \rightarrow \nu_\mu e$ interactions then takes the form

$$\frac{d\sigma(\nu_\mu e)}{dy} = \rho^2 \frac{G_F^2 m_e E_\nu}{2\pi}[(g_V + g_A)^2 + (g_V - g_A)^2(1-y)^2 + \frac{m_e y}{E_\nu}(g_V^2 + g_A^2)]$$

where E_ν is the incident neutrino energy in the lab frame and y is the fraction of neutrino energy tranfered to the electron. The differential cross section for $\bar{\nu}_\mu e \rightarrow \bar{\nu}_\mu e$ interactions can be found by simply replacing g_A with $-g_A$ such that

$$\frac{d\sigma(\bar{\nu}_\mu e)}{dy} = \rho^2 \frac{G_F^2 m_e E_\nu}{2\pi}[(g_V - g_A)^2 + (g_V + g_A)^2(1-y)^2 + \frac{m_e y}{E_\nu}(g_V^2 + g_A^2)]$$

For accelerator neutrinos, $E_\nu >> m_e$, the last term in each differential cross section is negligible. By integrating over all possible value for y from 0 to 1, the total cross section for each case becomes

$$\sigma(\nu_\mu e) = \rho^2 \frac{G_F^2 m_e E_\nu}{2\pi}[(g_V + g_A)^2 + \frac{1}{3}(g_V - g_A)^2]$$

and

$$\sigma(\bar{\nu}_\mu e) = \rho^2 \frac{G_F^2 m_e E_\nu}{2\pi}[(g_V - g_A)^2 + \frac{1}{3}(g_V + g_A)^2].$$

where from the predictions of the Standard Model

$$g_V = -\frac{1}{2} + 2\sin^2\theta_W, \quad g_A = -\frac{1}{2}$$

and

$$\rho^2 = 1.$$

By forming the ratio of cross sections, $R = \sigma(\nu_\mu e)/\sigma(\bar{\nu}_\mu e)$ an expression can be formed independent of the ρ^2 parameter. In terms of g_V and g_A, the ratio of cross sections becomes

$$R = \frac{(g_V + g_A)^2 + \frac{1}{3}(g_V - g_A)^2}{(g_V - g_A)^2 + \frac{1}{3}(g_V + g_A)^2}.$$

In terms of $\sin^2\theta_W$, the ratio can be expressed as

$$R = 3\frac{1 + 4\sin^2\theta_W + \frac{16}{3}\sin^4\theta_W}{1 + 4\sin^2\theta_W + 16\sin^4\theta_W}.$$

A plot of the cross sections and Ratio as a function of $\sin^2\theta_W$ is shown in Fig. 1.2.1.

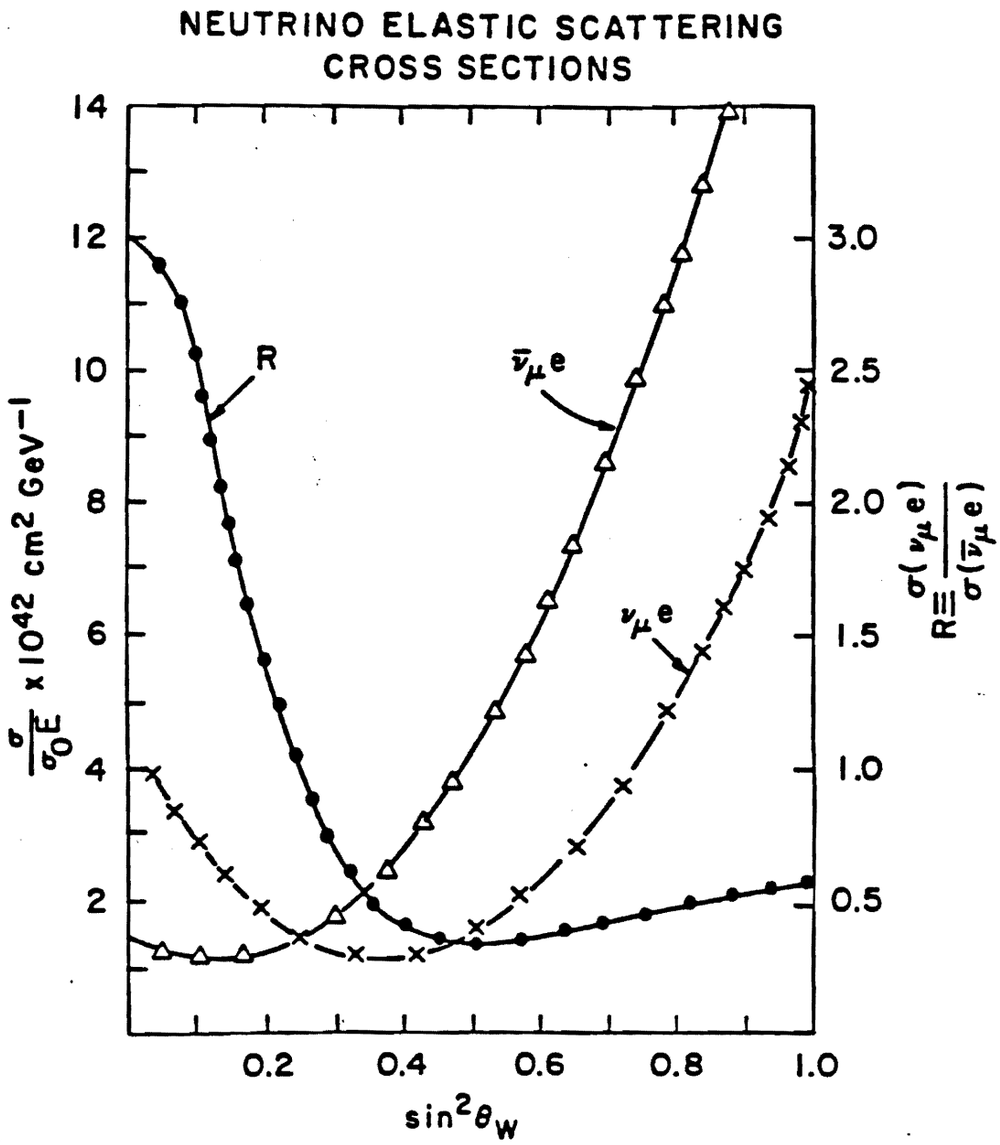

Figure 1.2.1 Cross sections and Ratio versus $\sin^2\theta_W$

3. Electromagnetic Contributions

An inevitable result of most gauge theories of leptons is the existence of possible electromagnetic properties for the neutrino. These electromagnetic properties may be manifest in the form of a charge radius or magnetic momment for the neutrino. Other electromagnetic properties may include a neutrino lifetime whereby the neutrino decays to a "lower" state by the emission of a photon. It may be possible to experimentally scrutinize neutrino interactions for the possible electromagnetic effects. Neutrino electron scattering provides one of the best techniques for this.

The matrix element of an electromagnetic current between neutrino states may be expressed as

$$< \nu(k')|J_\mu|\nu(k) >= -ie\bar{\nu}(k')[\gamma_\mu F_1(q^2) + \sigma_{\mu\nu}q_\nu F_2(q^2)]\nu(k)$$

where $F_1(0) = 0$, $F_1(q^2) \approx \frac{1}{6} < r^2 > q^2$ and $F_2(q^2) \approx f/2m_e$ with $< r^2 >$, the charge radius and f, the magnetic moment [14–15].

For $\nu_\mu e \rightarrow \nu_\mu e$ scattering, a charge radius leads to a modification in the total cross section of

$$\sigma_{\nu_\mu e} = \sigma^{SM}_{\nu_\mu e}(\sin^2\theta_W) + \frac{2m_e E_\nu}{3\pi}[\frac{\pi}{\sqrt{2}}\alpha G_F < r^2 > (\frac{8}{3}\sin^2\theta_W - 1) + \frac{2\pi^2}{9}\alpha^2 < r^2 >^2]$$

where $\sigma^{SM}_{\nu_\mu e}(\sin^2\theta_W)$ is the cross section prediction of the Standard Model. By straightforward manipulation, the modified cross section can be re-expressed as

$$\sigma_{\nu_\mu e} = \sigma^{SM}_{\nu_\mu e}(\sin^2\theta_W + \delta)$$

where

$$\delta \equiv \frac{\pi\alpha}{3\sqrt{2}G_F} < r^2 >$$

can then be observed as a deviation from the value for $\sin^2\theta_W$ determined from non-neutrino experiments.

The existence of a possible neutrino magnetic moment requires neutrinos of both helicities. The interaction of a neutrino possessing non-zero magnetic moment, f with an electromagnetic field, $F^{\alpha\beta}$, is given by [16]

$$L = \frac{1}{2} f(\frac{e}{2m_e})\bar{\nu}\sigma_{\alpha\beta}\nu F^{\alpha\beta}$$

where the neutrino must undergo a change in helicity. For $\nu_\mu e \rightarrow \nu_\mu e$ scattering, a magnetic moment leads to a contribution to the differential cross section of

$$d\sigma_f/dy = \frac{\pi\alpha^2}{m_e^2} f^2(\frac{1}{y} - 1).$$

By intergrating over y from y_{min} to 1 where $y_{min} = E_e^{min}/E_\nu$, the total cross section becomes

$$\sigma_{\nu_\mu e} = \sigma_{\nu_\mu e}^{SM}(\sin^2\theta_W) + \frac{\pi\alpha^2}{m_e^2} f^2[\ln(E_\nu/E_e^{min}) - 1 + E_e^{min}/E_\nu]$$

where $\sigma_{\nu_\mu e}^{SM}(\sin^2\theta_W)$ is the form of the cross section predicted by the Standard Model and E_e^{min} is the experimental low energy cut-off on the recoiled electron energy.

4. Experimental Goals

The goal of this thesis is to determine experimentally the cross section for $\nu_\mu e \rightarrow \nu_\mu e$ scattering from a sample of over 100 expected $\nu_\mu e \rightarrow \nu_\mu e$ events collected by the E734 neutrino detector in BNL wide band neutrino beam. By combining these results with with results from an anti-neutrino determination of the cross section for $\bar{\nu}_\mu e \rightarrow \bar{\nu}_\mu e$ scattering in the form of a ratio of cross sections, the weak coupling constants for the electron, g_V and g_A can be determined in a model independent way to within a four fold ambiguity where three of the ambiguities can be eliminated by results from e^+e^- experiments. The predictions of the Standard Model for the weak coupling constants can then be tested and a precise determination of the electroweak mixing parameter, $\sin^2\theta_W$ can be made.

By investigating the y dependent effects on the angular distribution of the event sample combined with the absolute cross section determination for $\nu_\mu e \rightarrow$

$\nu_\mu e$ scattering, a single-experiment determination of the weak coupling constants can be done. These results are shown to be consistent with the previous determination of g_V and g_A as well as with the Standard-Model predictions.

The experimental error on the determination of the $\nu_\mu e \rightarrow \nu_\mu e$ scattering cross section is then investigated as an upper limit on the existence of possible electromagnetic effects of the neutrino. A determination on the upper limits on the magnetic moment and charge radius of the muon neutrino is then made.

Chapter 2.

Experimental Apparatus

1. Neutrino Beam

For neutrino/anti-neutrino production, approximately 10^{13} protons per pulse are accelerated to an energy of 28.3 GeV in repetitive cycles (every 1.4 seconds) by the Alternating Gradient Synchrotron (AGS) at BNL (see Fig. 2.1.1). The accelerated protons are grouped into 12 packets owing to the R.F. structure of the AGS. Each packet is 30 ns wide (FWHM) and is separated in time from the next packet by 224 ns as shown in Fig. 2.1.2. The accelerated protons are then extracted in a single revolution [17] of the A.G.S. (preserving the R.F. structure of the beam) and transported to the target (with a beam spot size of approximately 2 mm full width at the target).

The target consists of three sapphire rods (Al_2O_3) 6.4 mm in diameter and totaling 45 cm in length (approximately two interaction lengths for protons at this energy). The target is enclosed in a water cooled stainless cylinder embedded in the front of two concentric electromagnetic focusing horns (see Fig. 2.1.3). In the region between the two horns, a magnetic field is produced for a period of 32 μs during each beam extraction. The magnetic field is generated by the discharge of twenty 42 μF (12 kV) capacitors producing a current of 250 kA passing in series through the surface of each horn [18](see Fig. 2.1.4).

When the accelerated protons impact the target a wide energy distribution of secondary particles (predominantly pions and kaons) is produced. The horns' magnetic field strongly focuses the secondary particles of a particular charge (positive or negative); while particles of opposite charge are strongly defocused. This permits selection of a neutrino or anti-neutrino beam by choice of horn polarity.

The beam of focused particles emerging from the second horn is nearly parallel with a divergence of less than 33 mrad as it enters a 50 meter decay region. The layout of the AGS neutrino beam line is shown in Fig. 2.1.5. As the beam travels

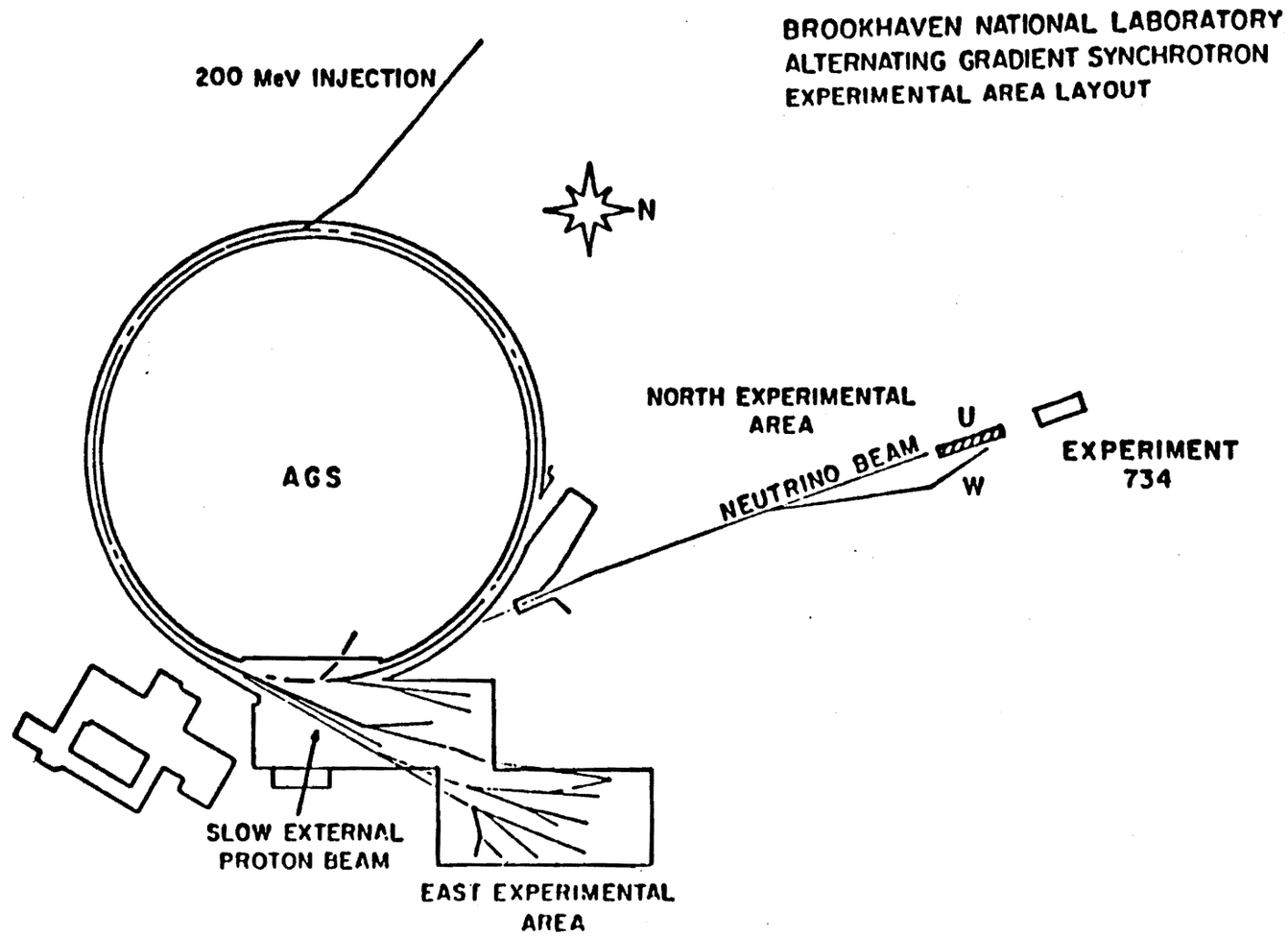

Figure 2.1.1 The AGS at Brookhaven National Laboratory

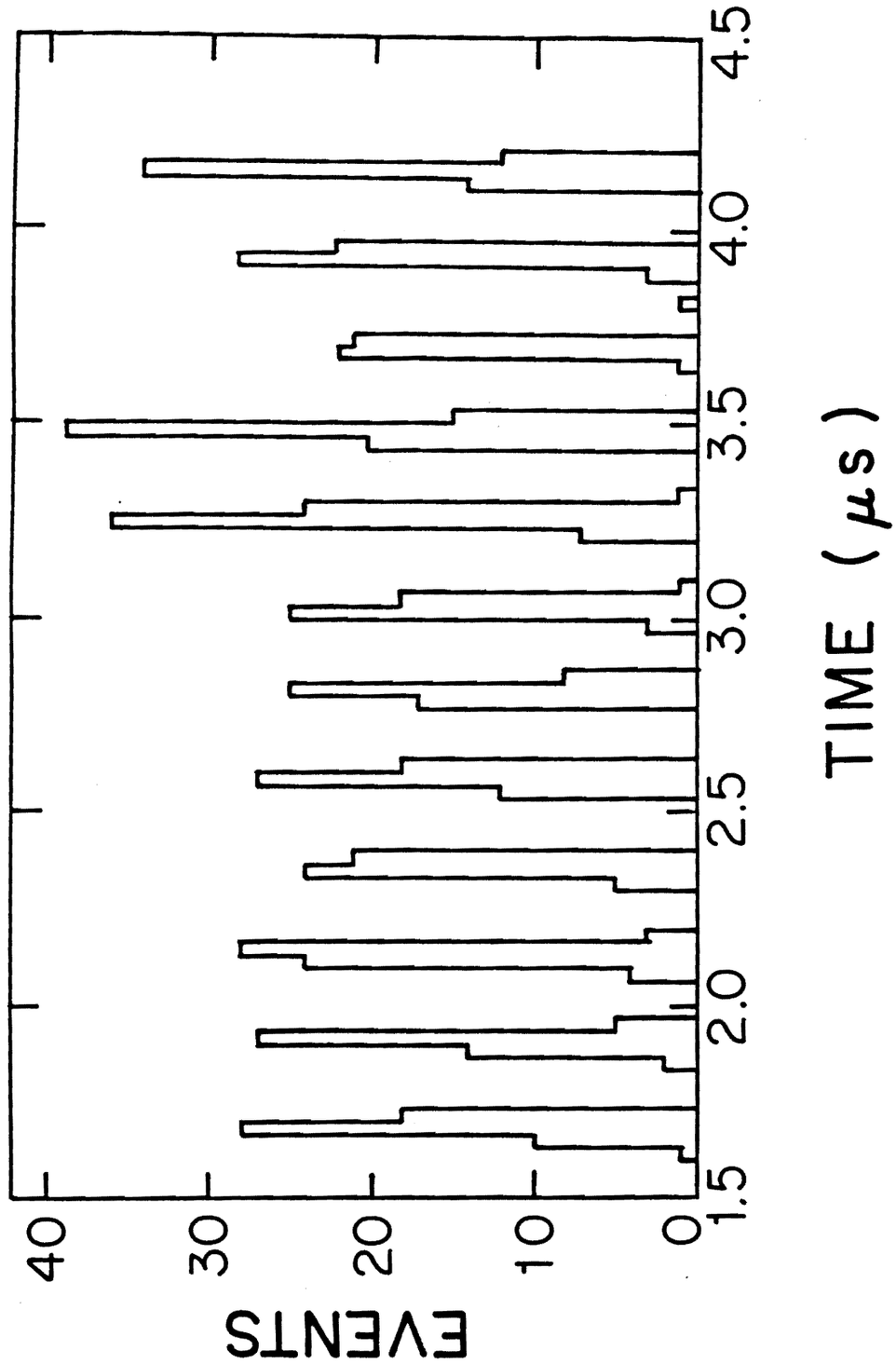

Figure 2.1.2 The distribution in time for neutrino interactions, reflecting the bunch structure of the AGS beam

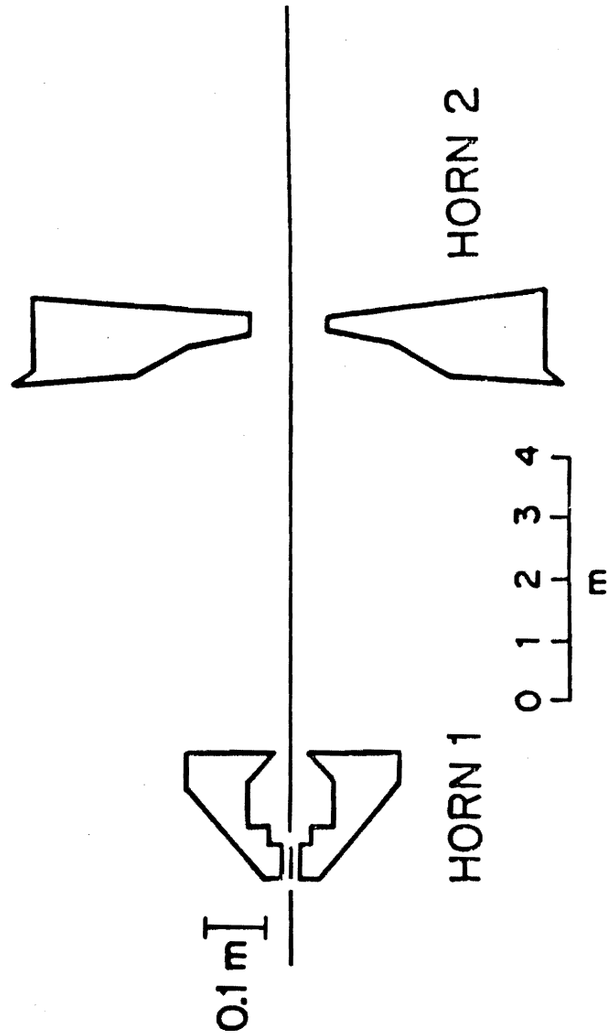

Figure 2.1.3 The layout of the magnetic horn system

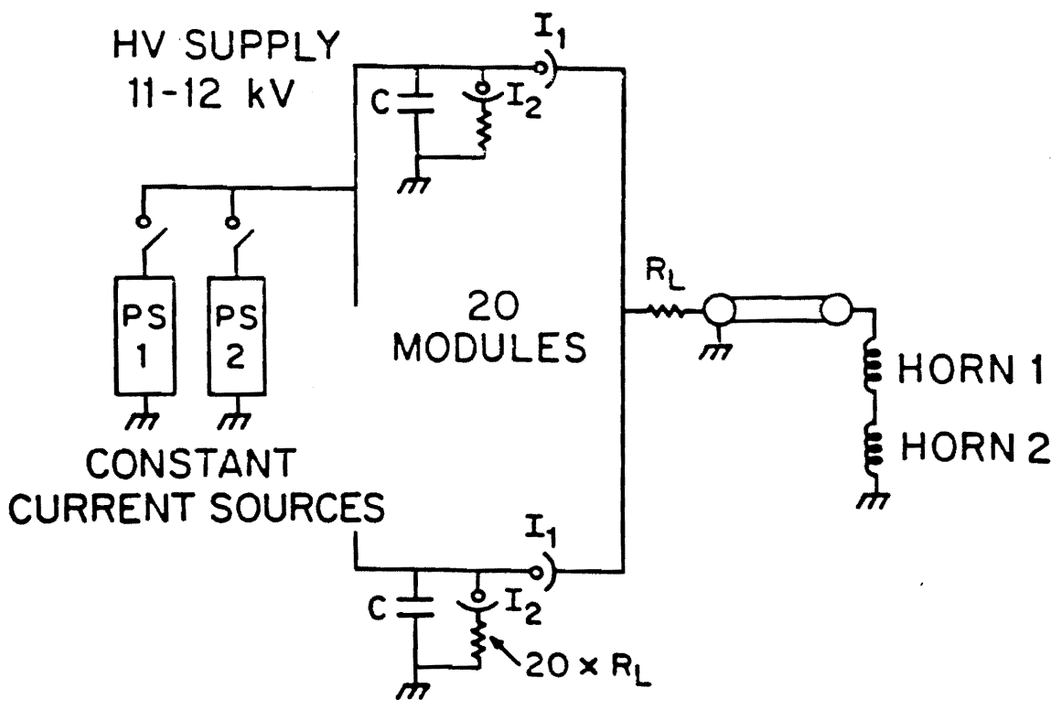

Figure 2.1.4 Schematic of the horn current system

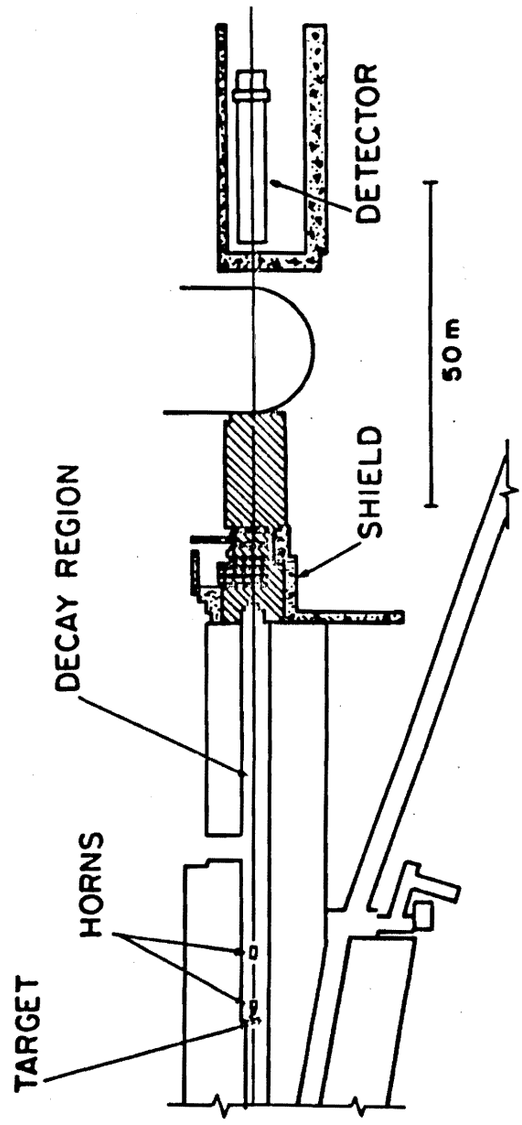

Figure 2.1.5 Layout of the neutrino beam line at the AGS

down the length of the decay region, the short lived constituents of the beam subsequently decay, predominantly into muons and muon neutrinos (or anti-neutrinos depending on the charge of the focused particles).

Located downstream of the decay region is 32 meters of steel and earth designed to remove any hadrons and the major fraction of muons that emerge from the decay region. (On average, approximately one muon per beam spill escapes through the shield and enters the fiducial volume of the detector.) Inside the steel shielding, ion chambers are positioned to measure the muon flux in the shield. These chambers are used primarily for monitoring the beam intensity, alignment and timing.

Charged pions and kaons created in the horn produce neutrinos or anti-neutrinos by their decay. The target production rate for positive pions and kaons is approximately twice the production rate for negative ones. This results in a total integrated neutrino flux approximately twice the total anti-neutrino flux. The proportion of charged pions produced is a factor of 20 greater than for charged kaons. This means that neutrinos from charged kaon decay contribute significantly only at the high momentum end of the spectrum. The predominant decay mode is $\pi^+ \rightarrow \mu^+ + \nu_\mu$ ($\pi^- \rightarrow \mu^- + \bar{\nu}_\mu$) for charged pions and $K^+ \rightarrow \mu^+ + \nu_\mu$ ($K^- \rightarrow \mu^- + \bar{\nu}_\mu$) for charged kaons. Contributions to the neutrino/anti-neutrino spectrum from the decay of other hadrons are small and may be neglected.

The neutrino spectra were measured indirectly from the observations of quasi-elastic neutrino reactions, $\nu_\mu n \rightarrow \mu^- p$ ($\bar{\nu}_\mu p \rightarrow \mu^+ n$) in the detector and the muon spectrometer. Two techniques were used to determine the spectra. One technique involved the study of quasi-elastic events where the muon stopped inside the fiducial volume of the detector. The other involved the study of quasi-elastic events where the muon traversed the muon spectrometer. Both techniques used the determination of the muon energy and direction to reconstruct the incident neutrino energy. Since the quasi-elastic reaction is a simple two body problem,

the neutrino energy can be found from energy-momentum conservation,

$$E_\nu = \frac{m_N E_\mu - \frac{1}{2}m_\mu^2}{m_n - E_\mu + P_\mu \cos\theta_\mu}$$

where

$$P_\mu = \sqrt{E_\mu^2 - m_\mu^2}$$

and m_N is the nucleon mass (0.939 GeV), m_μ is the muon mass (0.106 GeV), E_μ is the total muon energy and θ_μ is the muon recoil angle with respect to the incident beam direction.

For the quasi-elastic events where the muon stopped within the body of the detector, the muon's range and direction can be measured and its energy calculated. To reduce contamination from other neutrino reactions, the reaction topology is required to be observed as a single track, and the muon is required to traverse more than 15 modules and be within 20° with respect to the beam direction. This selection limits the acceptance to neutrinos above 0.3 GeV, but since both flux and cross section are small below this energy, the limit is not important. The upper energy limit of this technique is given by the overall length of the detector and is about 1.5 GeV. There were 2284 and 2665 selected events in the neutrino and anti- neutrino data sets, respectively. Background contributions from other neutrino reactions were $(39 \pm 8)\%$ and $(31 \pm 6)\%$, respectively.

For quasi-elastic events where the muon leaves the detector and traverses the muon spectrometer, the muon energy and direction can be determined. The muon energy is determined from the momentum measured in the magnet of the spectrometer plus the energy loss in the detector [19]. Additionally, the charge of the muon can also be determined. This will provide the ability to determine the extent of contamination in the beam from wrong sign (helicity) neutrinos.

From the previous techniques, the incident neutrino spectrum can be determined by

$$\phi(E_\nu) = \frac{N_{QE}(E_\nu)}{A_{QE}(E_\nu) \times \sigma_{QE}(E_\nu) \times n_N}$$

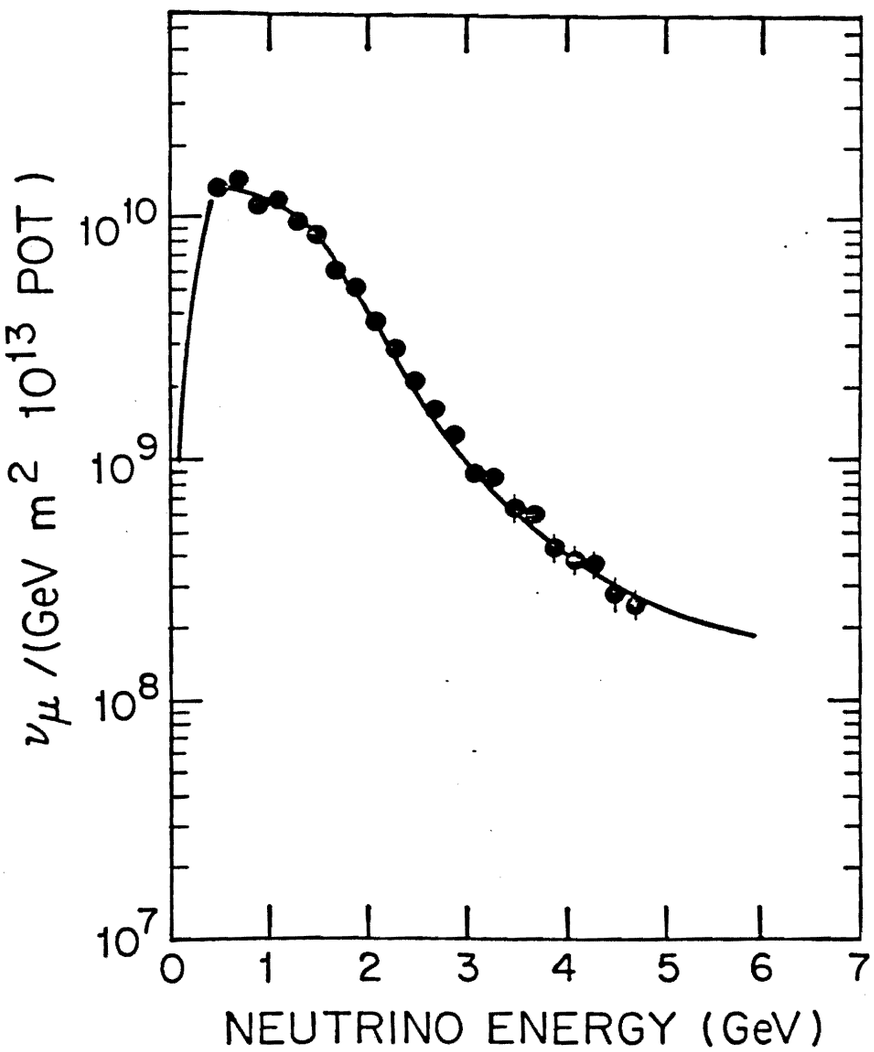

Figure 2.1.6 The measured ν_μ spectrum determined from quasi-elastic events

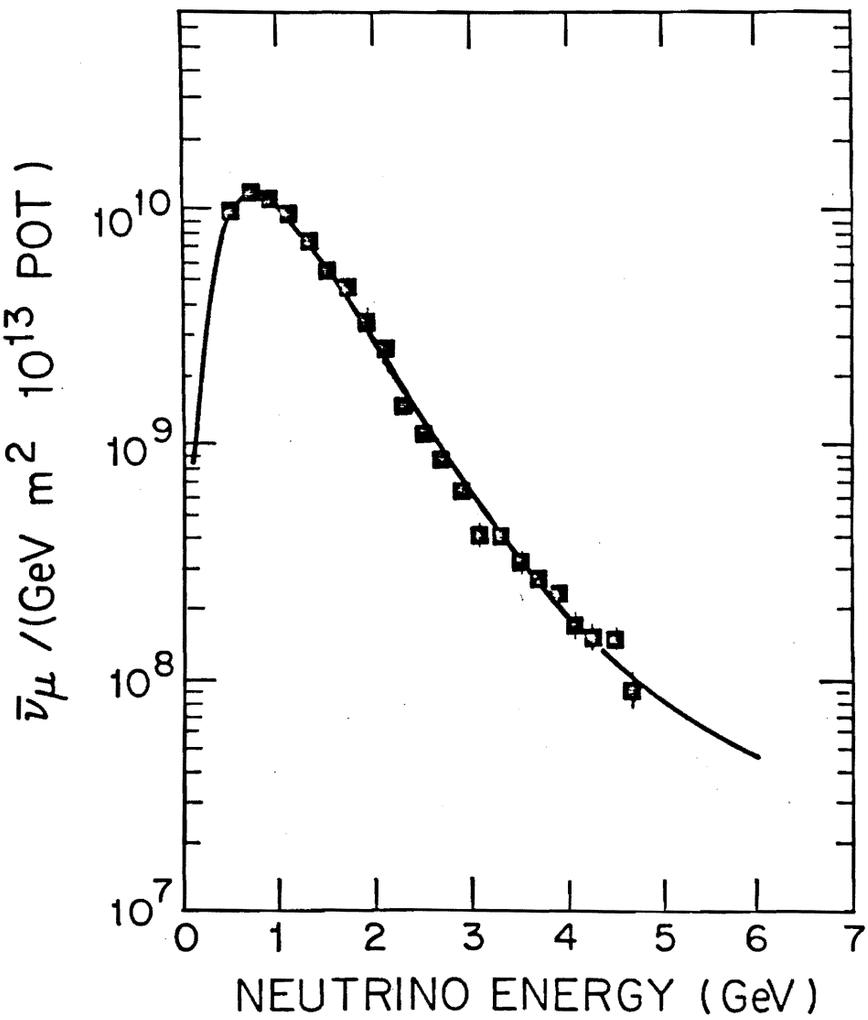

Figure 2.1.7 The measured $\bar{\nu}_\mu$ spectrum determined from quasi-elastic events

where $N_{QE}(E_\nu)$ are the number of selected events within the energy bin at incident neutrino energy, E_ν, $A_{QE}(E_\nu)$ is the quasi-elastic acceptance as a function of E_ν determined from MONTE CARLO studies, $\sigma_{QE}(E_\nu)$ is the quasi-elastic cross section and n_N is the number of target nucleons in the fiducial volume of the detector. The resulting ν_μ spectrum is shown in Fig. 2.1.6 and the resulting $\bar{\nu}_\mu$ spectrum is shown inFig. 2.1.7 along with the NUBEAM calculation of the spectra (solid line).

Two classes of contamination are present in the final neutrino/anti-neutrino beam, wrong helicity neutrinos and electron neutrinos. Wrong helicity neutrinos are produced from the decay of pions and/or kaons of opposite charge which were not completely defocused from the forward direction by the horns. The measurement of wrong helicity contamination is performed using the muon spectrometer (discussed later) positioned at the downstream end of the detector. Since the production rate for positive pions (neutrinos) is approximately twice the rate for negative pions (anti-neutrinos), the wrong helicity contamination in the anti-neutrino beam is expected to be approximately four times the contamination in the neutrino beam [19]. The wrong helicity spectra measured by quasi-elastic events in the spectrometer are shown in Fig. 2.1.8 along with the NUBEAM calculation (solid curve). NUBEAM [19] is a neutrino beam Monte Carlo used to calculate neutrino spectra for given experimental apparatus. NUBEAM was adapted for this experiment and used to calculate the expected neutrino spectra and contaminations.

Muons produced in pion decay have a probability of decaying before being absorbed in the shielding. Their decay produces electron neutrinos via the decay mode, $\mu^+ \rightarrow e^+ + \nu_e + \bar{\nu}_\mu$ ($\mu^- \rightarrow e^- + \bar{\nu}_e + \nu_\mu$). The contamination level in the neutrino beam for this process is approximately $2.0 \times 10^{-3} \nu_e/\nu_\mu$. Some charged kaon decay modes can also produce electron neutrinos. The decay $K^+ \rightarrow \pi^0 + e^+ + \nu_e$ ($K^- \rightarrow \pi^0 + e^- + \bar{\nu}_e$) produces a contamination level of approximately $2.5 \times 10^{-3} \nu_e/\nu_\mu$. The other source of electron neutrinos comes from the decay $K_L \rightarrow \pi^+ + e^- + \bar{\nu}_e$ ($K_L \rightarrow \pi^- + e^+ + \nu_e$). The production of K_L does not have

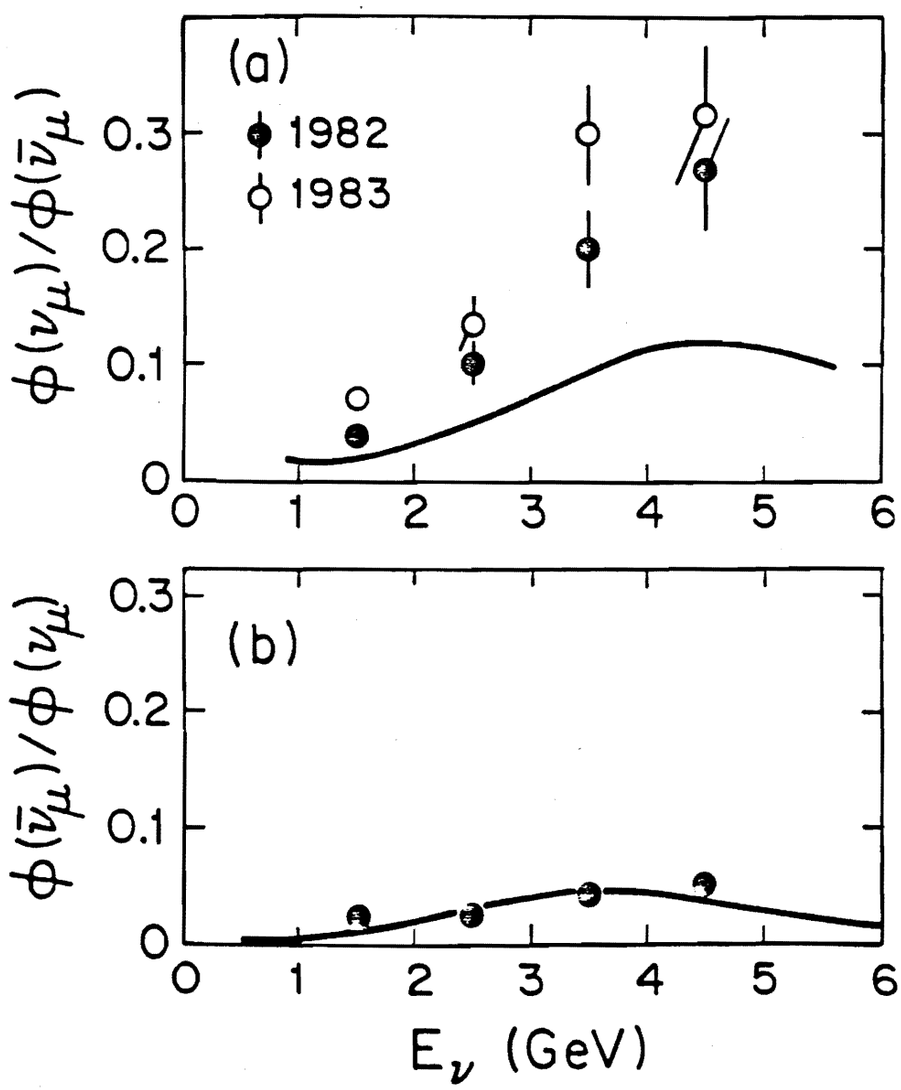

Figure 2.1.8 The measured spectra of the wrong helicity neutrinos from quasi-elastic spectrometer events

focused enhancement and is not directly measurable. The contamination from this source is not well known, but is estimated to be small.

Electron neutrino contamination is particularly critical in this experiment. Electron neutrino interactions with nucleons produce a single final state forward electron (positron) which can mask muon neutrino electron elastic interactions. The cross section for this process is four orders of magnitude greater than the neutrino electron cross section. This represents a difficult background challenge for signal extraction. However, the flux $\phi(E(\nu_e))$ can be determined from the reaction, $\nu_e n \rightarrow e^- p$ with techniques similar to those discussed above where the electron is identified by the electromagnetic shower it produces [19,20]. The ν_e spectrum is shown in Fig. 2.1.9 along with the NUBEAM calculation (solid curve).

2. Main Detector

Owing to the small cross sections characteristic of weak interactions, massive detectors are required to produce effective signal rates. The signal in this experiment dictates that the detector not only be massive but must be mostly active, highly segmented and possess fine energy and angular resolution. These requirements are paramount in the ability to resolve signal from background. The detector used in this experiment satisfies these criteria [21].

The detector weighs 172 metric tons and is segmented into 112 identical modules. The detector is shown in Fig. 2.2.1. Each module consists of one plane of liquid scintillator calorimeter cells and two planes (mounted horizontally and vertically) of proportional drift tubes (PDT). The liquid scintillator accounts for 80% of the detector mass. The remaining mass is distributed among the calorimeter acrylic and the structural aluminum for the PDTs. A list of sources for materials used in the contruction of the detector is contained in Ref. 21.

Downstream of the main detector is a 30 metric ton shower counter consisting 10 planes of calorimeter cells interspersed with ten radiation lengths of lead. This is used to contain showers produced in the rear of the main detector. Downstream of the shower counter is a magnetic spectrometer. The spectrometer utilizes an

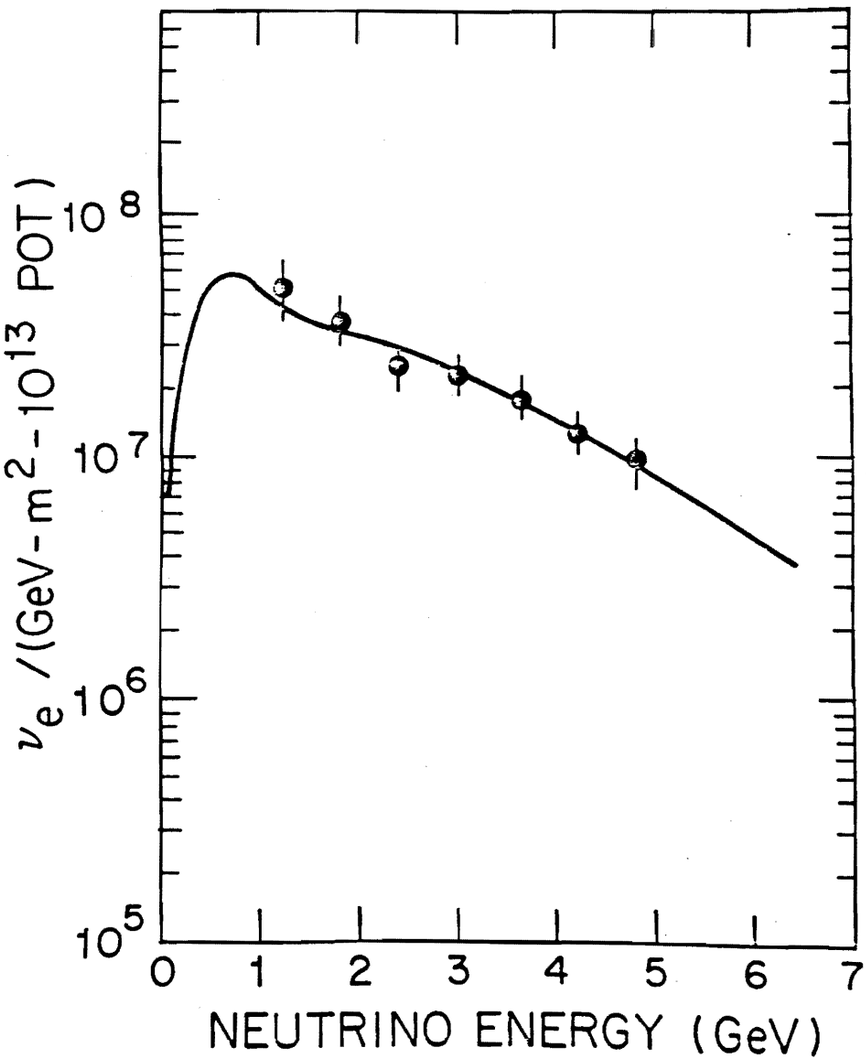

Figure 2.1.9 The measured ν_e spectrum

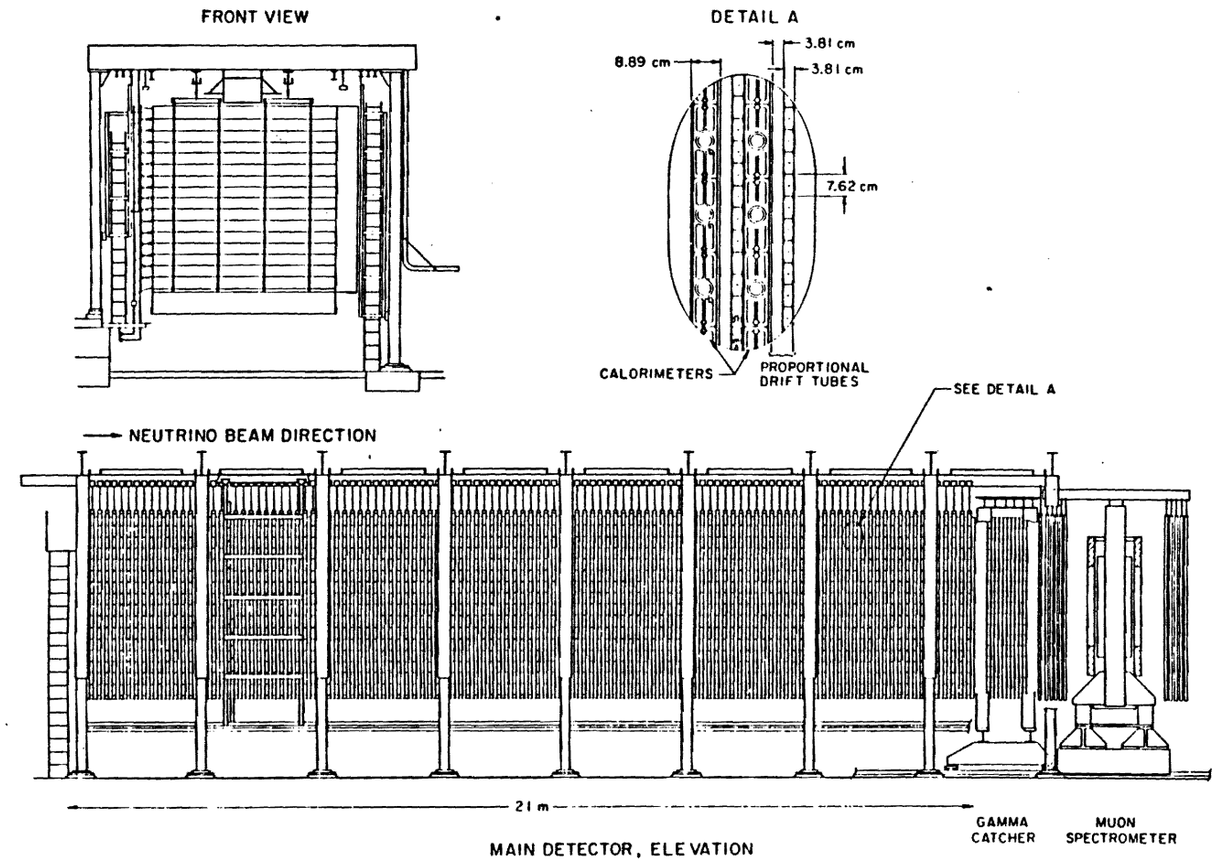

Figure 2.2.1 The E734 neutrino detector

open air gap magnet with a $1.8m \times 1.8m \times 0.46m$ aperture. On either end of the magnet are nine PDT planes as tracking chambers. The magnetic spectrometer is used to measure the spectrum of neutrinos and anti-neutrinos indirectly from quasi-elastic scattering reactions.

3. Calorimeter System

Each calorimeter plane consists of 16 cells mounted horizontally to form an array with a $4m \times 4m$ active area. Each cell consists of a rectangular extruded acrylic tube (with dimensions $4.00m \times 0.254m \times 7.62cm$ and wall thickness 2.5mm) fitted with a molded end cap at each end. Each end cap is fitted with a window for a 2 inch photomultiplier tube and a fiber optic cable (for calibration and diagnostics). The requirement for sufficient light collection from a minimum ionizing particle at the distant end of a cell limited the height of each cell to 0.254m. The cell is filled with a mixture of mineral oil (40%) and NE235A liquid scintillator (60%). Liquid scintillator was chosen for the active medium owing to its light output and attenuation properties and its relative cost. Each end cap was silvered to decrease reflective losses at the ends of each cell. The acrylic provides total internal reflection at the outside surface of the cell to enhance the light collection efficiency. Each cell was wrapped in light tight paper and assembled into planes of 16 cells each.

The photomultiplier tubes (PMT) were 2 inch diameter Amperex 2212A fitted with a printed circuit resistor chain. Each PMT gain was calibrated with a NaI scintillator and a standard source (^{241}Am). The gains were equalized to within 5% by the choice of resistor between the DC power supply and the divider chain. This enabled all PMTs to be operated at the same 2150 Volts. Twenty four power supplies were used to power the 3904 PMTs. The ground return on each resistor chain was isolated from the signal ground through a 10k resistor.

The fiber optic cable from each end cap was connected to an air spark gap. This served to introduce calibrated light pulses into to each end of the calorimeters to monitor and calibrate the performance of the calorimeter system and electronics.

The PMT signals were transmitted through RG62/U coax cable to the detector electronics.

The calorimeter electronics integrated the collected charge from each PMT and pulse time relative to the master gate. The PMT electronics are shown schematically in Fig. 2.3.1. A fast preamplifier generates a signal that is discriminated to form a trigger pulse. The discriminator level is set to a common level for all PMT by the setting of a D/A converter. The set level corresponds to the receipt of two or three photoelectrons which is roughly half the expected yield from a minimum ionizing particle passing through the midpoint of a calorimeter cell. The trigger pulse is passed to the timing circuitry for measurement. Aside from the primary trigger mode, the electronics provide a horizontal and a vertical cosmic ray trigger which are used for the maintenance and calibration of the detector.

The presence of a trigger pulse from either the left or right PMT enables the charge integration and data readout for both PMT. It also flags the cell as hit for the purpose of forming a cosmic ray trigger. If a trigger is detected, the charge signal from the slow preamplifier is integrated and held for readout. The integration is performed for 100 ns which exceeds the expected signal duration of approximately 50 ns.

To achieve nanosecond timing resolution, a hybrid digital-analog technique was used to measure the trigger times. A trigger pulse enables a 25 MHz digital counter produced from the 100 MHz master clock. This measures the coarse time to within 40 ns. To resolve the fine time to within 1 ns, the trigger pulse enables a current source to discharge a capacitor until it is disabled by the next clock cycle. The final voltage on the capacitor is then an interpolation of the time between the 40 ns clock cycles. Each PMT channel was equipped with two fine time circuits to measure the time of two independent hits.

4. PDT System

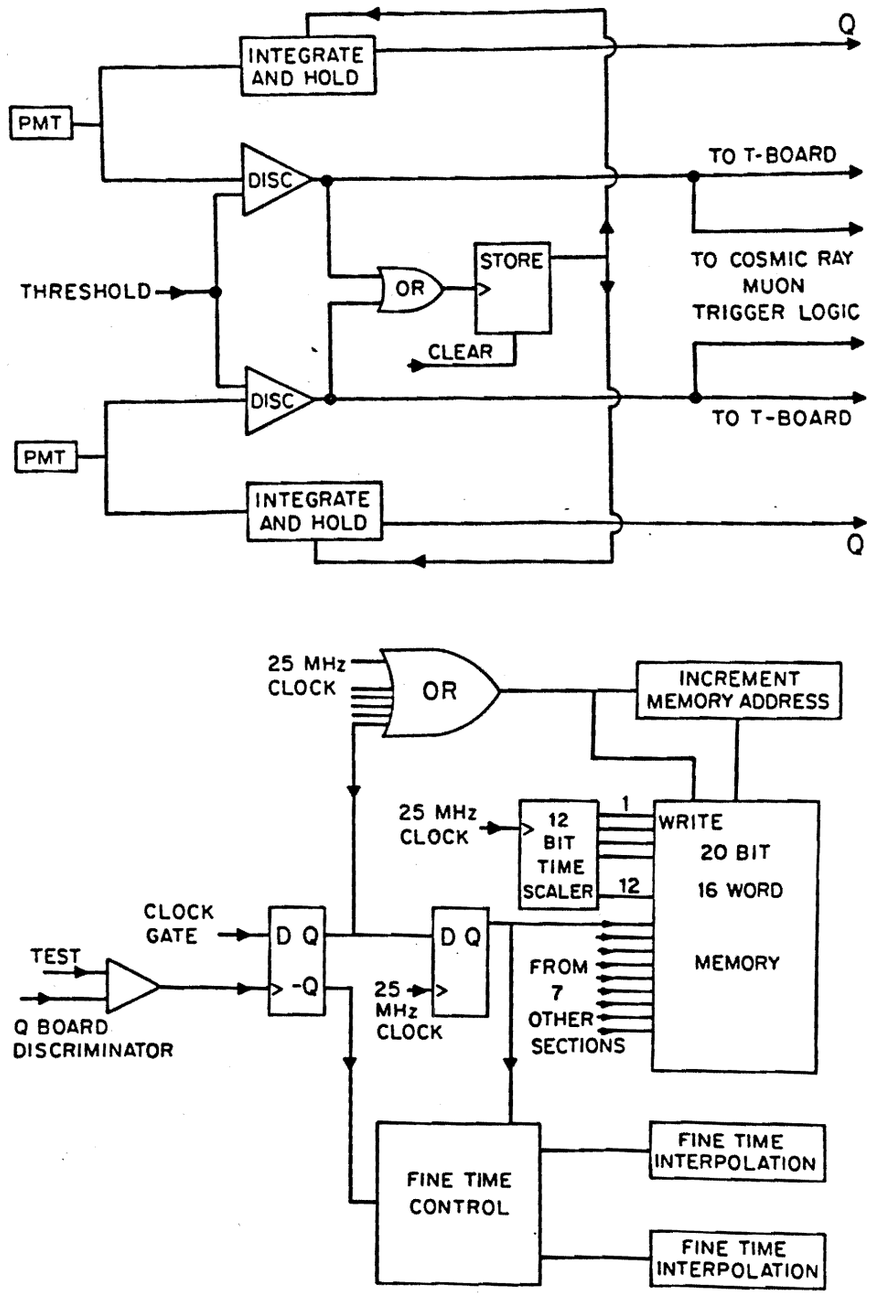

Figure 2.3.1 Diagram of the PMT electronics illustrating the charge integration and timing functions

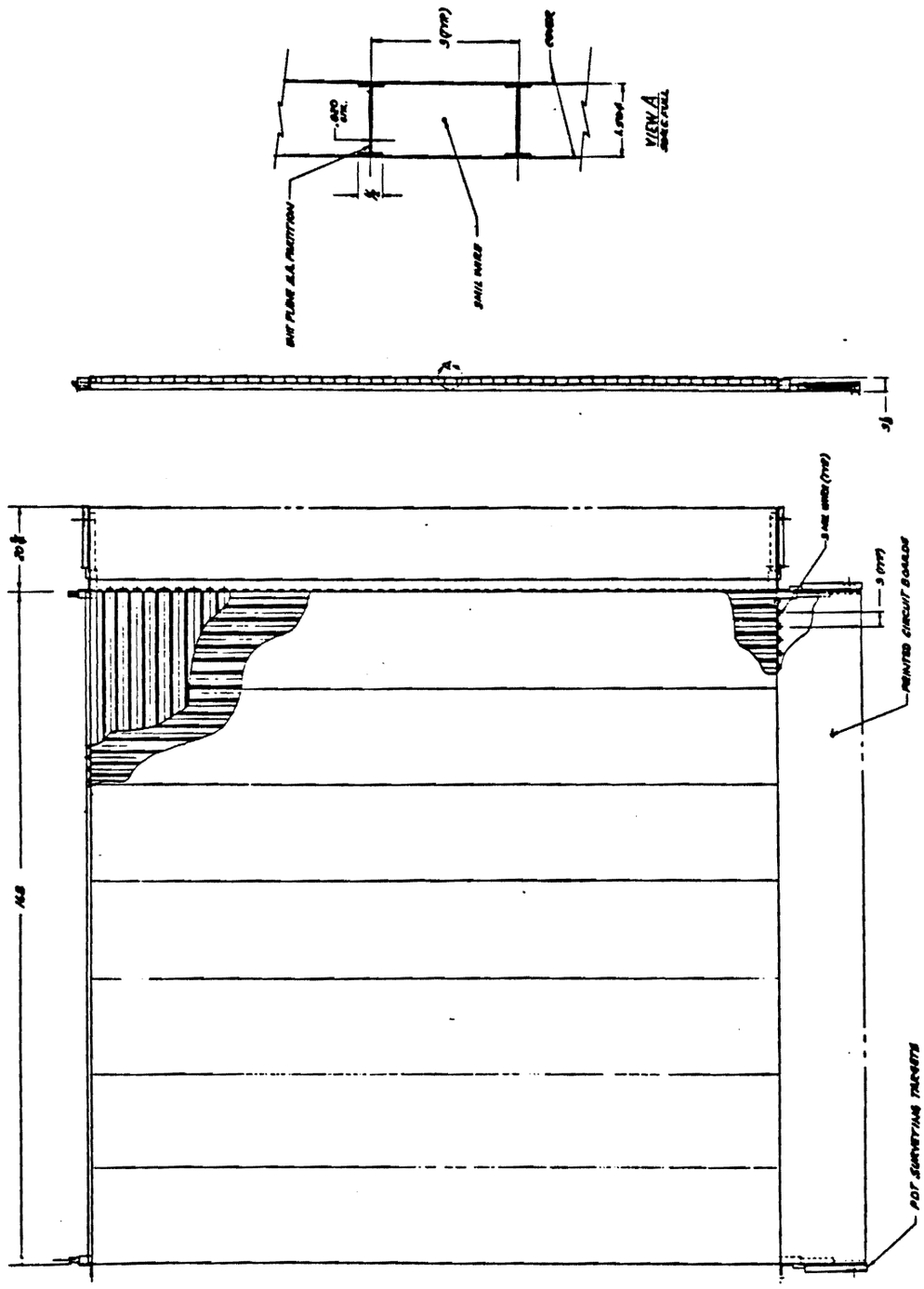

Figure 2.4.1 Construction of the PDT assembly

Each plane of proportional drift tubes (PDT) consists of 54 cells. Each plane was constructed from roll formed I-beams 4.2m in length spaced 76mm apart and sandwiched between 0.5mm aluminum sheets to form the 54 cells. Each cell was $3.8cm \times 7.6cm$ and closed with an injection molded end cap at each end. A 75 micron stainless steel wire threaded through the center of each end cap was pinned in place with a tension of 4.4 newtons. Pairs of PDT planes were oriented at right angles with respect to each other and glued together. The PDT construction is illustrated in Fig. 2.4.1.

Each x-y pair of PDT planes was suspended in place between each plane of calorimeters to form the main body of the detector. The PDTs were filled with P10 gas (10% methane, 90% argon) and checked for leaks. The P10 gas was circulated through the all the PDTs by a closed recirculating system which removed water vapor. The total volume of gas was recirculated every 48 hours with a replacement rate of 40 cubic meters per week. This rate was sufficient to keep oxygen contamination below an acceptable level of 400 ppm.

High voltage was applied to each PDT wire through a 20k resistor to produce an electric field within each cell. The PDTs were operated in the proportional region so that the number of ion pairs collected at the electrode was proportional to the energy deposited by passing charged particles [22]. The high voltage was regulated by a gain stabilization system to offset changes in atmospheric conditions which greatly affect the gain of the PDT. The gain stabilization system consisted of a ^{109}Cd X-ray source on a standard PDT cell monitored by a LSI 11/23 based system to control the PDT high voltage.

The electronics for the PDTs are designed to measure two pulse times and one integrated charge. The PDT electronics are shown schematically in Fig. 2.4.2. The pulse signal from each PDT is AC coupled to a preamplifier. The output from the preamplifier is differentiated and fed to a discriminator which determines if the PDT was hit. If the discriminator detects a signal above threshold, it triggers one of two 100 MHz clocks which count until the end of the master gate. A dead time of 800-1200 ns between discriminator firings is enforced so that long pulses

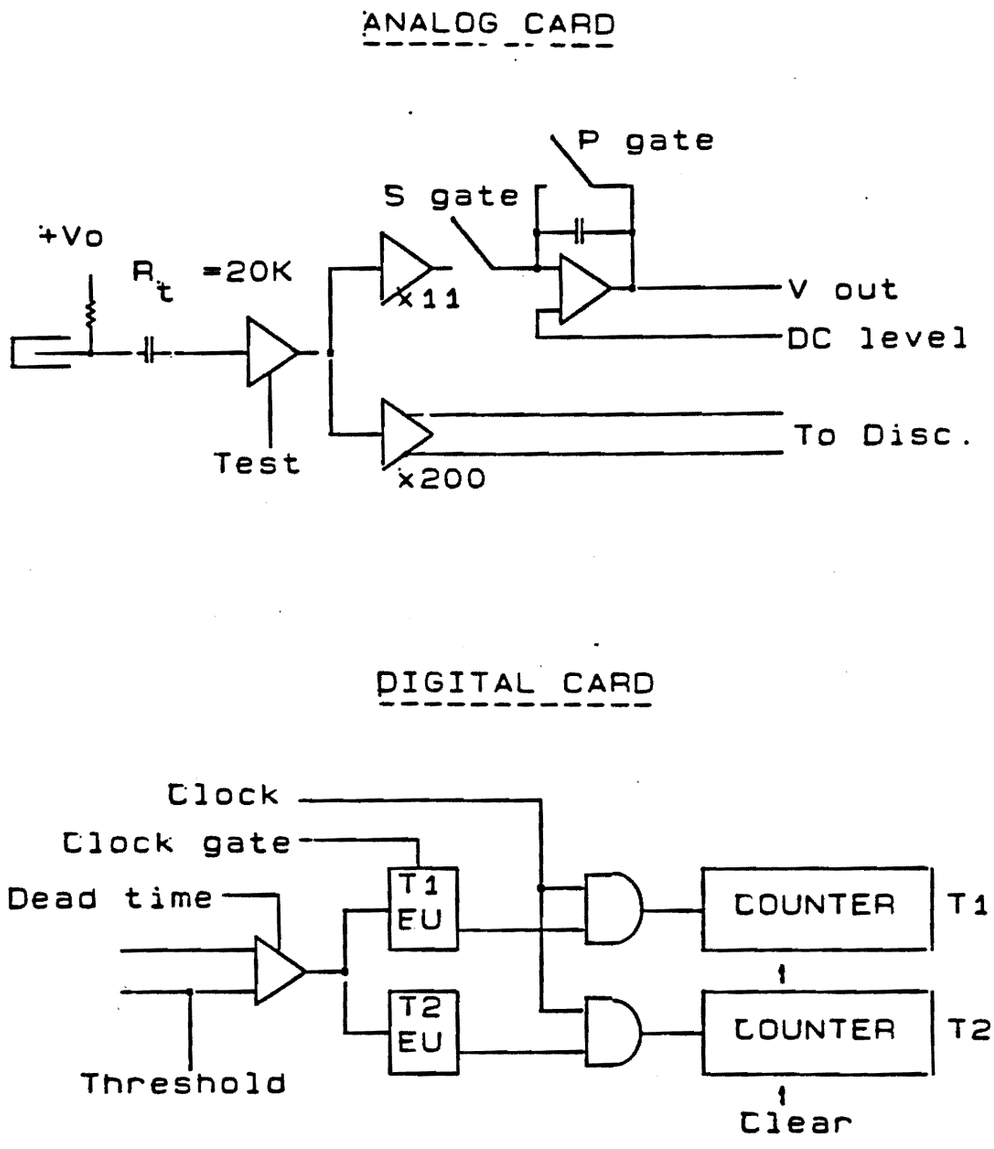

Figure 2.4.2 The PDT electronics

caused by slow drifts within each cell will not result in double hits. The output of the first preamplifier is also fed to a charge integrator through a second amplifier and a gate switch, S. During the master gate the gate S is turned on to permit the amplified signal current to flow to the charge integrator. The integrator is reset before the start of the master gate. At the end of the master gate, gate S is turned off and the integrator holds the accumulated charge until it can be read out and digitized by the scanner.

5. System Control

The operation of the detector required control and monitoring of each system within the detector. The detector system was organized in four sections. Each section consisted of 32 identical modules composed of one plane of calorimeters and its two adjacent planes of PDTs (X and Y), except for the last section which contained only 16 modules and included the gamma catcher and muon spectrometer. Each section contained three custom built scanners, LSI-11 microprocessor, timing and gating box, monitor interface and associated power supplies. The overall organization for the data acquisition system is illustrated in Fig. 2.5.1.

Within each section, there were one calorimeter scanner and two PDT scanners. The calorimeter scanner controlled 32 calorimeter planes, readout logic and cosmic ray trigger logic. Each PDT scanner controlled 16 pairs of X-Y planes including readout logic, diagnostic pulser, and cosmic ray trigger logic. The scanners were cabled directly to each plane of the detector electronics via a parallel data bus. The scanners were designed to provide the lowest level of control for the detector. Each scanner asynchronously collected, read out and digitized the data from each detector element flagged as being hit at the end of the $10\mu s$ beam gate. The data from each scanner was passed by DMA link directly to the LSI-11 microprocessor controling each section.

Each microprocessor was responsible for programming scanners for particular readout conditions and collecting the detector data from the scanners. This programming scheme for the scanners provided flexibility in data taking. The

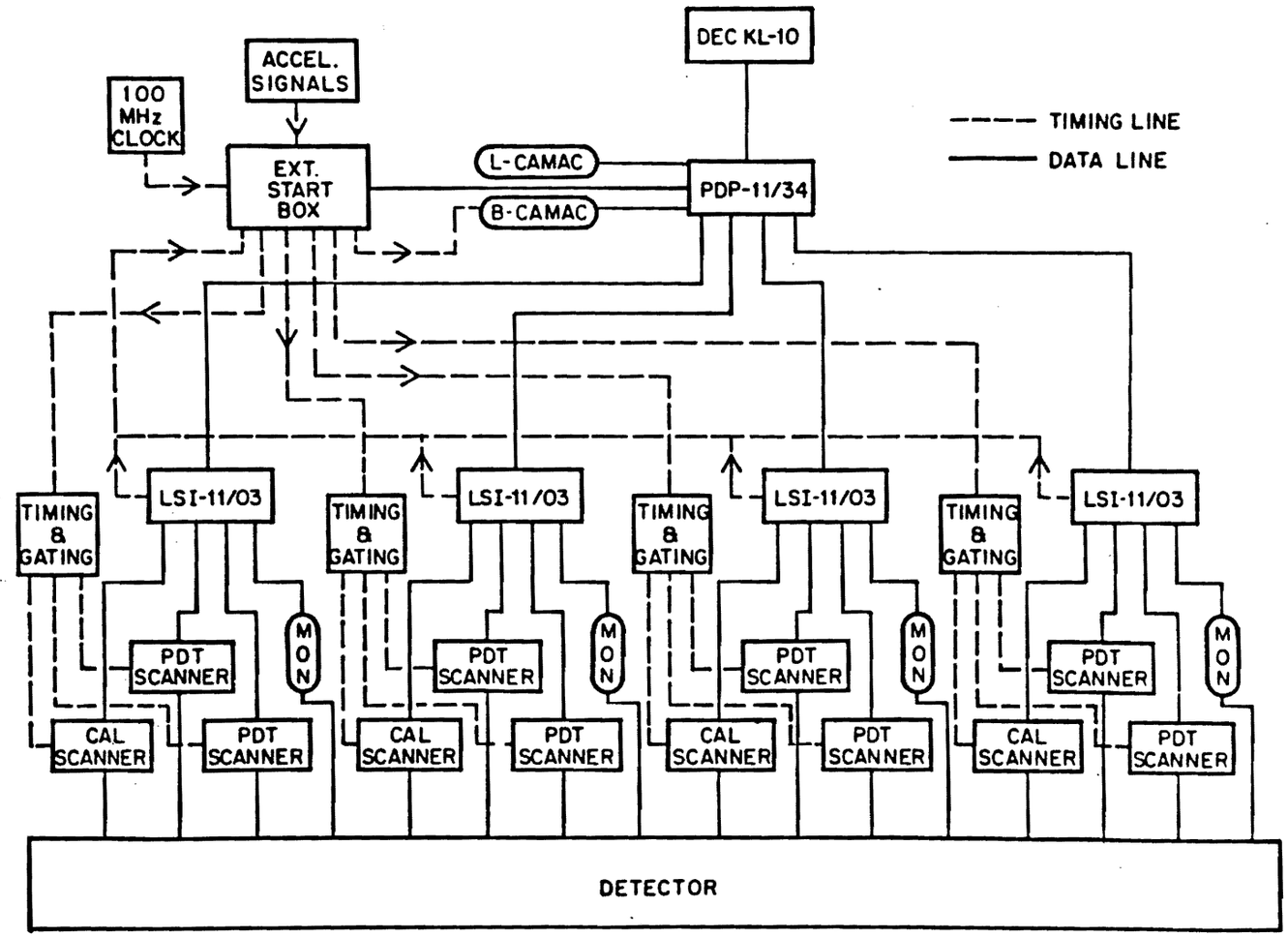

Figure 2.5.1 The E734 data acquisition system

microprocessor maitained two sets of scanner programming conditions, one set for beam running, and the other set for controlling calibrations or cosmic ray data collection. Between beam spills at the AGS, the microprocessors would activate the non-beam programming conditions to perform calibrations or diagnostics. This enabled efficient use of running time to maximize the time allocated for beam data taking. Upon receipt of the pre-beam interrupt signal from the AGS (which arrives 10 ms prior to beam extraction), all ongoing tasks were aborted and the beam tables reactivated to prepare for the next beam arrival. After completion of the beam task, data readout and transfer, the non-beam tasks were reactivated.

The microprocessors contained several D/A boards to control discriminator thresholds and various calibration parameters. The microprocessor also contained a 64 channel A/D to monitor temperature sensors and all power supply voltages and currents associated with that section of the dectector. These quantities were continually compared to values stored in the microprocessor. If any of the monitored quantities fell outside the tolerances assign to each nominal value, the shift operator was signalled to investigate.

Overall system control was managed by a PDP-11/34 computer. The 11/34 served as the primary operator interface for controlling the experiment. It also served as the final stage of data acquisition. The 11/34 was equipped with 128 kbytes of memory, 2 RK05 disk drives, 2 RX01 floppy drives, 2 1600 BPI tape drives, 4 MATROX video graphic displays and a printer/plotter. The 11/34 was interfaced to the four LSI-11/03 through 500 kbytes/sec parallel links and to a remote computer through a 30 kbytes/sec serial link. Two CAMAC crates were attached to the 11/34 to provide AGS information and calorimeter light pulser information.

The software operation of the detector was controlled by the online program MULCH running on the 11/34 under RT-11. MULCH is a version of the Fermilab RTMULTI [23] with extensive additions to the data acquisition and analysis sections [24]. MULCH included additional graphic display drivers and transfer routines to establish a link to the remote analysis computer. From the 11/34 console an

operator could initiate through MULCH beam data collection, calibration tasks, cosmic ray collection or monitor system wide information as well as play back any data previously store on magnetic tape.

As data was collected from the microprocessors, it was reformatted and written on to magnetic tape by the acquisition system within MULCH. MULCH would then sample events, for display analysis within MULCH, and to transfer to the remote KL10 computer for extensive online analysis. The KL10 provided the ability to perform diagnostic studies on the detector as well as assemble calibration information for elements of the detector.

6. Calibrations

Of great importance for the sucessful operation of this experiment is the monitoring and calibration of the individual systems within the detector. The detector was designed to facilitate this process by being able to execute various diagnostic and calibration tasks between beam spills. Calibration information was continuously assembled over time for the various detection systems. Any problems with elements within the detector could be quickly identified and investigated. In addition, critical parameters of the detector, such as temperature and power supply voltage, were monitored continuously during and selectively between beam spills.

There were four basic calibration tasks. The first involved the observation of cosmic rays passing horizontally through subsections of the detector. Both PDT and calorimeter performance could be studied by this technique. The second calibration task consisted of electronically pulsing the input stage of the PDT electronics to determine the performance of the PDT electronics. The third calibration task involved feeding the light pulse from an electronically controlled spark gap into the end of each calorimeter cell via a fiber optic cable. And the fourth calibration task involved the observation of vertical cosmic rays in the calorimeter cells. This information was used to determine light attenuation lengths within each calorimeter cell.

A cosmic ray trigger was built into the calorimeter scanner. It was designed to fire when consecutive planes of calorimeters within a specified block were hit. Each block was composed of groups of four modules. Within each group of four only three modules were required to be hit to form the cosmic ray trigger. This would allow the trigger to function even if an entire plane of calorimters was malfunctioning. The size of each block could be specified by software to enable the trigger to fire upon detection of cosmic rays 8, 16, 24, or 32 modules in length. In addition, the trigger could require coincidence between sections of the detector in order to fire.

The cosmic ray data was used primarily to determine plane and element efficiencies. A line would be fit to the wire positions of a cosmic ray trace in the detector. Each PDT and calorimeter cell within one cell width of the cosmic ray trajectory was checked for a hit. The efficiency was then the frequency at which a particular cell indicated a hit when both adjacent planes contained good hits. This efficiency data was available on-line during data runs and was used as a diagnostic to identify detector problems for investigation and repair. Cosmic ray pulse height information was also collected and used to monitor PDT and calorimeter power supply performance. In a similar fashion, beam muons collected during beam data taking could also be used for diagnostic and calibration purposes.

To calibrate and test the PDT electronics, a controlled signal from a pulser was introduced into the first stage preamplifier of each PDT channel. This PDT pulser could be operated in three different calibration modes to measure various performance aspects of the PDT electronics. The first mode fed two pulses of known amplitude at specific times into the PDT input stage. The readout times and integrated charges were then compared against known values for each channel. The second mode involved pulsing the electronics with a very small amplitude signal to trigger the charge integrator. The amplitude of the signal was small enough to not contribute to the charge integration compared to the pedestal value. Therefore the integrated charges readout in this mode determined the charge pedestal. The third mode used multiple pulses of varying amplitude

to determine the functional relationship between input pulse height and charge integration. Extrapolating this function to zero provided a second determination of the charge pedestal which was consistent with the previous method.

To calibrate the calorimeter system, a controlled pulse of light was fed into each calorimeter cell via the fiber optic cables mounted in each end cap. The light pulse was produced by a high voltage spark gap viewed by the fiber optic cables inside a light tight box. There were four modes of operation for the light pulser to calibrate various aspects of the calorimeter system. The first mode involved pulsing each group of calorimeter cells with the maximum possible light output. A vacuum photodiode observed the same pulse to provide a time and charge reference for the calibration. The firing times of the calorimeter PMTs were then compared to the firing time of the vacuum photodiode. The time difference corresponded to the time pedestal for each PMT channel. This process also served to identify bad PMT channels. The next two modes of calibration involved filter settings in front of the spark gap. One mode operated a one filter setting. The integrated charge readout from each PMT from this mode would then be compared to standard values determined from previous studies. The other mode used three different filter settings to determine the linearity of the charge integration circuitry. The fourth mode was a special mode to determine the charge pedestal for each PMT. Selectively (left or right) each PMT was disabled by lowering the power supply voltage. Then the light pulser was operated. Since a hit on either PMT enables charge integration for both PMTs, the measured charge on the disabled PMT would then correspond to the charge pedestal for the PMT electronics.

The fourth calibration task involved the observation of cosmic rays traveling vertically throught the calorimeter planes. The vertical cosmic ray trigger required the majority of cells in one calorimeter plane to register a hit. The horizontal position of the cosmic ray within each cell was then determined by the timing difference between the two PMTs to within 10 cm. The position was later refined using long muons and PDT hit positions. Once the x position of the cosmic ray was known, the profile of charge versus distance for each PMT was accumulated.

This data was then fit to the functional relation,

$$Q(x) = A(e^{-x/L} + B)$$

where A is the overall gain of the PMT, B is the charge pedestal for the PMT, and L corresponds to the measured attenuation of light within the cell[21].

7. Test Beam

A subsection of the detector was installed in a charged particle test beam at the AGS. The subsection consisted of nine, main detector modules (x,y PDT and calorimeter) with ten gamma catcher modules (lead-calorimeter). Additional instrumentation was installed to identify beam particles by energy and time of flight. This included two cherenkov counters and three plastic scintillators upstream of the test beam detector. The farthest two plastic scintillators were spaced 31 meters apart allowing for very good separation of protons, pions and electrons from time of flight. The two cherenkov counters were used to identify unambiguously electrons in the beam. Also included upstream were 24 planes of thin beam chambers similar in construction to the detector PDT planes. These beam chambers were positioned in the beam to provide accurate determination of the trajectories of beam particles traveling into the detector.

The test beam provided the spectrum of charge particle types from 0.4 GeV to 5.0 GeV. The beam polarity could be selected by the polarity of the upsteam AGS beam magnets. The particle momentum was selected by a dipole magnet positioned upstream in the test beam line. The selected momentum was bent through a 6 degree angle by the magnet in order to enter the detector and coincident the trigger.

Data were taken for several particle types and momentum ranges. This information was used to establish ionization profiles for different particle types moving through the detector. Of particular importance for the electron analysis was the energy and angular resolution for electrons in the detector. Studies of incident electron angle versus reconstructed angle in the detector as well as studies

of electron energy versus observed visible energy were performed and discussed in detail in Ref. 25.

The kinematics for $\nu_\mu e \rightarrow \nu_\mu e$ scattering restrict the recoil electron to a very forward angle with respect to the incident neutrino. This forward recoil angle will provide a very strong signature for extracting the $\nu_\mu e \rightarrow \nu_\mu e$ signal from background. Therefore, the ability to measure the electron angle (i.e. angular resolution) must be well understood.

The angular resolution for electrons in this experiment was measured by comparing the known incident electron angle determined from the beam chambers to the angle measured by an interactive angle fit (discussed later) in each projection of the detector. This comparison was performed at three different electron energies of 0.4, 0.6 and 1.0 GeV in order to establish the energy dependence of the angular resolution. One hundred electron events were measured at each energy. The angular resolution function[25] was measured to be, for each projection

$$\Delta\theta_{x,y} = \frac{(13 \pm 1)\text{mrad}}{\sqrt{E_e[GeV]}}.$$

A plot illustrating the angular resolution functional dependence on energy is shown in Fig. 2.7.1.

The observed electron energy deposited in the detector had to be corrected for the inactive component of the detector mass. In addition, the ability to measure the electron energy, that is the resolution, also had to be well understood. This was accomplished with the test beam electron data. Beam electrons with energies of 0.4, 0.6, 0.8 and 1.0 GeV were observed in the detector. The deposited energy in the detector was then compared to the known energy of the electron specified by the upstream magnet selection. From this, the energy scale (correction) factor and the resolution function were determined. The electron energy resolution function was measured to be

$$\frac{\Delta E}{E} = \frac{0.13}{\sqrt{E[GeV]}}$$

and the scale factor to be 1.43 ± 0.14. A plot illustrating the electron energy resolution determination from the test beam data is shown in Fig. 2.7.2.

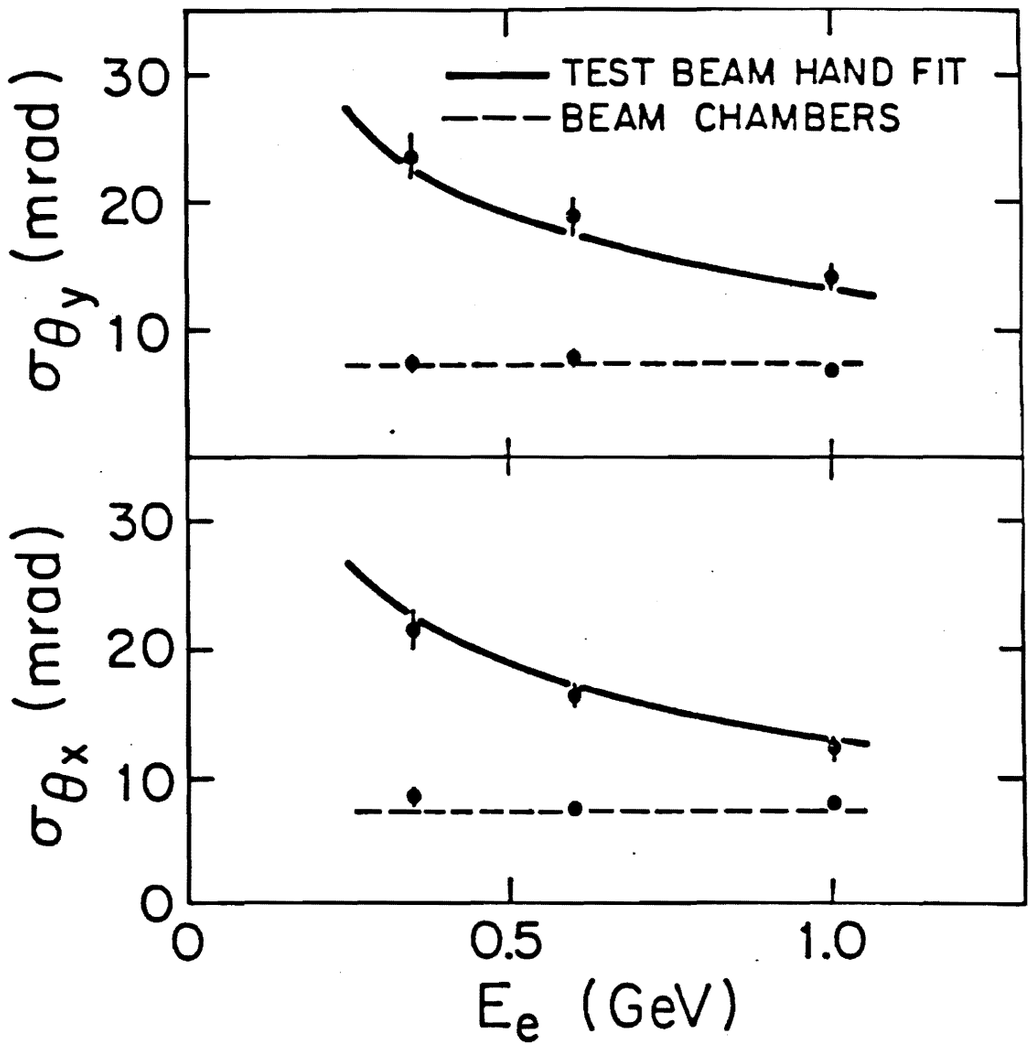

Figure 2.7.1 Angular resolution for test beam electrons

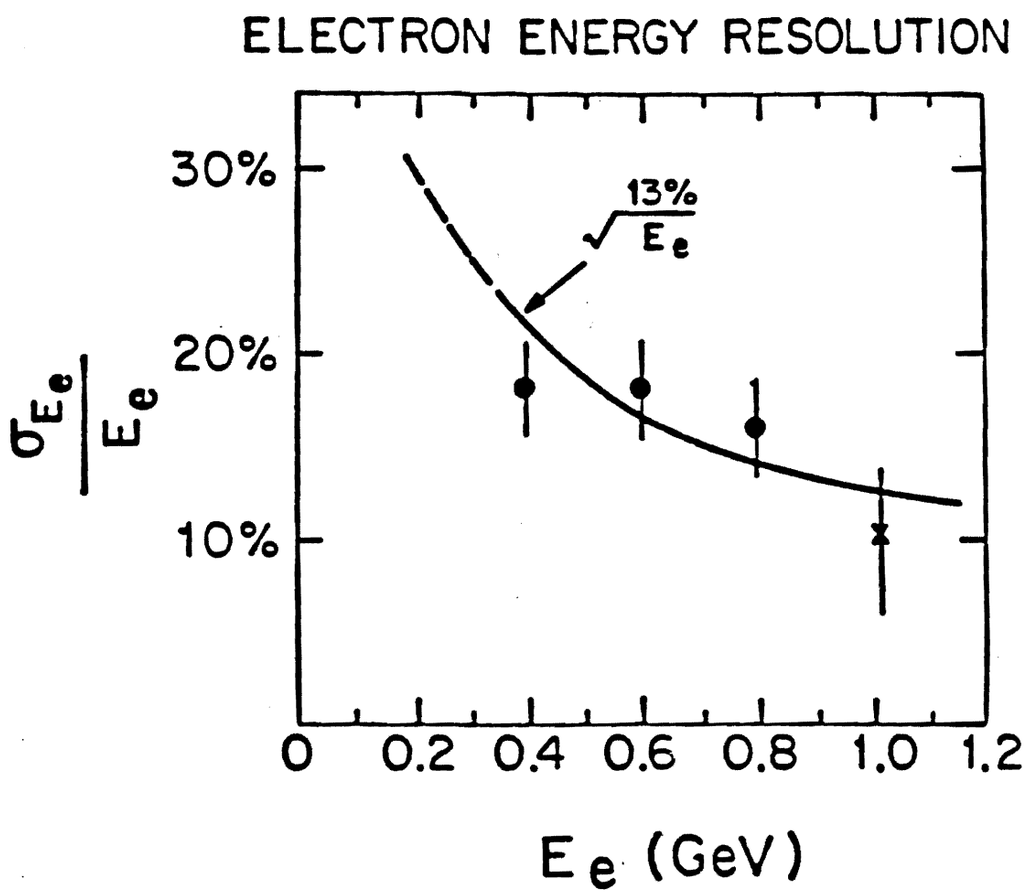

Figure 2.7.2 Energy resolution for test beam electrons

A Monte Carlo study of the scale factor was also performed by comparing the thrown energy of the electron from the Monte Carlo generator to the deposited energy in the main detector for 1000 generated events. The results were consistent with the test beam determination within 10%. A third study of the scale factor was also perform by kinematically reconstructing $\nu_e n \rightarrow e^- p$ events seen in the main detector. By comparing the expected energy of the electron to the deposited energy in the detector the scale factor was determined. This determination was also found to be consistent with the test beam determination cited above.

Chapter 3.

Data Reduction

Since becoming fully operational in 1981, the E734 apparatus has logged several thousand hours of exposure time in both neutrino and anti-neutrino wide band beams at the AGS. Two data sets corresponding to the neutrino and anti-neutrino exposures have been collected. The anti-neutrino data set consisted of 354 (800 BPI) and 325 (1600 BPI) raw data tapes corresponding to the 1981 and 1983 anti-neutrino exposures, respectively. The neutrino data set consisted of 371 (800 BPI) and 311 (1600 BPI) raw data tapes corresponding to the 1981 and 1983 neutrino exposures, respectively.

The 1981 portion of the neutrino data has been analyzed with regard to $\nu_\mu e \rightarrow \nu_\mu e$ elastic scattering and 51 events have been observed. The results are reported in Ref. 26 and detailed in Ref. 27. The 1981 and 1983 anti-neutrino data set has been analyzed with regard to $\bar{\nu}_\mu e \rightarrow \bar{\nu}_\mu e$ elastic scattering and 55 events have been observed. The results are reported in Ref. 28 and detailed in Ref. 25. However, the anti-neutrino analysis resulted in significant improvements in the analysis process (see Ref. 25). In light of this new analysis procedure, it was determined that the 1981 neutrino data set should be re-analyzed along with the yet to be analyzed 1983 neutrino data set in order to fully exploit all the data. This analysis of the 1983 neutrino data set along with the re-analysis of the 1981 neutrino data set and its combination with the results from the previous anti-neutrino analysis is the subject of this thesis.

The combined 1981 and 1983 neutrino data sets represented over 3 million AGS bursts. The number of signal $\nu_\mu e \rightarrow \nu_\mu e$ events expected is on the order of 100. The need for extensive data reduction is obvious. This was accomplished in several steps beginning with the NUE/FELIX production. The complete analysis process is diagrammed in Table 3.1 along with the data reduction summaries.

analysis stage	1981 ν_μ	1983 ν_μ	combined
POT	7.61×10^{18}	1.60×10^{19}	2.36×10^{19}
PDT filter	171,114	356,272	527,386
$\theta_{PDT} < 0.2$	80,922	178,384	259,306
1st eye scan	6,813	15,884	22,697
2nd eye scan	3,095	5,685	8,778
analysis cuts	1,118	1,924	3,042
tube cut	582	963	1,545
e/γ cut	356	641	977
$\theta^2 < 0.03$	256	460	716

Table 3.1 The electron analysis procedure

1. NUE Production Program

Once the raw data had been collected and stored on magnetic tape, it had to be processed into a form which would facilitate further analysis. This was performed by the FORTRAN program NUE. NUE ran as a FELIX batch process on the CDC 7600 at BNL. NUE produced output streams for all the data sets that would be used by the experiment including the two data sets used for the measurement of the neutrino electron elastic cross section: the neutrino electron signal data set and the quasi-elastic normalization data set.

Raw data tapes were read by NUE along with the necessary detector calibration files (produced on the KL10 computer) and geometry files. The calibration and geometry files contained the pedestals, gains, time offsets and coordinate positions for each element in the detector. Once read in, NUE unpacked the data and stored it in FORTRAN COMMON blocks. Next, all raw charge and timing information for each detector element in the data was corrected and normalized using the information from the calibration files. The x-position of the hit within each calorimeter cell was determined from the relative triggered times of the cell's photomultiplier tubes.

Next, the calorimeter hits were clustered in time. The time clustering consisted of placing the calorimeter elements in time bins of 40 ns and then correlating

all nonzero bins within two time bins of each other. PDT elements were then associated with a time cluster by correlating the PDT time with the mean time of the cluster. A PDT could be associated with up to three different time clusters.

Once all elements had been associated in time, two dimensional track fitting could be performed with PDT hits. The track fitting algorithm would start by locating the upstream end of a track as the first combination of 3 PDT hits out of five consecutive planes which lay in a straight line. The algorithm then iterated along the line until it had associated all appropriate PDT hits with the track. This was done for all tracks in each view for all time clusters. After all tracks had been identified, the scintillators were used to correlate PDT hits in each track with a correct time cluster. Then tracks from both views were matched in 3 dimensions by using vertex and track length to form a 3 dimensional track.

The next step in NUE was to use the PDT drift distances to refit the 2 dimensional tracks previously obtained. The drift distance is obtained from the time difference between the PDT trigger time and the trigger time of the nearest associated scintillator. This time difference is known as the drift time. Each drift distance has an ambiguity as to which side of the PDT wire the particle passed. To resolve this, a "tree" algorithm was used to determine the appropriate combination of drift distance for the best line fit. With all tracks refit, NUE then associates multiple 3 dimensional tracks with a common vertex. This corresponds to identifying multi-prong interactions.

Once NUE had fully reconstructed an "event", the results were spoolled out to a data summmary tape (DST) in a standardized format which would facilitate further analysis. The quasi-elastic data set was obtained from these data summary tapes.

2. The PDT Filter

The PDT filter [25] is a subroutine in the NUE production program. The subroutine's function is to select electromagnetic shower candidates from the raw data sample and output them onto tape. Its operation is independent of any

trackfinding analysis in NUE and has no effect on its operation. The filter makes use of the energy and time clustering information from NUE for each event. The filter was designed to be able to separate and identify multiple electromagnetic showers in a given time cluster. To do this, the filter exploited PDT information to locate possible shower candidates. The PDT information was used instead of the calorimeter information, because of the PDTs superior spatial resolution.

An electromagnetic shower is an event which produces a large number of secondary particles as it moves through the detector. An example of an electromagnetic shower events is shown in Fig. 3.2.1. The secondary particles are mostly photons which convert into e^+e^- pairs. These pairs often have enough energy to continue pair production by bremsstrahlung radiation. The finite size of the PDTs in the detector does not permit the secondary particles to be distinguished individually from one another. Instead, the secondaries cause the number of elements hit per plane to increase along the particle's path. A typical 1 GeV shower produces an increase from one to four or five PDT hits per plane and an increase from one to about two or three calorimeter hits per plane over the length of the shower. Because a photon can travel several planes before converting, it is possible to have physically separated secondary showers associated with a primary shower upstream. These secondary showers can appear as separated showers or as single showers with spatial gaps. Smaller secondary showers can appear as energy deposits in individual calorimeter cells around the body of the main shower. For the filter to be effective, it has to be able to locate a candidate shower and determine if it fits the criteria of multiple hits per plane and gaps in the body of the shower.

The PDT filter relied on energy and timing information provided by NUE to process each event. For each time cluster within each event, the filter would locate the calorimeter planes which contained hits as the region to begin the search for possible showers. All PDT hits within this region and within 100 ns before and 1200 ns after the mean time of the cluster were summarized in a local array. PDT hits which were groups of nearest neighbors in a plane were averaged together to determine a mean hit position and error ($error = 8.0cm \times N_{PDT}/2$).

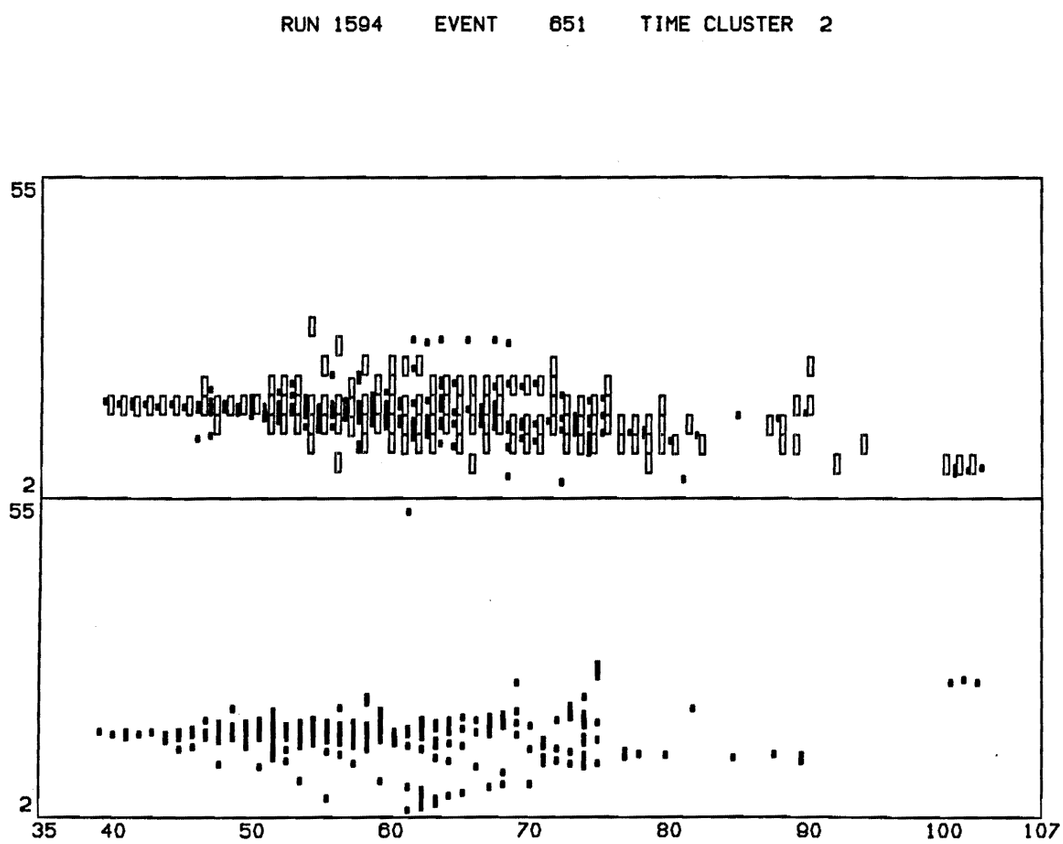

Figure 3.2.1 An example of an electromagnetic shower as indicated by a hit map of each projection of the detector

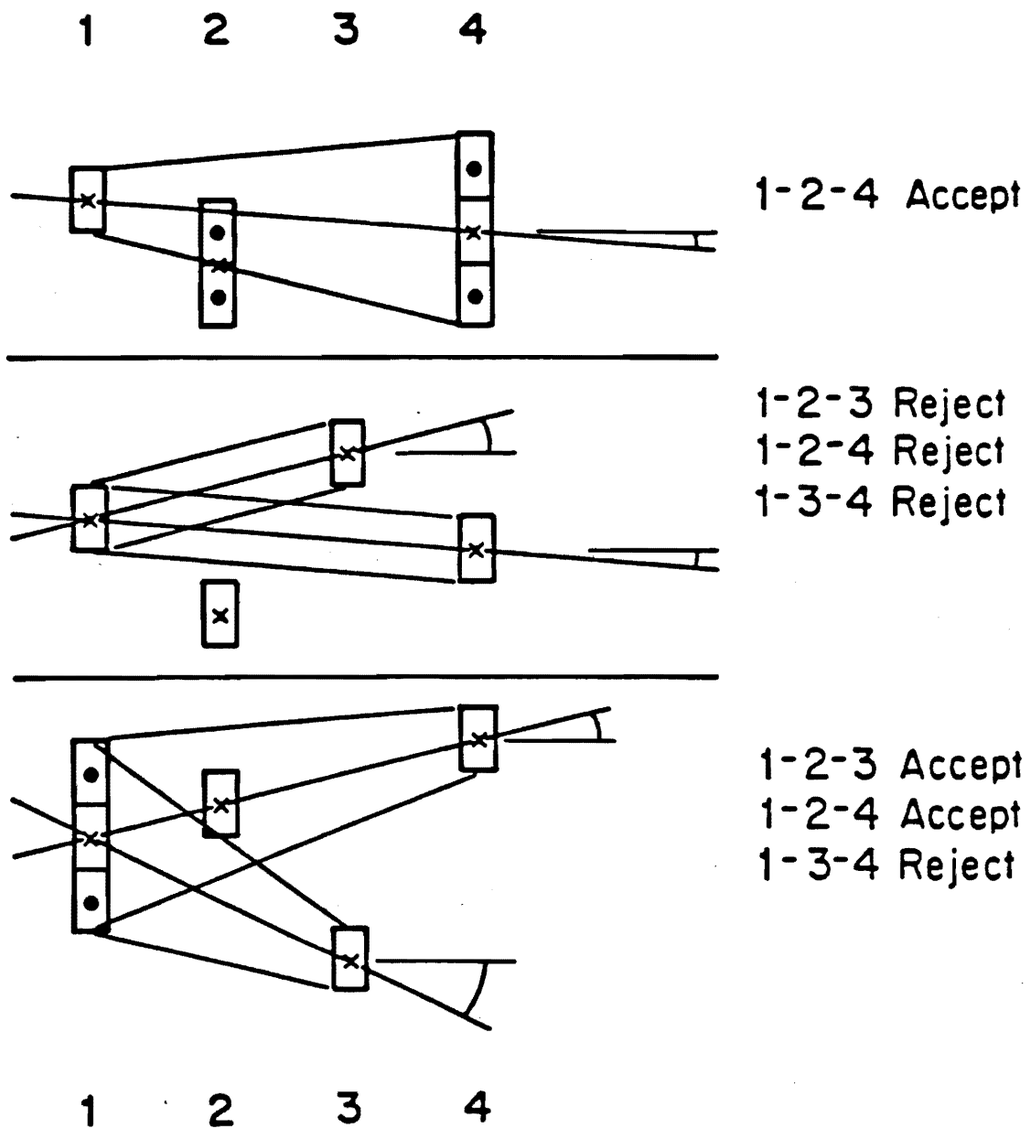

Figure 3.2.2 Sample vertex track patterns

All coordinates for fitting were based on PDT wire positions. The filter stepped through each plane in each view in the region until all groups of PDT hits were processed. The filter then considered all combinations of three PDT hit positions in four consecutive planes as a possible shower vertex. To reject side entering events, the filter required the first PDT hit position to be within a fiducial volume. The fiducial volume corresponded to the region between PDT wire position 3 and 53 (7.6 cm from the active edge of the PDT plane) in both the X and Y view. To test if any of the hit combinations could form a shower vertex, a line was fit through the first and third hit positions. This line was required to have a slope with respect to the beam direction of less than 0.5 to reject large angle events. The second hit position was required to be within the error of the second hit position plus the average error of the first and third hit positions (see Fig. 3.2.2). The planes in front of the vertex plane were checked to insure that the filter had located the front of a shower candidate. The vertex candidate was rejected if the first upstream plane contained any PDT hits within 16 cm of the fit line in either view or if there was a calorimeter hit within 20 cm in the Y view.

Once a vertex candidate was established, other groups of PDT hits downstream of the vertex were checked for association. For a PDT group to be considered part of a shower it had to lie within a road defined by

$$\Delta x < 8.0cm \times N_{HITS}/2 + 0.06 \times \Delta z + 8.0cm$$

or

$$\Delta x < 8.0cm \times N_{HITS}/2 + 20.0cm$$

where Δx is the transverse distance of the PDT group to the trial line and Δz is the downstream distance of the PDT group from the vertex. The first term to the right of each inequality corresponds to the error on the position of each PDT group. The second term to the right of the first inequality corresponds to a simple model for multiple scattering. The PDT groups that met these conditions were considered part of the shower and were included in a later recalculation of the trial line. The filter continued to move downstream until it encountered a plane

with no PDT hits within the road in either view. The filter then recalculated the fit line based on the associated PDT groups previously established. The process of searching for PDT hits within the road downstream of of the vertex group was then repeated with the new trial line. This process was then iterated three more times. A program study indicated that most trial lines converged to a stable solution within four iterations. After each iteration the shower candidate was checked against all other candiates prevously identified to insure that the same shower was not found twice.

After the last trial line iteration for a shower, a check was made upstream of the vertex for associated PDT hits. If any there were any PDT hits within 12 cm of the trial line the shower was rejected. The filter further required that the shower be at least three modules long in each view and that the shower length in each view be within four modules of each other. This was to insure that the shower projections matched in each view. The filter then flagged all associated PDT hits with a shower to prevent these PDT hits from being used to find vertices downstream. Other PDT and calorimeter hits were then checked for association with the shower. Any PDT or calorimeter hits which were within two modules upstream of the vertex and 15 modules downstream of the end of the trial line and within a road were considered associated. The road for associated calorimeter hits was

$$\Delta x < 50.0cm \times N_{cells}/2 + 0.06 \times \Delta z + 8.0cm$$

or

$$\Delta x < 50.0cm \times N_{cells}/2 + 45.0cm$$

and the road for associated PDT hits was

$$\Delta x < 8.0cm \times N_{PDTS}/2 + 0.06 \times \Delta z + 8.0cm$$

or

$$\Delta x < 8.0cm \times N_{PDTS}/2 + 45.0cm$$

where Δx is the transverse distance of the PDT or calorimeter to the trial line and Δz is the downstream distance of the element from the vertex. The first term

to the right of each inequality corresponds to the position uncertainty within each element. The second term to the right of each inequality represents a simple model for multiple scattering effects.

Once all elements for a shower were assembled, angle and energy cuts could be performed. The first estimate of the shower angle was calculated from the final trial line from each view. The energy in the first two vertex planes, E_{vtx1} and E_{vtx2} (where the first plane was defined as the first plane with a calorimeter hit) were calculated by summing up the associated calorimeter energy in each plane. The total visible energy, E_{TOT} for the shower was calculated from the sum of all calorimeter hits associated with the shower. A shower candidate was rejected if it failed any of the following requirements:

$$\theta_{PDT} < 0.35 Rads$$

$$E_{vtx1} < 60 MeV$$

$$E_{vtx2} < 60 MeV$$

$$E_{TOT} > 100 MeV.$$

These requirements were designed to eliminate candidates which could not be single electrons. Since electron events are kinematically constrained to very small angles, the angle cut was used to eliminate large angle background events. The vertex energy cuts eliminated multi-prong events which would deposit more energy at the vertex. And the visible energy cut limited the number of low energy showers which are very often short, difficult to identify and dominated by background.

Candidate showers were then checked for gaps. If a shower had calorimeter hits downstream of the end of the trial line the shower was considered to have gaps. Next a test was made for multiple hits per plane. The test was done by counting the number of planes with more than one calorimeter hit (M), with one hit (S) and with zero hits (Z). A shower was considered to have multiple hits if it satisfied the following conditions:

$$M + S > Z$$

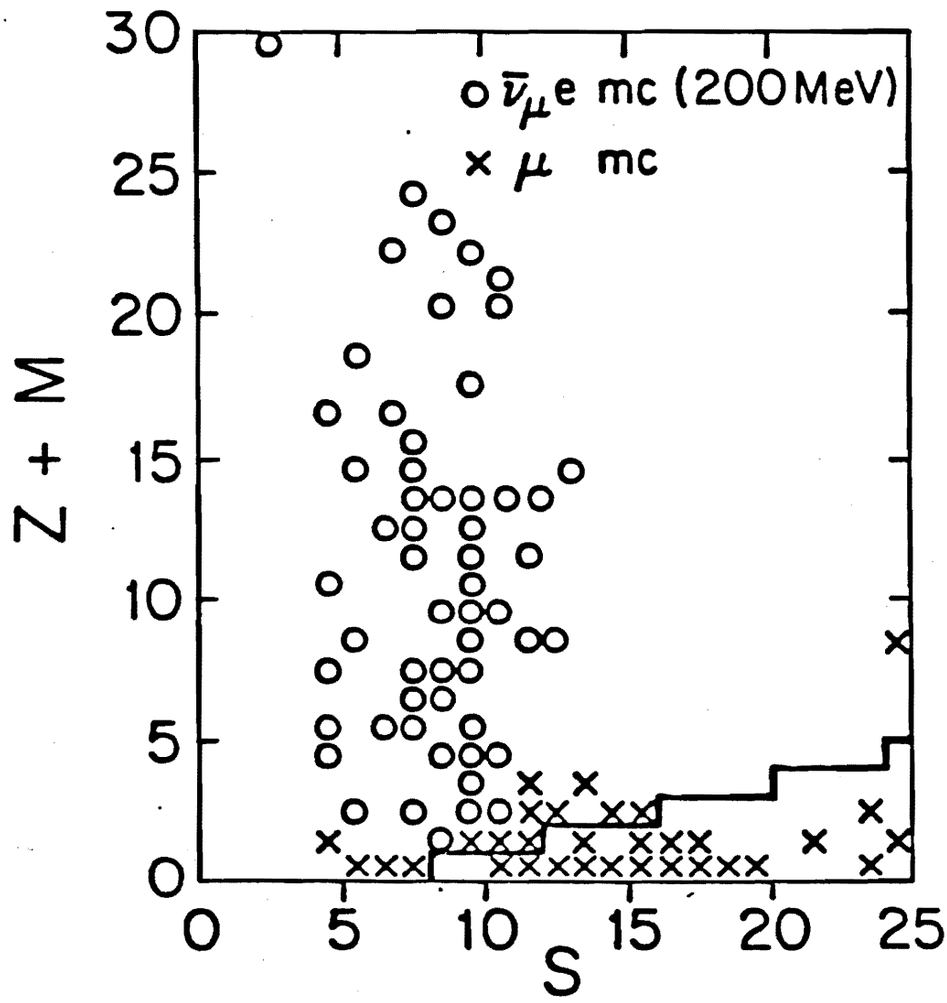

Figure 3.2.3 Multiple Hit Criterion

and

$$M + Z > S/4 - 2.$$

A Monte Carlo study [27,29] of hit patterns of muons and electrons indicated that muons tend to have only a single calorimeter hit per plane while electrons have multiple hits per plane. The results of this study are shown in Fig. 3.2.3. Candidate showers were then checked for containment. Any shower with did not exit the side of the fiducial volume in either view was considered to be contained. Any shower not satisfying any of the follow criteria was rejected: 1) The shower was contained and had gaps, 2) The shower was greater than 40 modules long, had gaps and had multiple hits, 3) The shower exited and had multiple hits.

Showers which passed these criteria were considered good candidates and were stored until the remainder of the time cluster was processed. The filter then proceded to analyze the next time cluster in the event until all time clusters were processed. Once an event had been processed, each time cluster which contained a good shower was output to tape along with information summarizing the shower.

The PDT filter was tested against the "scintillator" filter[27,29] used in previous analyses. The "scintillator" filter as its name implies used only calorimeter information to identify showers. It also rejected events which contained a possible second interaction or track within the time cluster of interest. However, it did provide a reasonable trial horse by which the PDT filter was tested. The results of the comparision are given in Ref. 25.

Chapter 4.

The Electron Analysis

The data were taken during the 1981 and 1983 wide band running periods at the AGS. 7.61×10^{18} POT and 1.60×10^{19} POT were delivered during each of these periods respectively. The collected data were written to 371 (800 BPI) and 311 (1600 BPI) raw data tapes before processing through NUE. From the NUE production program, the PDT filter identified 527,386 events as containing a candidate shower. These events were written to 48 (6250 BPI) data tapes for further electron analysis.

1. Eye Scan

After processing by the NUE production program, the data which passed the PDT shower filter had to be reduced further to fascilitate analysis. This was accomplished by a physicist observation of each event. Because of the difficulty and complexity of pattern recognition for electromagnetic showers with software and the need for very high signal acceptance, it was felt that an eyescan by physicists was the best way to procede.

The eyescan was prepared by first reading the output summary tapes from NUE and selecting only those events with a PDT shower angle, θ_{PDT} of less than 0.200 radians. The events with PDT shower angle of greater than 0.200 radians consisted mostly of muons and multi-prong interactions. This requirement reduced the number of events to be eyescaned by a factor of two from 527,386 events to 259,306 events. Line printer plots were made of each event along with an event summary kept in a separate file. The plots were output onto micro fiche to provide a convenient form to eyescan (see Fig. 4.1.1). Along with the events, Monte Carlo simulated events were randomly interspersed at the 2% level as a control on eyescanning efficiency.

The Monte Carlo events were overlaid onto trigger and background events randomly selected from both the 1981 and 1983 neutrino running periods. The

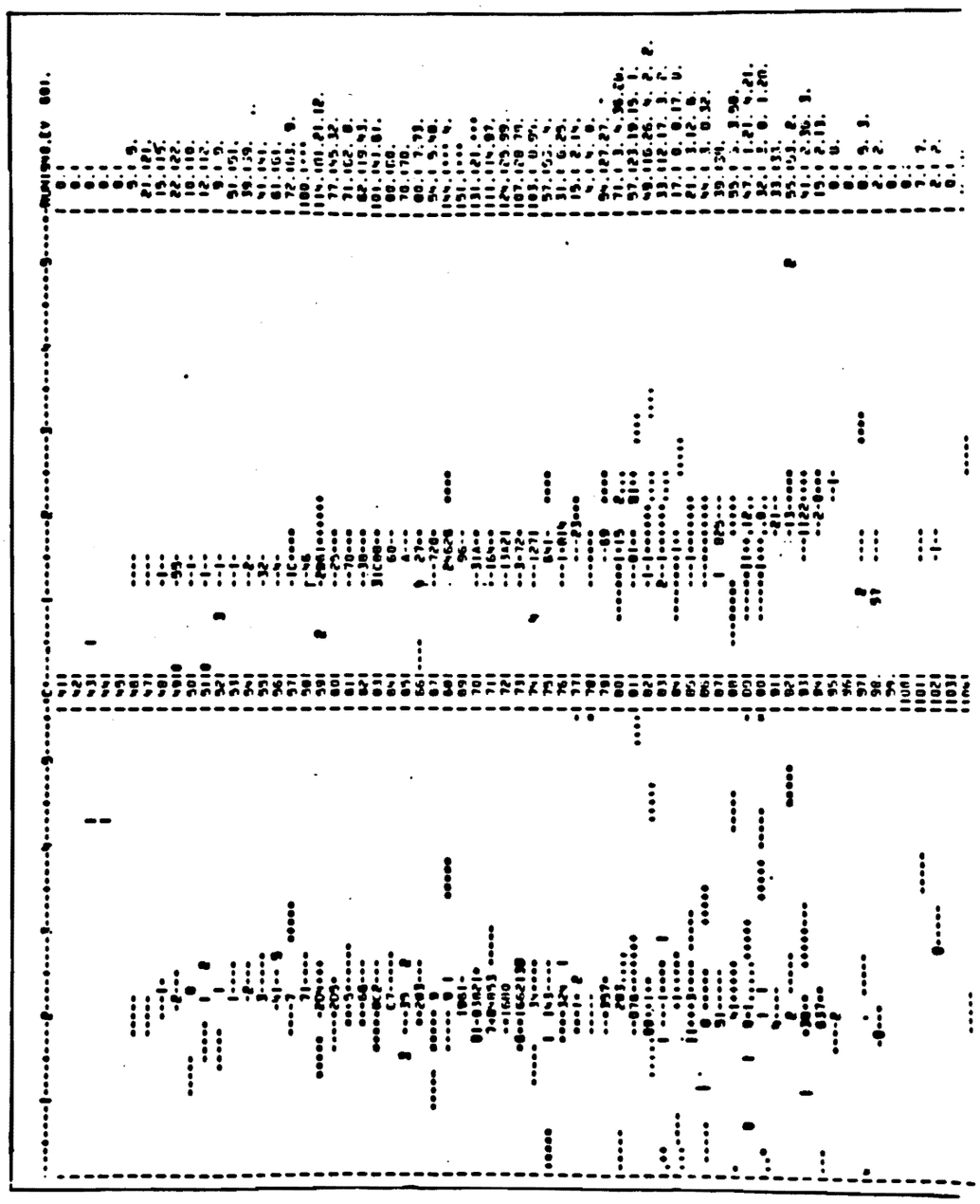

Figure 4.1.1 Display of a shower candidate from the eyescan as indicated by a symbolic hit map of each detector projection

Monte Carlo events were positioned in time to correspond to one of the twelve time buckets of the beam with the same 30ns FWHM distribution within the bucket. Energy and timing inefficiencies were added to the Monte Carlo events to more closely emulate real candidate events.

Each event was then scanned twice by two separate physicists (see appendix 1 for scan rules). The physicists were given no information as to which hits the PDT filter had chosen as a shower candidate. The physicist job was to identify any electromagnetic showers in the event frame. If an event frame contained no electromagnetic shower candidates it was then rejected.

Once a physicist located a shower candidate it was checked for possible associations with other interactions in the same time cluster. If a shower had other tracks originating from its vertex as seen in both views of the event, it was to be rejected. Shower candidates that were accepted were then classified into two categories, "electron/gamma" or "stub".

Electron/gamma candidates were showers judged as being possible signal events with no association to other activity in the time cluster. Stub candidates were showers with a clear association with an upstream energy deposit in the scintillators. Stub events were cases where the shower may have been caused by a photon from the decay of a π^0 where the π^0 was produced by an interaction at the position of the upstream scintillator hits.

Once all events have been double scanned, the electron/gamma results were "OR"ed (including Monte Carlo events) to produce a condensed sample of shower candidates which were replotted for a second eyescanning session. This sample was again doubled scanned. There were again two categories of candidates. The first were "electron" type. These were the signal events which would be processed for later analysis. The second were the "stub" candidates which were later used for background studies. Once the scan was completed any discrepancies between the two scanners were resolved by a joint session between the two scanning groups.

The first eyescan involved the participation of ten physicists working over a period of several weeks. The first eyescan process reduce the number of candidate events from 259,306 events to 22,697 events. Two groups of two or more physicists were formed to perform the second eyescan. The second eyescan condensed the 22,697 events into 8,778 candidate electron events and 1,475 stub events.

2. Signal Analysis

Once the eyescan was complete, the "electron" and "stub" events were stripped into a condensed data set. Each data set was processed through a program which recalculates the initial angle and total energy of each candidate electromagnetic shower. The program reruns the PDT shower filter to summarize each shower in each event. It then locates that shower the eyescannner had identified. If it did not find the scanner's shower, it would select the largest shower (most PDT hits) it found in that event. Once the shower was identified, the program would re-evaluate the shower angle based on a least squares fit. The fit would encompass all possible combinations of PDT hits with weighted uncertainties based on the effects of multiple scattering as the shower evolves in the detector. Other important quantities concerning the shower were also determined. All this information was assembled into a new common data block. This information was then summarized into a standard format DST file.

After the eyescan selected events had been processed and summarized, studies were done to verify the appropriateness of the energy scale factor previously determined from test beam studies. The energy scale factor corrects the observed detector energies to the actual energy. This factor accounts for the nonactive component of a detector mass as well as the overall scale for energy measurements. By studying dE/dx distributions of beam muons in the detector the energy scale was found to vary by less than 10% over time (see Fig. 4.2.1). The test beam energy scale factor was then used for this data set.

After the energy studies on the data sample were complete, fiducial volume and energy cuts were applied to further condense the size of the event sample.

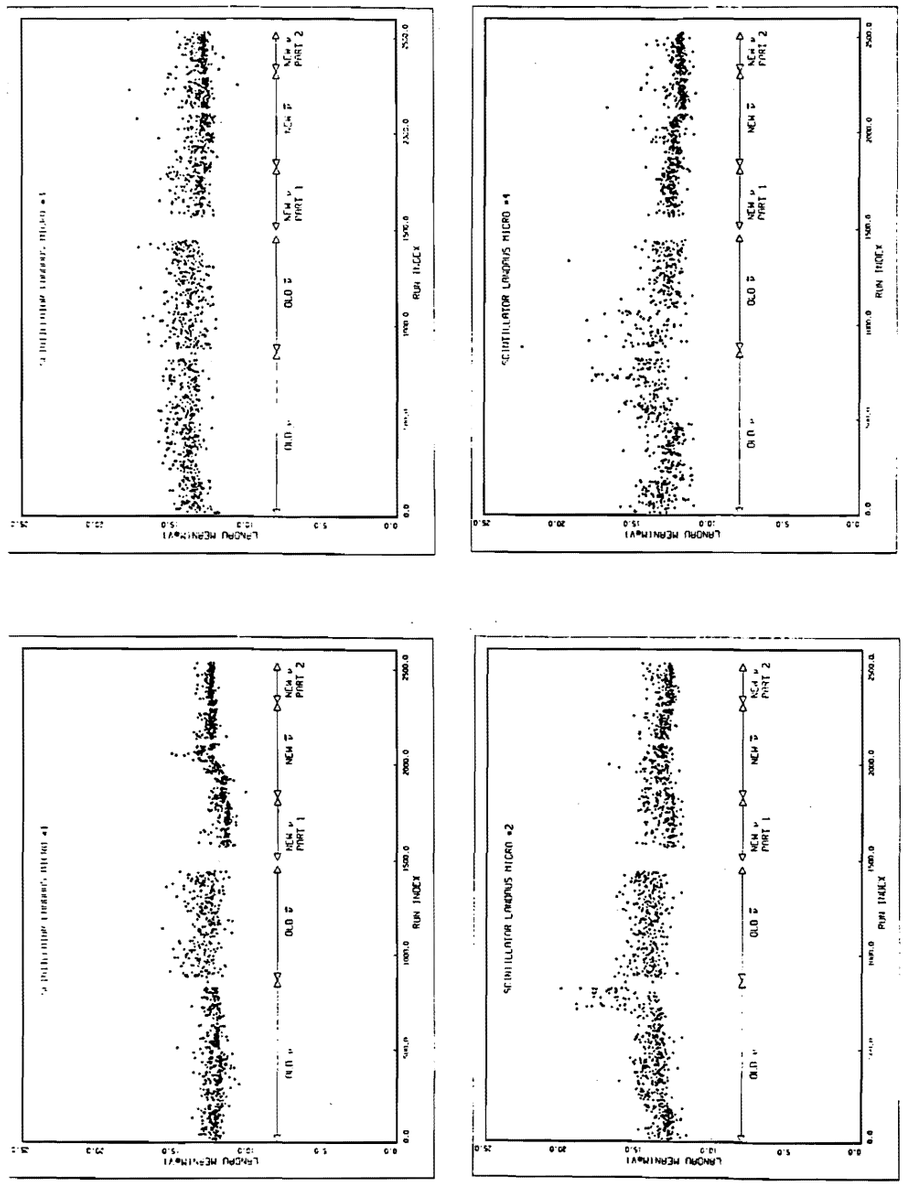

Figure 4.2.1 Plot of the mean dE/dx values for the calorimeters over time

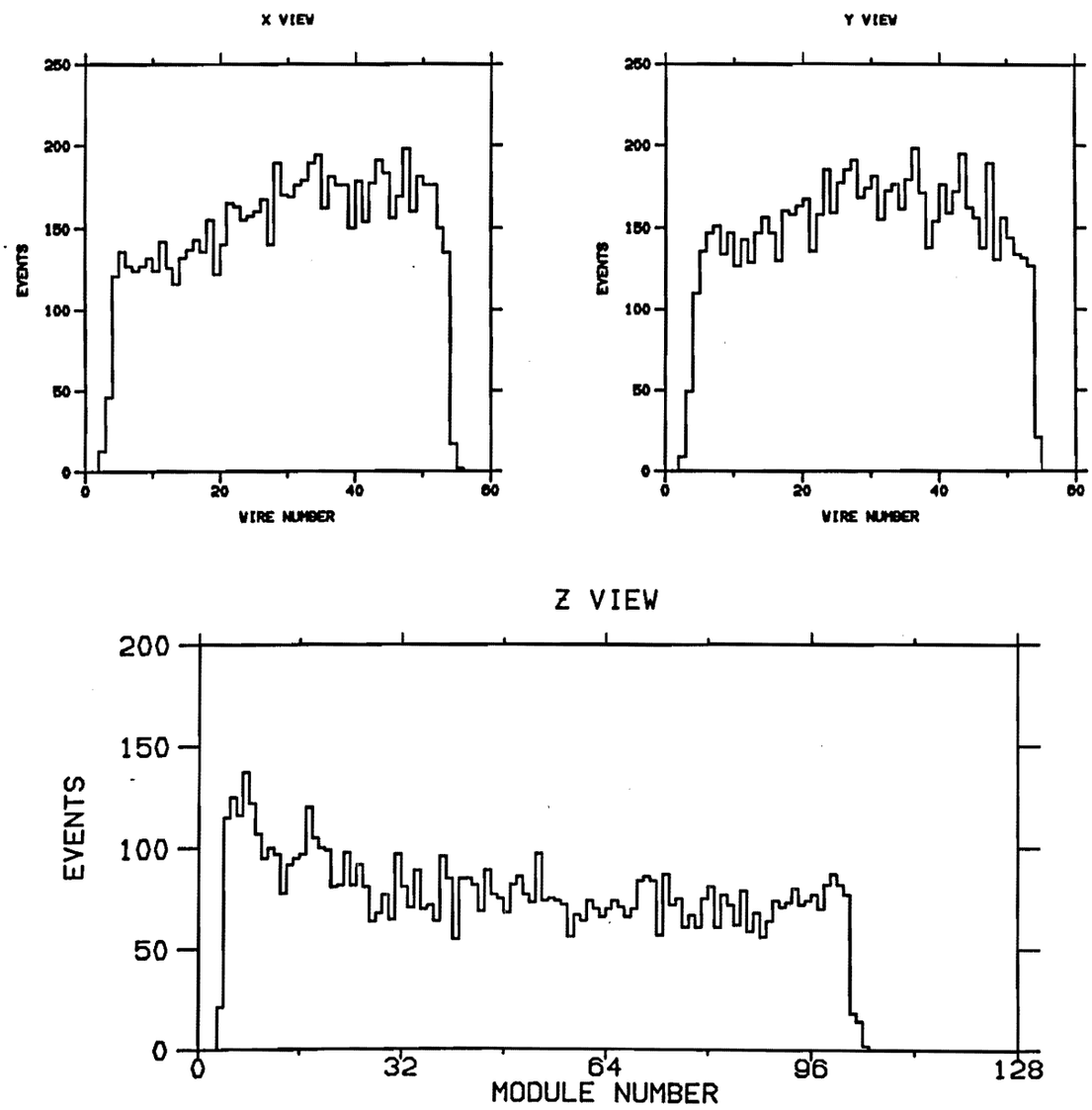

Figure 4.2.2 Distribution of event vertex positions

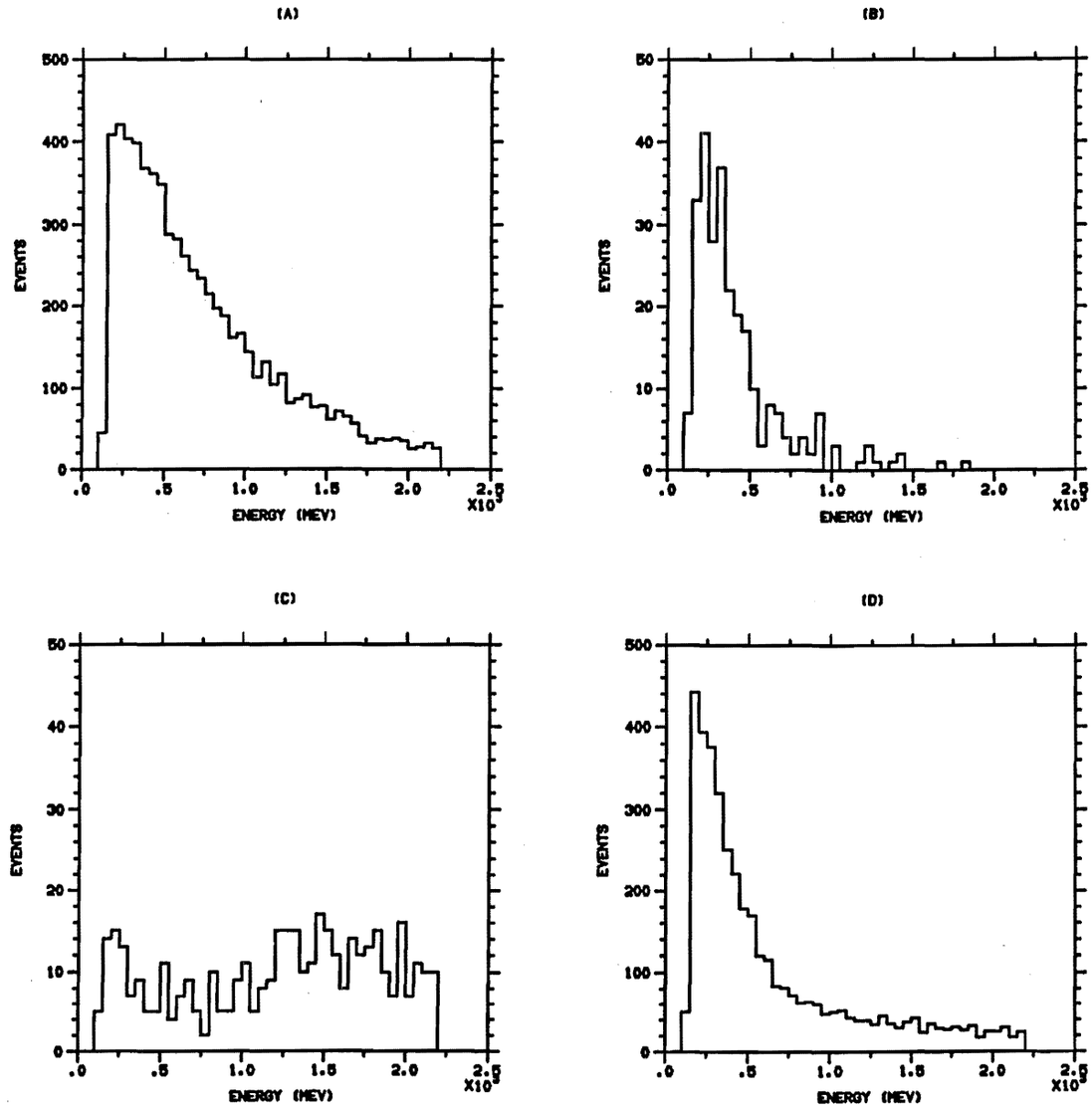

Figure 4.2.3 Shower energy distribution for a) $\nu_\mu e \rightarrow \nu_\mu e$ Monte Carlo, b) $\nu_\mu n \rightarrow \nu_\mu n \pi^0$ Monte Carlo, c) $\nu_e n \rightarrow e^- p$ Monte Carlo, and d) the data.

The fiducial volume cut was

$$6 < X_{PDT} < 51$$

$$6 < Y_{PDT} < 51$$

$$6 < Z_{Module} < 98$$

where X_{PDT} and Y_{PDT} are the PDT wire positions and Z_{Module} is the module number of the vertex cell. The distribution of event vertex positions is shown in Fig. 4.2.2. The fiducial volume cut is used to eliminate front or side entering tracks or electron events which are not fully contained in the detector. The cut on the corrected electron energy was

$$210MeV < E_e < 2100MeV.$$

The low energy cut is used to reduce background hadrons and π^0s which dominate at low energies. The high energy cut is used to reduce $\nu_e n \rightarrow e^- p$ background which dominates in the region above 1500 MeV. The electron energy distribution is shown in Fig. 4.2.3.

The next step in the data reduction procedure was to apply an energy cut to the vertex calorimeter cell. Any event with greater than 30 MeV in the vertex cell was rejected. This cut was intended to reduce the hadronic background component in the sample. It primarily addressed the $\nu_e n \rightarrow e^- p$ background owing to the high energy deposition of the final state proton. The 30 MeV level was determined to be the upper limit on the expected true electron signal vertex energy distribution (see Fig. 4.2.4).

Application of these cuts reduce the $8,778$ events from the second eyescan to $3,042$ events. This reduced sample was then subjected to an interactive refit of the initial shower angles by physicists.

The strongest signature for identifying $\nu_\mu e \rightarrow \nu_\mu e$ scattering in this experiment is the very forward initial electron scattering angle (< 0.1 rad). A precise determination of this angle will provide the best means of extraction of signal from

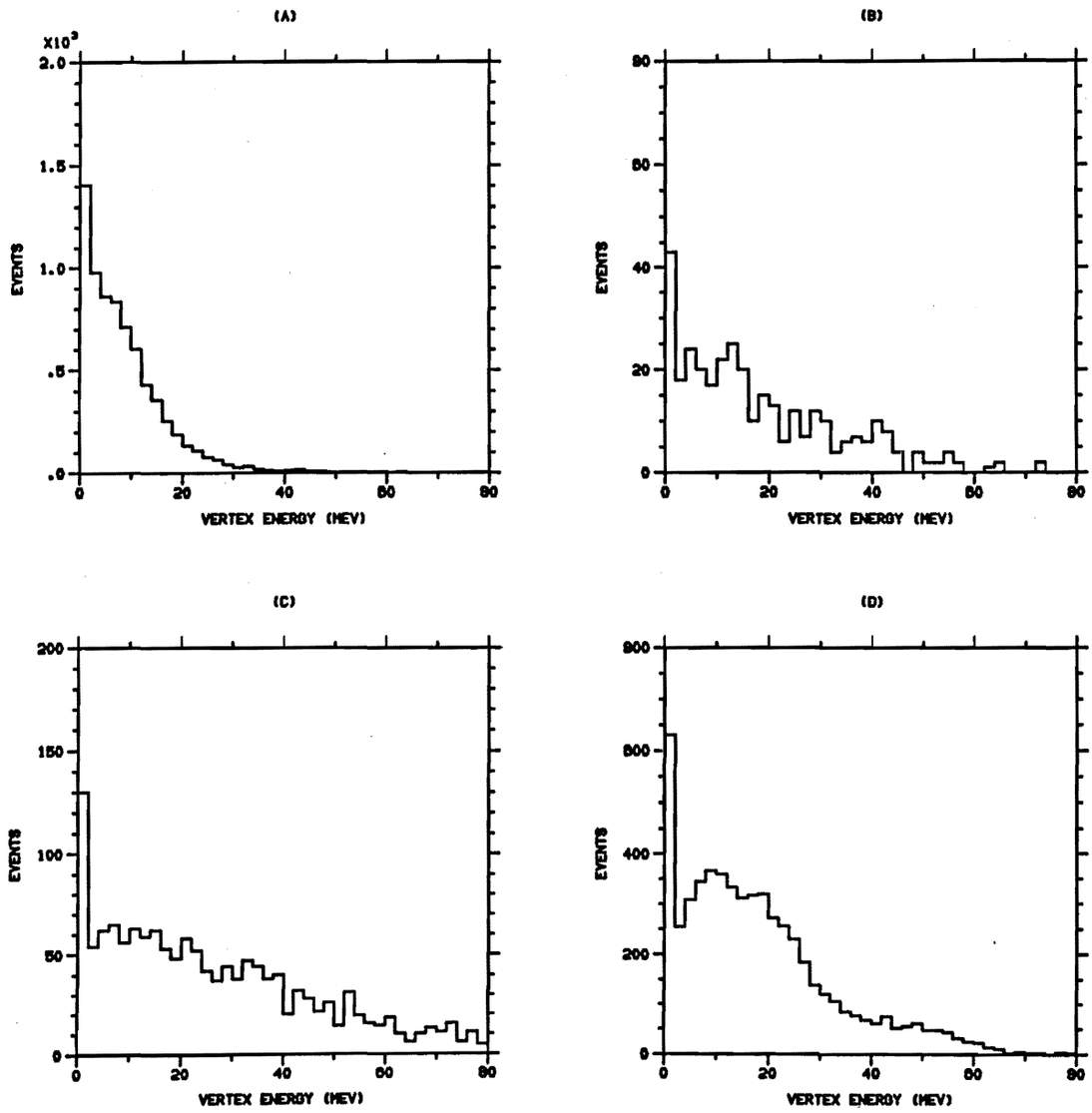

Figure 4.2.4 Vertex energy for a) $\nu_\mu e \rightarrow \nu_\mu e$ Monte Carlo, b) $\nu_\mu n \rightarrow \nu_\mu n \pi^0$ Monte Carlo, c) $\nu_e n \rightarrow e^- p$ Monte Carlo, and d) the data.

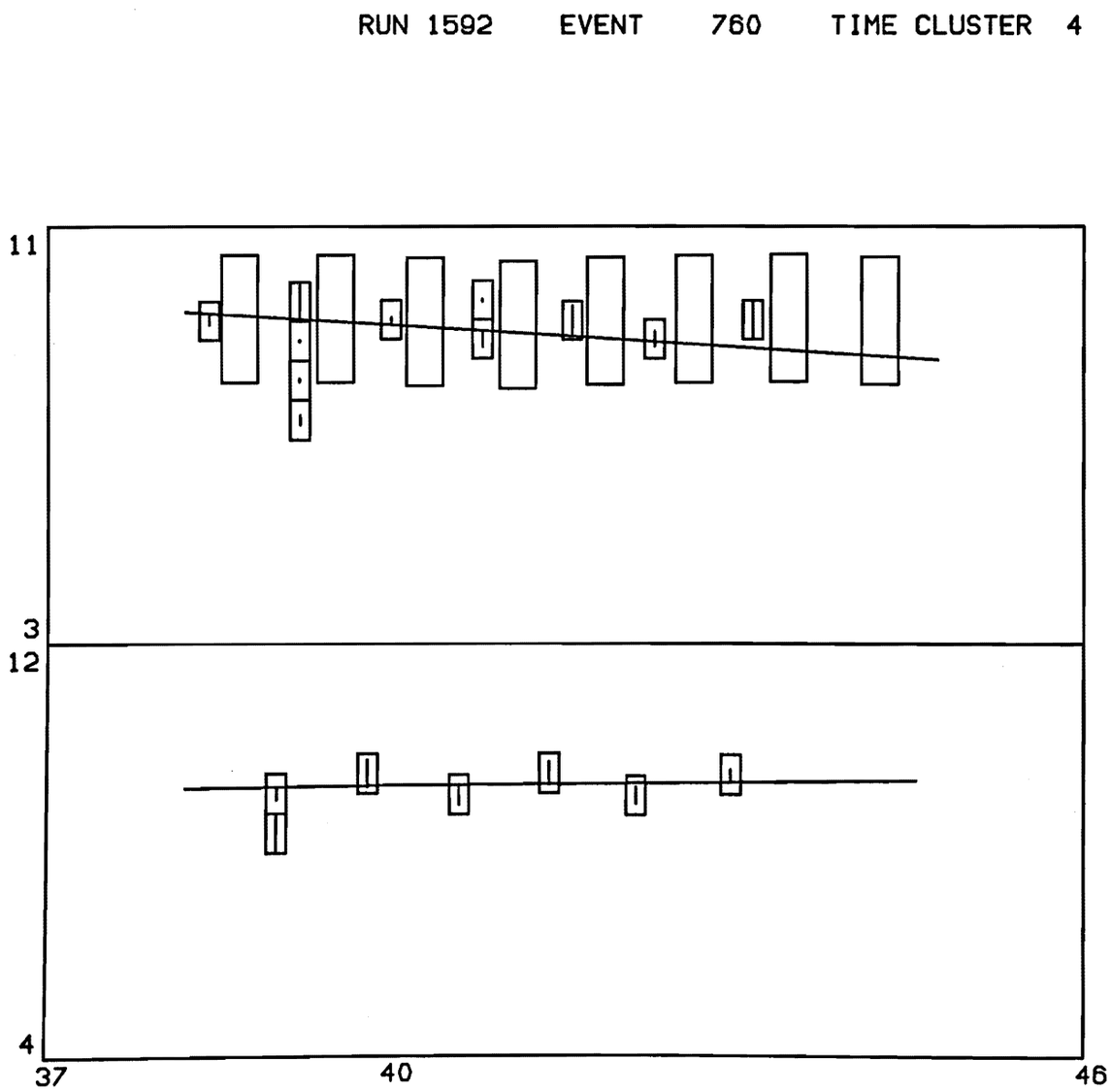

Figure 4.2.5 Interactive display for shower angle determination

background. This determination is accomplished by an interactive scan and refit of all shower angles. Each projection of each selected event is displayed on a Tektronics graphics screen with the "best fit" angle displayed. An example is shown in Fig. 4.2.5. The operator can then decide whether the trial fit is appropriate (e.g. exclusion of crossing muon hits). If not, the operator can then choose from the display screen the best fit which will satisfy the shower criteria (drift contours, multiple scattering). The operator can make multiple attempts by trial and error until satisfied with the choice of fit in that projection. A summary file is then made of all refit angles.

After examination of each projection of each event in the data sample, only 24% of the angles in the X projection and 28% of the angles in the Y projection had to be refit. Each event which had either one or both projections refit was checked for angular biasing on the part of the operator. Comparisons of the original and refit angles were performed. No systematic correlation between the refit angle and the original angle was found.

After the interactive angle refit, the selected events (with updated angles) were processed through another interactive program which applied a "maximum" multiple scattering road to each projection of the shower candidate. The largest source of background in this experiment is from photons produced in π^0 decays and hadronic interactions. However, the showers from π^0 decays and hadronic interactions have a broad scattering distribution owing to 1) the fact that both daughter photons from π^0 decay may be visible in the detector as separated angles and 2) that hadronic interactions are not kinematically constrained to the forward direction necessarily. By applying a multiple scattering road based on the maximum scattering limits of a single electron, much of the background can be eliminated.

Again each projection of each candidate shower is displayed on a Tektronics graphics screen with the multiple scattering road shown. A line 20 modules in length is draw upstream from the shower vertex. The sum of the shower energy outside the road is displayed along with any energy "seen" directly upstream of

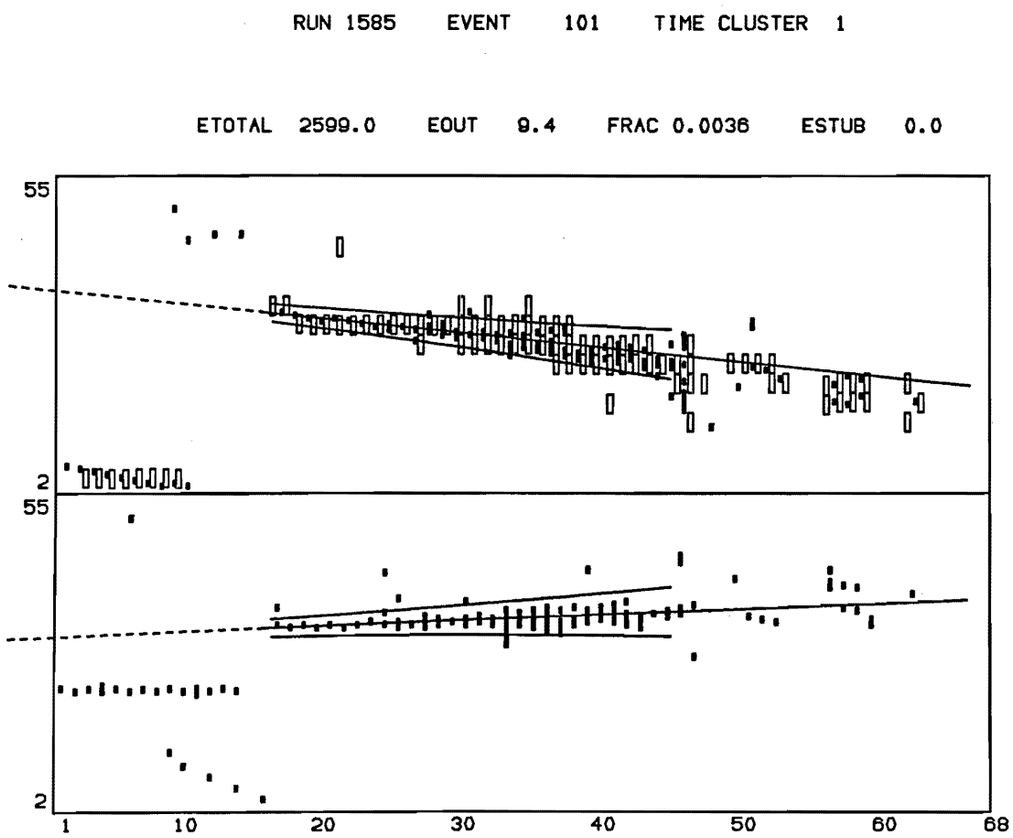

Figure 4.2.6 Graphic event display of the "road" application

the vertex. An example is shown if Fig. 4.2.6. The operator accepts or rejects the event based on two determinations. 1) If the energy outside the road is greater than 2.5% of the total shower energy, the event is rejected. 2) If there is greater than 10 MeV of energy "seen" directly upstream of the vertex, the event is rejected. The operator may exempt an event from these criteria if the energy determinations were complicated by the presence of an unassociated track or event (e.g. beam muon, side entering track, etc.).

The 1,545 events which passed the "road" cut were then checked for fatal microprocessor errors, duplicate events, and bad runs. Any events failing these checks were removed from the candidate list. These same checks were applied to the normalization sample to insure consistency and the validity of the information used in each event. Only 20 events were removed from the sample.

At this point, the background in this condensed data sample now consists mostly of photons from π^0 decays with only a small, low energy ($< 400MeV$) hadronic component. To separate out signal from background is now mostly a matter of separating electron events (showers) from photon events (showers). This was accomplished by investigating the dE/dx distributions in the early part of each shower candidate.

To separate the electrons from the background, that is to separate the events into an "electron" sample and a "gamma" sample, PDT and scintillator dE/dx measurements near the shower vertex were used. The separation was based on Monte Carlo and test beam studies of single electron and e^+e^- pair ionization rates for this detector. True electrons appear with high probability ($>$ 90%) as single ionizing particles while the photons of the background appear ($>$ 70% of the time) as double ionizing particles. The energy deposition in the first calorimeter cell after the vertex was used for the decision on the calorimeter ionization (see Fig. 4.2.7). The PDT information used was more complicated for two reasons. First because the PDTs are low mass devices, there is a probability that a PDT registers zero energy some fraction of the time. Second because the PDT dE/dx distributions have large Landau tails at high dE/dx values. To reduce these effects,

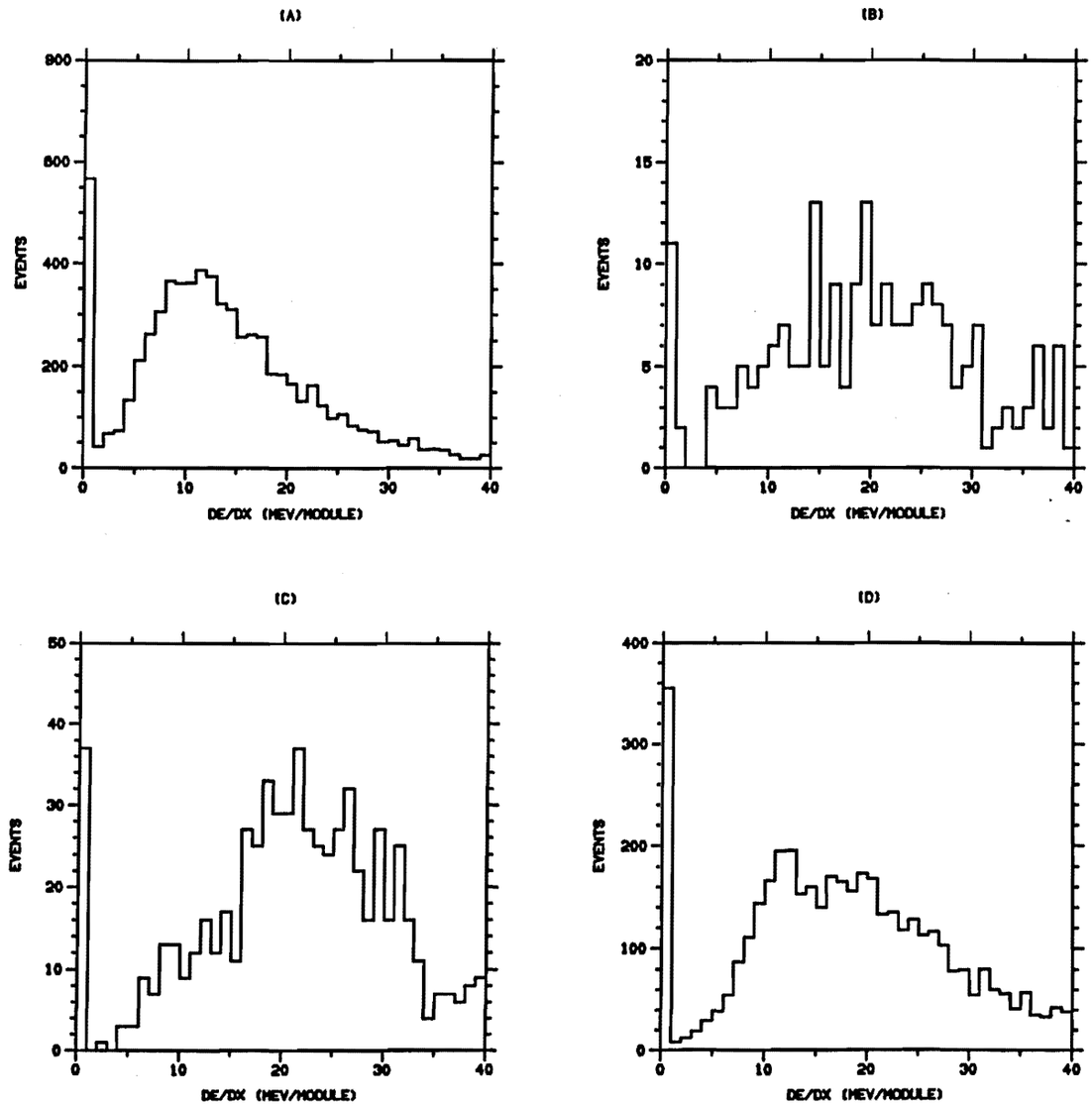

Figure 4.2.7 dE/dx depositions in the first calormeter after the vertex for a) $\nu_\mu e \rightarrow \nu_\mu e$ Monte Carlo, b) $\nu_\mu n \rightarrow \nu_\mu n \pi^0$ Monte Carlo, c) the stub sample and d) the data.

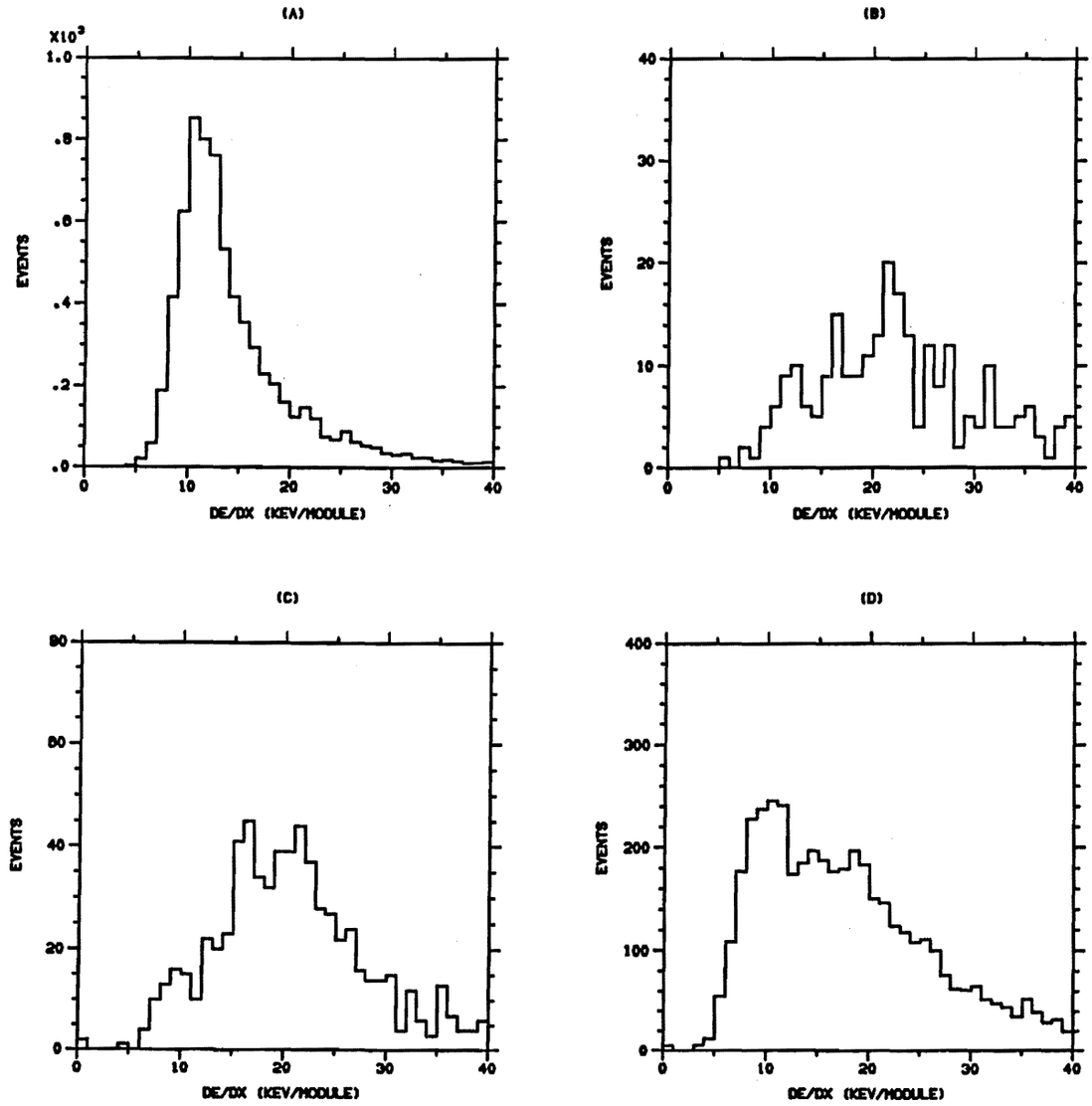

Figure 4.2.8 The average dE/dx depositions in the PDTs downstream of the vertex for a) $\nu_\mu e \rightarrow \nu_\mu e$ Monte Carlo, b) $\nu_\mu n \rightarrow \nu_\mu n \pi^0$ Monte Carlo, c) the stub sample and d) the data.

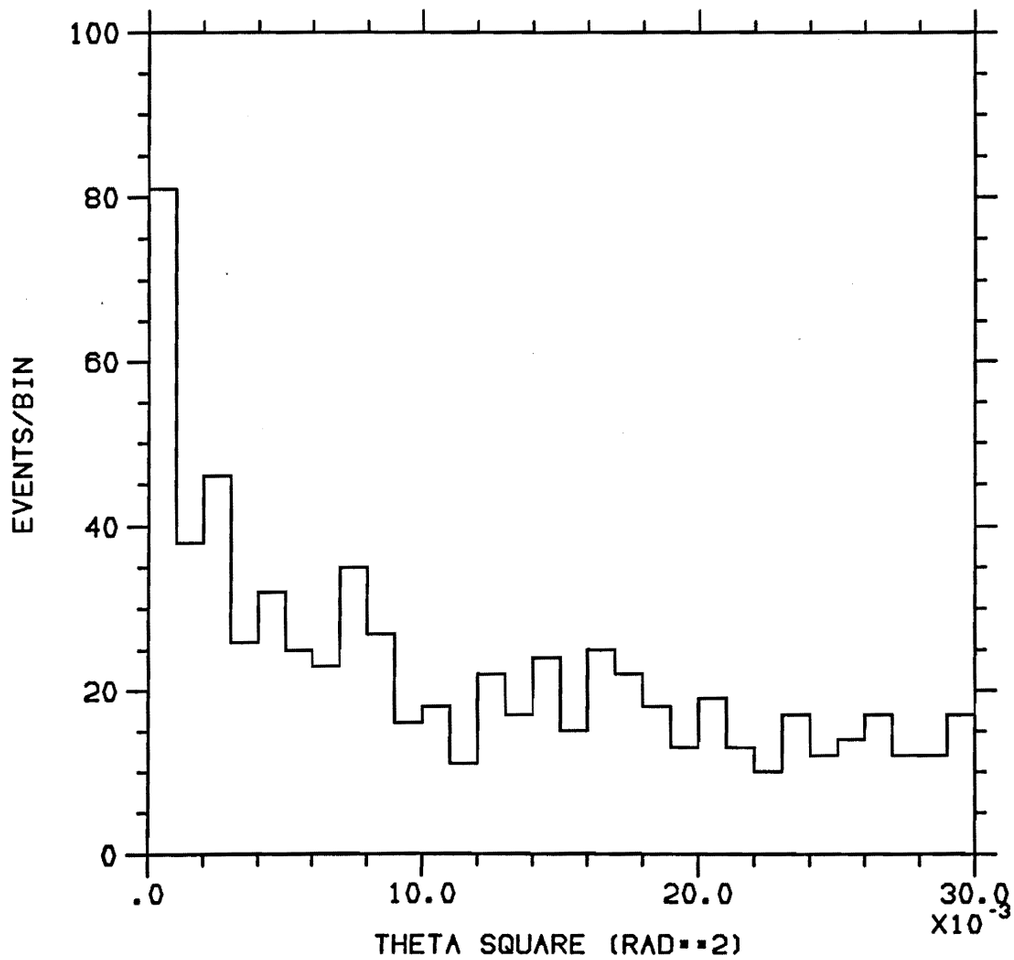

Figure 4.2.9 θ^2 for the final electron sample

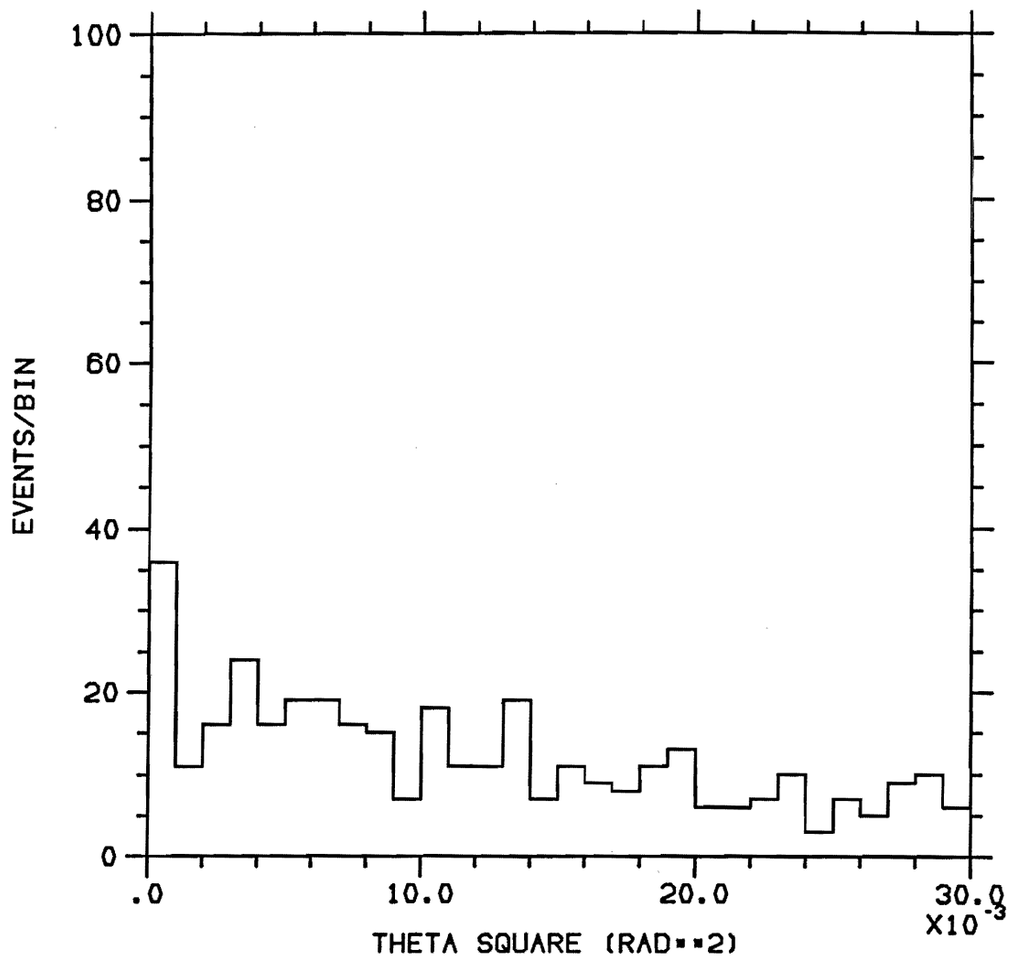

Figure 4.2.10 θ^2 for the final photon sample

the PDT ionization was calculated from the average of the minima of each x and y PDT plane before and after the first calorimeter cell used above (see Fig. 4.2.8). PDT planes with zero energy were excluded from taking the minima and average. If an event had no PDT energy information in these planes, the event was passed as an electron. The "gamma" sample was designated as the region for which

$$dE/dx[CAL] > 18MeV$$

and

$$dE/dx[PDT] = \frac{\min(E_{x_1}, E_{y_1}) + \min(E_{x_2}, E_{y_2})}{2} > 15KeV.$$

These separation values correspond to the points between minimum and twice minimum ionizing peaks for the ionization studies performed above. Any event not classified as a "gamma" by this scheme was considered an "electron" event.

The e/γ separation procedure identified 977 "electron" events and 548 "gamma" events. These two samples were reduced to 716 "electron" events and 355 "gamma" events by a maximum θ^2 limit of 0.03. Studies established that fewer than 1% of the electron signal extended beyond 0.03. Plots of θ^2 for the "electron" and "gamma" sample are shown in Fig. 4.2.9 and Fig. 4.2.10, respectively.

3. Signal Extraction

Once the data had been condensed down into "electron" and "gamma" samples, final signal extraction could take place. At this point the two most significant quantities to investigate for signal extraction were the electron angle in θ^2 and the electron energy, E_e. Both the angle and energy for signal electrons and background have been studied extensively with Monte Carlo. A clear understanding of the form of these distributions with consideration for resolution and acceptance is known and will be used to extract the final signal.

In the analysis of previous data sets[27,25] it was determined that the background present in the "electron" and "gamma" samples was nearly flat in θ^2. This resulted from the omni-directional decay of the parent π^0s for the background

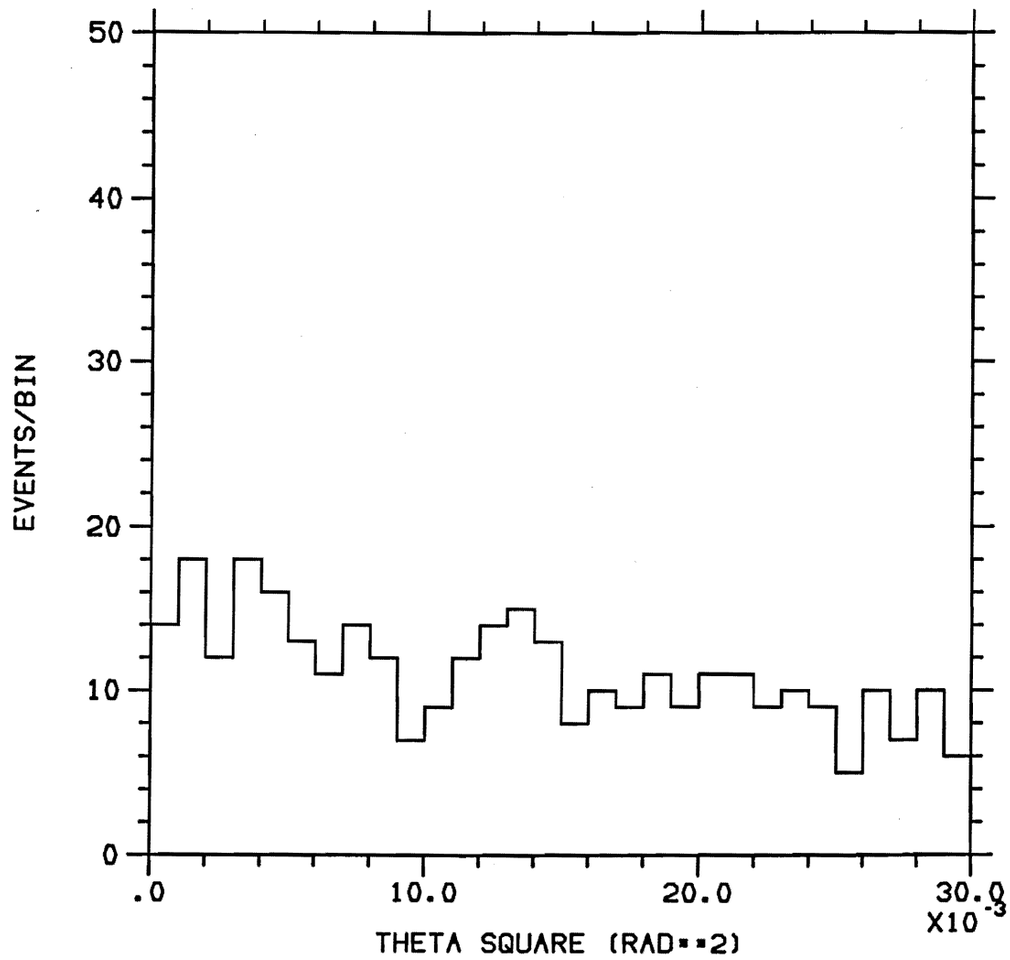

Figure 4.3.1 θ^2 distribution for the "stub" sample

photons and the uniform acceptance in θ^2. However it was discovered with this data set and analysis that the background shape was not flat but sloped in θ^2. This was apparent in both the "electron" and "gamma" samples (see Fig. 4.2.9 and Fig. 4.2.10) as well as the "stub" sample (see Fig. 4.3.1). The source of the slope was traced to the PDT filter angle cut at 200 mrad performed before the eye-scan. This was not fully apparent in the previous analyses because of insufficient statistics. All other cuts in the analysis were checked and no apparent angular biased was discoverd.

The slope effect was found to arise from the difference between the PDT filter angle and the DST/refit angle (previously described). Since the errors associated with each angle determination are independent of each other and since the PDT filter resolution error is significantly larger than the DST/refit for background events, the change in angle from the PDT filter angle to the DST/refit angle is equally likely to be significant positive or negative shift. However, the 200 mrad cut on the PDT filter angle produces a boundary effect were the distribution of events in θ^2 has a net increase to higher angle since the increase cannot be balanced by events which had been decreased from higher angles. In effect, the events can "wash" over the boundary to higher angles but not back the other way. The probability that an event will move over to higher angle and not be compensated by an event moving back the other way is proportional to the value of the angle. This is the effect which produces the observed slope in θ^2 when examining the DST/refit angle. This effect has been observed with Monte Carlo with appropriate models for the PDT filter resolution and the DST/refit angular resolution (see Fig. 4.3.2).

High statistics Monte Carlos for coherent and incoherent π^0 production [30]($\nu_\mu N \rightarrow \nu_\mu N \pi^0$) and for $\nu_e n \rightarrow e^- p$ production were generated. These channels were believed to predominately compose the background. The generated shower angle for these events was then smeared according to the PDT filter angular resolution. The plot of the PDT filter angle was observed to be flat in θ^2. The 200 mrad cut was then applied. The generated angle of the surviving events was

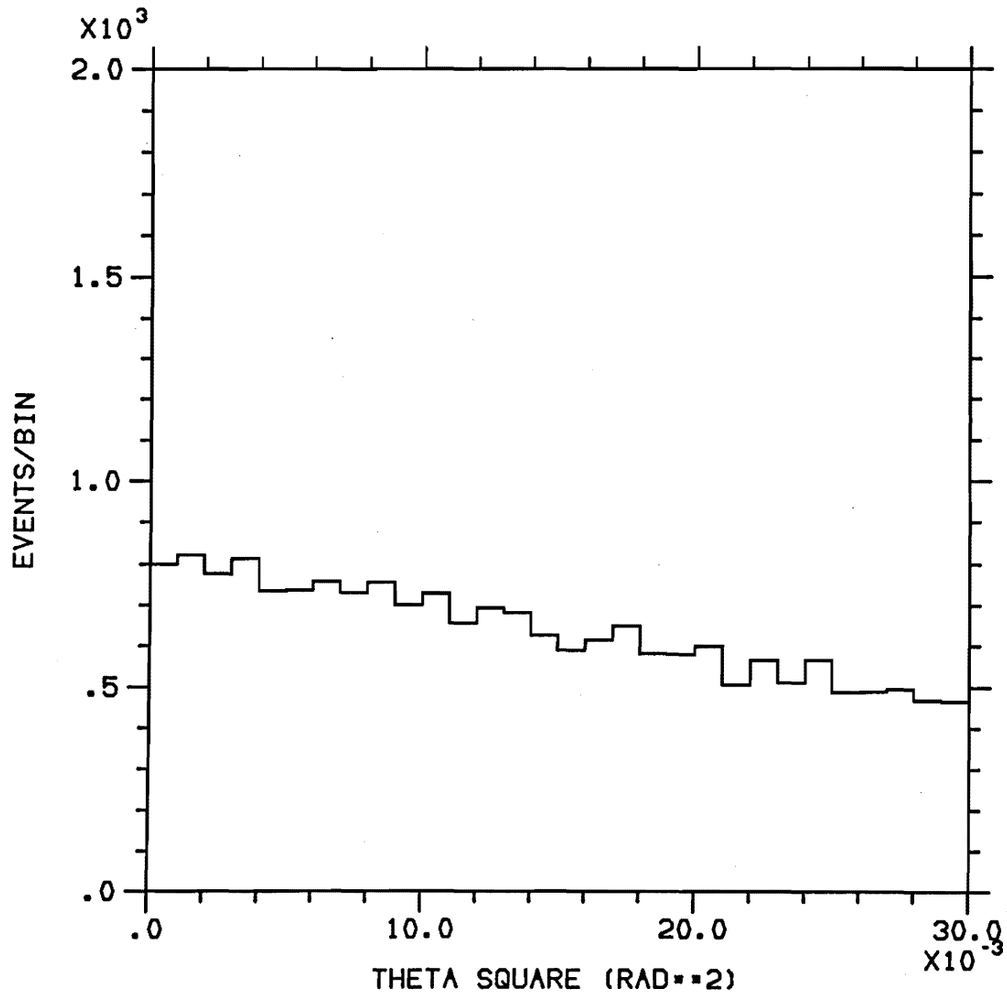

Figure 4.3.2 Monte Carlo π^0 events exhibiting the "slope" phenomenon

then smeared according to the DST/refit angular resolution. The θ^2 plot of the DST/refit angle revealed the slope phenomenon. Several different resolution models for the PDT filter angle and the DST/refit angle were tried and had the same result. All three background channels gave the same conclusion. Since the e^-p channel was not considered to have significant statistical influence on the background shape (44 out of 716 events) and no signicant difference between coherent and incoherent π^0 events was observed in this study, it was established that the the incoherent π^0 channel with the correct models for the resolution would accurately represent the background for later signal extraction studies.

Studies were done to interrogate the nature and composition of the candidate electron energy dustribution. The largest concern was the possible presence of a small, low energy ($< 400MeV$) hadronic component. Plots of θ^2 for various energy regions were studied. No significant correlation of background in θ^2 to energy could be identified. Additional studies investigating ionization rates in the forward part of the shower were unable to establish any statistically significant correlation between hadronic background and θ^2.

In order to identify possible hadronic events, an algorithm was used to determine the average number of PDT hits per plane over the extent of a shower candidate. A Monte Carlo study based on various channels showed that hadronic events in this data sample would be populated in the region with the average number of PDT hits per plane less than 1.3 (since hadrons do not brem). By selecting events from the data sample based on this criterion, an enriched sample of hadronic events was obtained. Plots of θ^2 for these events exhibited the same angular shape as was observed in the previous background studies in θ^2 for π^0s (see Fig. 4.3.3). That is, there were no discernible difference in θ^2 between hadron enriched and non-enriched background samples. Thus it was establish that contributions from the hadronic background would not complicate background subtraction based on θ^2.

The final number of observed electron events from the data sample of 716 "electron" candidates, was determined from a maximum likelihood fit involving

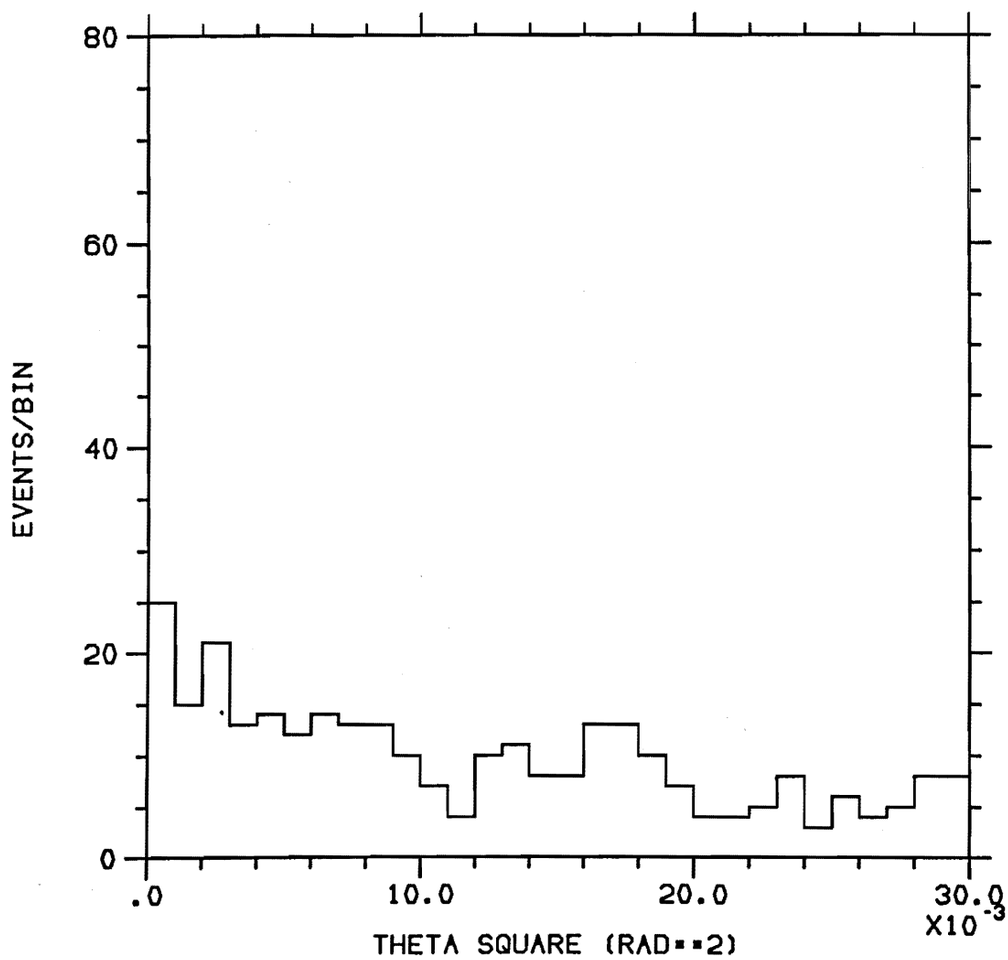

Figure 4.3.3 θ^2 plot for the hadron enriched sample

electron energy and θ^2 distributions. Signal and background distributions were fit to the data using a log-likelihood function. The signal event distributions were generated from the full Monte Carlo with resolution, acceptance and inefficiency effects added in as well as the noise from raw event overlays. The raw event overlays were AGS beam bursts selected at random from the full data set (before any data reduction). These events enhance the Monte Carlo modeling of events by adding detector noise and element inefficiencies. The background events were produced at the Monte Carlo generator level to obtain sufficiently high event statistics. The events were incoherent π^0 events exclusively which was determined to be an appropriate representation of the background at this point in the analysis. The modeling of the acceptances and angular resolution effects were applied to the background after generation. The PDT Filter angular resoultion effect was added to the background to produced the expected slope in θ^2. The energy distribution for the background was modeled from the energy distribution of the data for $\theta^2 > 0.01 rad^2$. Since no signal was observed to be present above 0.01 in θ^2, it was determined that this selected energy distribution would be an adequate model of the energy for the background Monte Carlo.

The form of the log-likelihood function was derived from the product of the probability functions for each bin (or element) in the $E - \theta^2$ distribution. The probability distribution for each bin was considered to be Poisson in nature

$$P_{\bar{n}}(n) = \frac{e^{-\bar{n}}\bar{n}^n}{n!}$$

owing to the finite number of events in each element. The likelihood function is expressed as the product of the probabilities for each element

$$\Phi = \prod_{ij} P_{\bar{n}_{ij}}(n_{ij}).$$

Therefore by subsituting in the form of the Poisson distribution, the log-likelihood function can be expressed as

$$\ln \Phi = \sum_{ij}(-\bar{n}_{ij} + n_{ij} \ln \bar{n}_{ij} - \ln n_{ij}!)$$

where n_{ij} is the number of events found in element ij for the data sample and

$$\bar{n}_{ij} = N_S f_{ij}^S + N_B f_{ij}^B$$

is the mean number of events in each element predicted by the Monte Carlo distributions weighted according to the respective number of signal, N_S and background, N_B events.

The maximum likelihood fits were performed using the FORTRAN minimzation package, MINUIT [31]. MINUIT was used to minimize the negative of the log-likelihood function to find the respective number of signal,N_S and background, N_B events. The minimization of the negative of the log likelihood corresponded to finding the maximum of the likelihood function or in other words the best combination of signal and background events.

Bins ($\theta^2 \times E$)	N_S
30×1	113.5 ± 16.0
30×2	111.9 ± 15.7
30×3	108.9 ± 15.6
30×4	108.0 ± 15.4
30×5	105.1 ± 15.2
30×6	105.1 ± 15.2
30×10	103.3 ± 14.9
30×12	106.7 ± 15.0
30×15	106.5 ± 14.8
30×20	105.5 ± 14.8
30×30	105.5 ± 14.6
30×60	106.2 ± 14.4
1×15	112.0 ± 42.7
1×30	115.6 ± 39.2
1×60	148.9 ± 32.6

Table 4.3.1 $E - \theta^2$ fits for various binnings

Many combinations of distribution binning in both energy and θ^2 were tried, as well as fits exclusive in energy or θ^2. Several different binnings in both θ^2 and energy were done to study the systematics associated with this fitting technique. The fits were stable for different binning in θ^2. However there were systematic

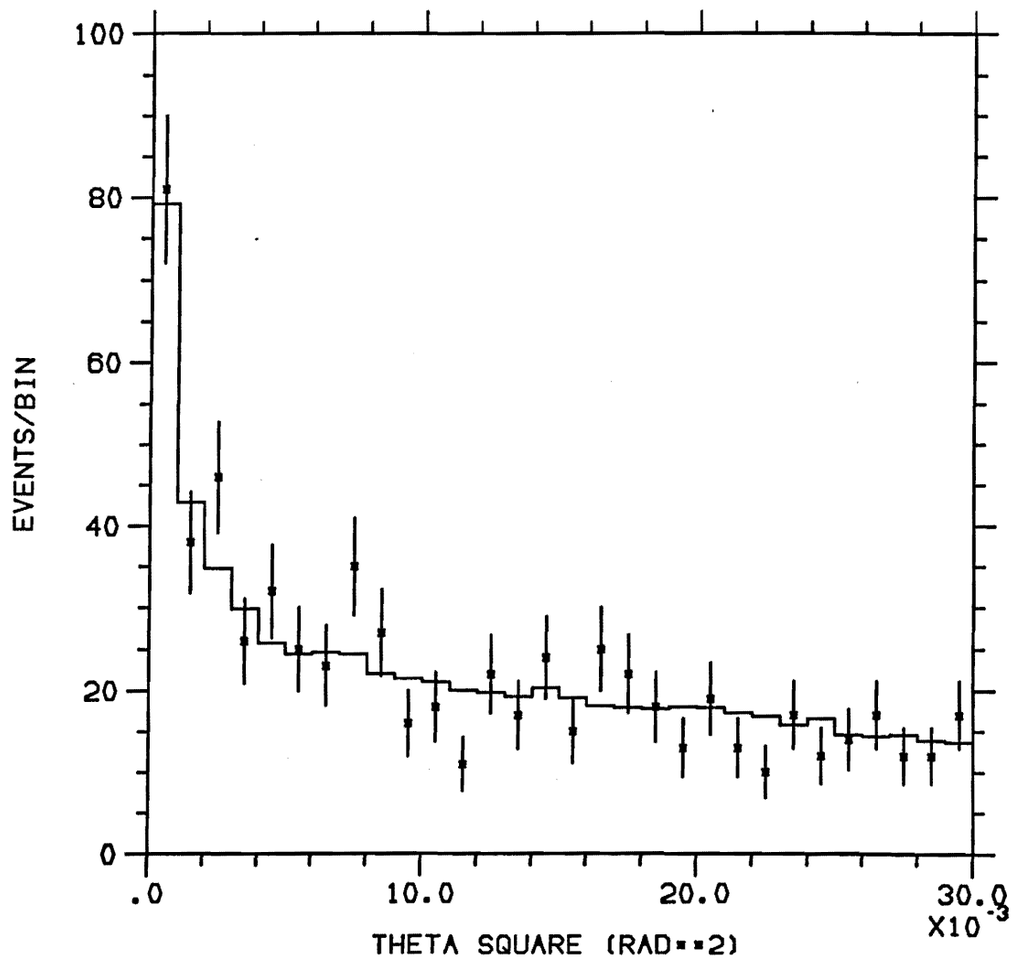

Figure 4.3.4 θ^2 fit to the data (error bars) with Monte Carlo (solid line) signal and background

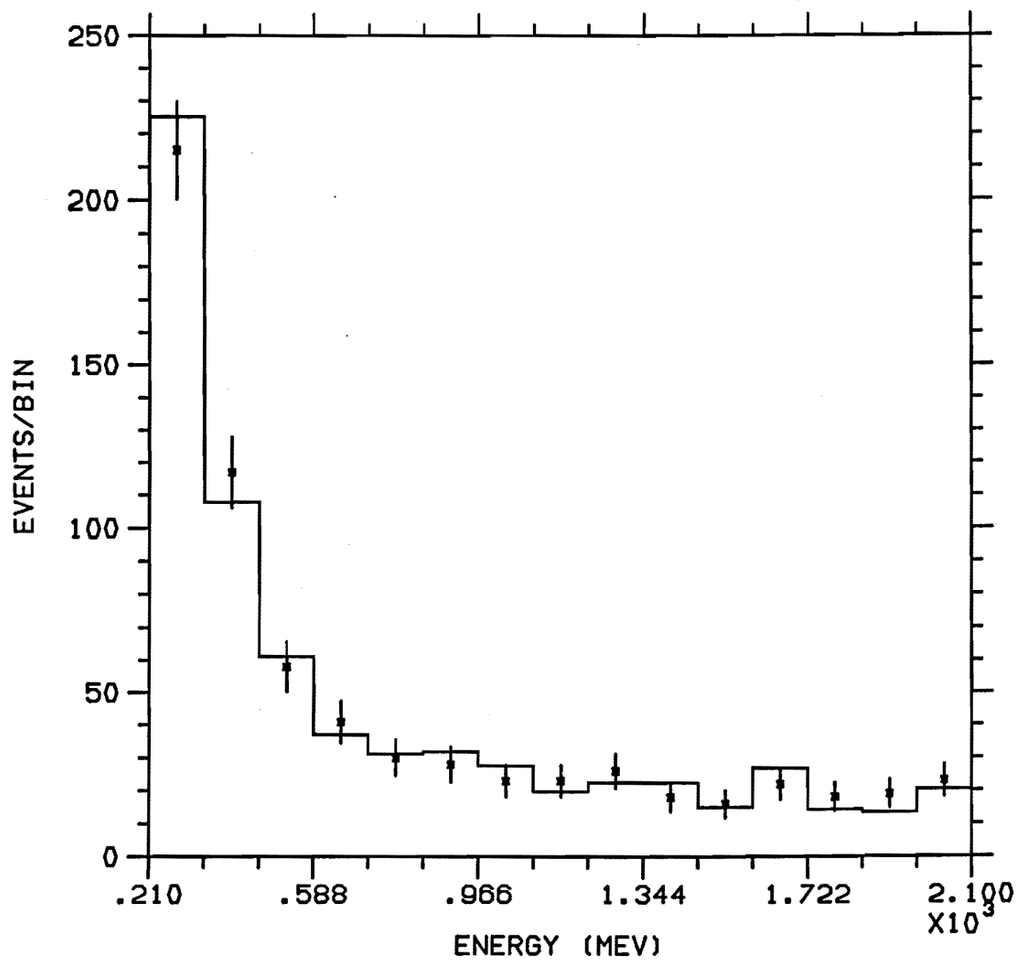

Figure 4.3.5 Energy fit to the data (error bars) with Monte Carlo (solid line) signal and background

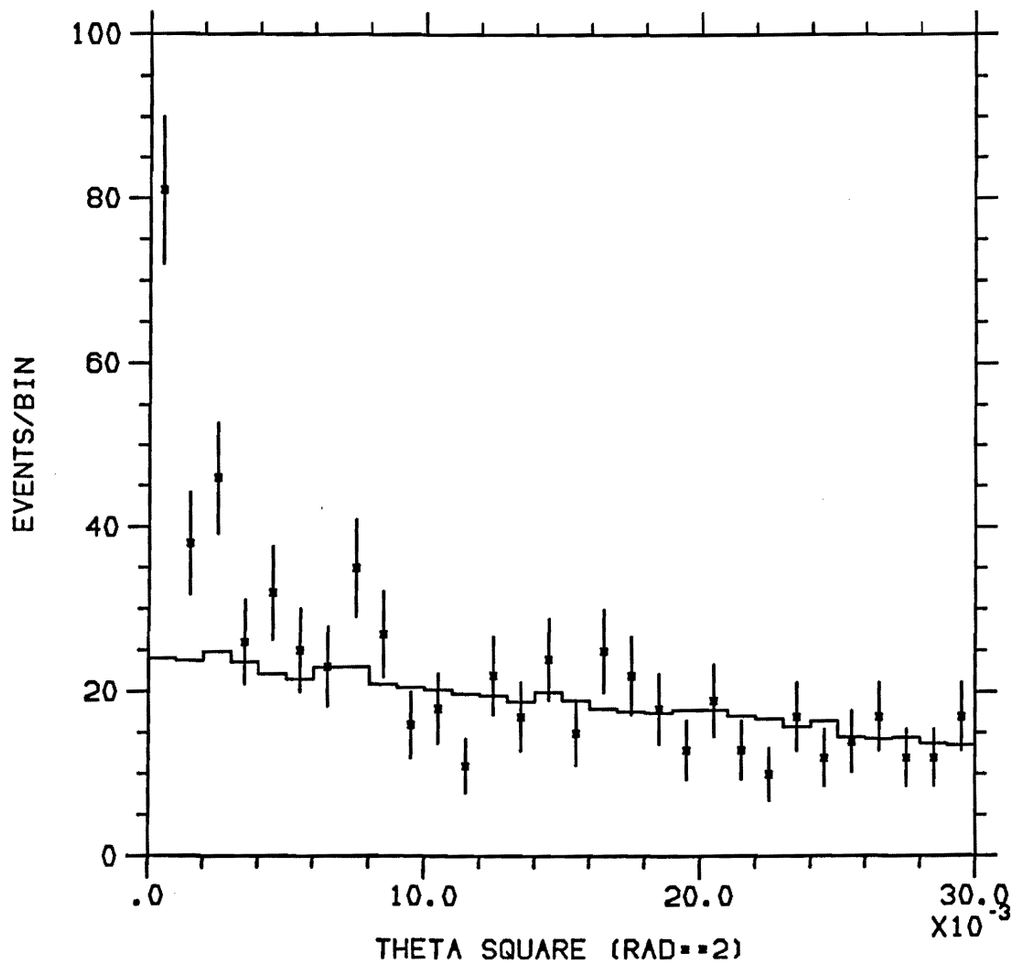

Figure 4.3.6 θ^2 fit to the data (error bars) with Monte Carlo background (solid line) only

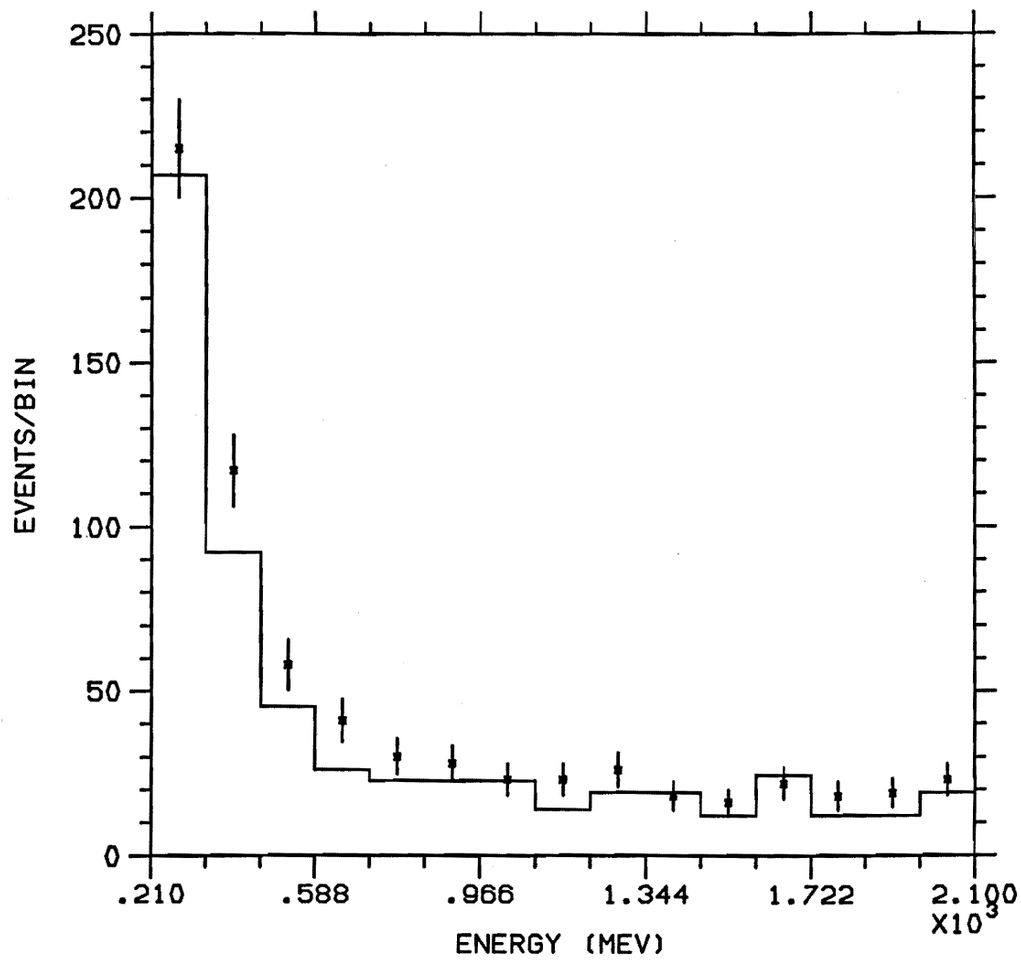

Figure 4.3.7 Energy fit to the data (error bars) with Monte Carlo background (solid line) only

fluctuations for different binnings in energy (see Table 4.3.1). 30 bins in θ^2 and 15 bins in energy were chosen for the final value for the observed number of electron events

$$N_S = 106.5 \pm 14.8[stat] \pm 5.0[syst].$$

This particular fit was chosen as the most appropriate because of its central value relative to the other binnings and relative size of the statistical error. Plots of θ^2 and energy for the final fit are shown in Fig. 4.3.4 and Fig. 4.3.5, repectively. Plots of θ^2 and energy indicating the level of background in the final fit are shown in Fig. 4.3.6 and Fig. 4.3.7, respectively. The statistical error determined by MINUIT corresponded to a change in the log likelihood function of 0.5. This represents the 68% confidence level limit.

4. Acceptances and Efficiencies

In order to obtain an accurate determination for the $\nu_\mu e \rightarrow \nu_\mu e$ cross section, the number of observed electron events had to be corrected for losses and inefficiencies in the analysis process as well as for any residual background.

The first loss or inefficiency in the analysis was due to the PDT filter. The function of the PDT filter was to locate all possible shower candidates which might be considered electron events. However, a small fraction of the time the PDT filter would fail to locate a genuine electron event. To measure this inefficiency, Monte Carlo generated electron events were used. These events were generated with the full Monte Carlo which incorporated models for PDT and calorimeter inefficiencies and weighted according to the actual beam flux. These models would enable the Monte Carlo to emulate the real data in regard to the effect of element inefficiencies on the PDT filter performance. In addition, randomly selected data events from three separate running periods were overlaid on the Monte Carlo events. This would add in the effect of detector noise on PDT filter performance. The efficiency is then simply the percentage of Monte Carlo electron events the PDT filter located within the fiducial volume. This was done for each of the three different overlay sets. The three results were combined to provide an overall value

to use for the entire data set with the difference between the individual values used as a measure of the systematic uncertainty in the effect of detector noise on the filter performance. The PDT filter efficiency was measured to be

$$\epsilon_{PDT} = 0.882 \pm 0.005[stat] \pm 0.012[syst].$$

The statisical error was determined simply from the number of generated events used in the study.

The next loss in the analysis was due to the 200 mrad cut on the PDT filter angle to reduce the eyescan sample. Normally electron events would have PDT filter angles well below this cut. However, a small fraction of the electron events would be lost due to the PDT filter miscalculation of the angle. To measure this inefficiency, the same Monte Carlo events used in the previous study were used. The efficiency is then simply the percentage of Monte Carlo events within the fiducial volume which survive this cut. Again this was done for all three overlay sets and the results combined to be used against the entire data set. The PDT filter angle cut efficiency was measured to be

$$\epsilon_{\theta<0.2} = 0.978 \pm 0.003[stat] \pm 0.003[syst]$$

.

Next in the analysis were losses from the eye scans. A new set of Monte Carlo electron events were generated and randomly inserted into the eye scan samples at the 2% level. The Monte Carlo events were generated in the same fashion as the events used in the previous studies except only two sets of overlay events were used. Each event was double scanned by two different and independent scanners. Since multiple scanners participated in the eye scan, individual efficiencies were tabulated. The overall eye scan efficiency used for the final correction was then simply the percentage of Monte Carlo events within the fiducial volume that were selected by either scanner.

The eyescan was performed in two steps. The first step involved individual scanners working independently in which each event was scanned twice by two

different scanners. The overall eyescan efficiency for this scan was determined to be

$$\epsilon_{eye1} = 0.990 \pm 0.002[stat].$$

The second step involved a rescan of all selected events from the first step. This scan required scanners to work in pairs where event selection is made in conjuction by the paired scanners. Each event from the first step was doubled scanned by pairs from different institutions (i.e. Brown U. and U. of Pennsylvania). Differences between the institutions were adjudicated in a joint session. The overall eyescan efficiency for this scan was determined to be

$$\epsilon_{eye2} = 0.987 \pm 0.002[stat].$$

The next step in the analysis was the $210MeV < E_e < 2100MeV$ energy cut on the electron energy. Again the inefficiency effects from this cut were evaluated with Monte Carlo events. A generator level study (as opposed to the full Monte Carlo) was used in order to obtain significantly high statistics. The acceptance factor is simply the percentage of events which passed this cut. However, the acceptance factor depends weakly on the value of the Weinberg angle. When the final fit for $\sin^2\theta_W$ is performed the functional dependence for the acceptance factor is included. The acceptance factor for the Weinberg angle of $\sin^2\theta_W = 0.225$ was measured to be

$$A_{210\rightarrow 2100} = 0.710 \pm 0.001[stat] \pm 0.030[syst].$$

The vertex energy cut of 30 MeV in the analysis was the next effect to be examined. Once again the full Monte Carlo was used to determine the efficiency as simply the percentage of events which survive the cut. The vertex energy cut efficiency was measured to be

$$\epsilon_{Evtx<30} = 0.978 \pm 0.002[stat] \pm 0.007[syst].$$

After the vertex energy cut the next step was to apply the electron/gamma separation technique. The efficiency of this technique has been studied carefully

with Monte Carlo and test beam electron events. The efficiency is simply defined as the percentage of events selected as electrons by this technique. Since this technique is very dependent on observed energies in individual elements, it was judged that the test beam events would be a more representative emulation of genuine electron events than the Monte Carlo events. However the Monte Carlo did serve to support the test beam determination of the efficiency. The electron/gamma efficiency was measured with test beam events to be

$$\epsilon_{e/\gamma} = 0.91 \pm 0.01[stat] \pm 0.02[syst].$$

The next step in the analysis was to apply a multiple scattering road to the candidate events to further eliminate background events. However some fraction of the electron events would be lost. To determine the loss, Monte Carlo electron events were passed throught this multiple scattering road. The percentage of surviving events determined the efficiency to be

$$\epsilon_{Road} = 0.924 \pm 0.010[stat] \pm 0.011[syst].$$

The final efficiency correction that had to be determined was the 0.03 Rad^2 cut on the sample. Owing to angular resolution effects in determining the final electron angle, a small percentage of electron events will have a resultant angle greater than 0.03 Rad^2 in θ^2. Monte Carlo events at the generator level with the appropriate energy and angular resolution models were used to calculate the efficiency. The efficiency was measured to be

$$\epsilon_{\theta^2<0.03} = 0.994 \pm 0.001[stat] \pm 0.031[syst].$$

The next correction which had to be made was for the fraction of electron events produced by wrong helicity neutrinos in the neutrino beam. To determine this fraction, the cross section for anti-neutrino electron scattering[25] was integrated over the beam flux for wrong helicity neutrinos

$$N_{wh} = \int \phi_{wh}(E_\nu)\sigma_{wh}(E_\nu)dE_\nu n_e$$

where $\phi(E_\nu)$ is the wrong helicity flux (see Fig. 2.1.8), $\sigma_{wh}(E_\nu)$ is the anti-neutrino cross section, and n_e is the number of target electrons in the fiducial volume of the detector. The resulting number of wrong helicity events was then divided by the best estimate of the expected number of actual neutrino electron events to determine the fraction of wrong helicity events. This fraction was calculated to be

$$f_{wh} = 0.016 \pm 0.004[syst].$$

Here the systematic error is dominated by the uncertainty in the wrong helicity flux.

The last correction to be made was also due to beam contamination. A small beam component of electron neutrinos will induce electron neutrino quasi-elastic events which would be able to emulate neutrino electron elastic events in the analysis. To determine the fraction of these quasi-elastics in the final sample, Monte Carlo electron neutrino quasi-elastic events were generated and passed through the analysis to determine the overall acceptance. Next the cross section[30] for this process was integrated over the electron neutrino component in the beam (see Fig. 2.1.9). This number was then corrected by the acceptance to determine the number of electron neutrino quasi-elastic events in the final sample. This number was calculated to be

$$n_{e-p} = 3.8 \pm 0.3[stat] \pm 2.0[syst].$$

Once the corrections to the observed number of electron events have been established, the true number of electron events can be calculated. Table 4.4.1 summarizes the factors contributing to the corrected number of $\nu_\mu e \rightarrow \nu_\mu e$ events. The expression for the corrected number of $\nu_\mu e \rightarrow \nu_\mu e$ events incorporating the correction factors is

$$N_e^{corr} = \frac{(N_S + n_{e-p})(1 - f_{wh})}{A_{210\rightarrow 2100} \prod_i \epsilon_i}$$

where

$$\prod_i \epsilon_i = \epsilon_{PDT}\epsilon_{\theta<0.2}\epsilon_{eye1}\epsilon_{eye2}\epsilon_{Evtx<30}\epsilon_{e/\gamma}\epsilon_{Road}\epsilon_{\theta^2<0.03}$$

N_S	$106.5 \pm 14.6 \pm 5.0$
ϵ_{PDT}	$0.822 \pm 0.005 \pm 0.012$
$\epsilon_{\theta<0.2}$	$0.978 \pm 0.003 \pm 0.003$
ϵ_{eye1}	$0.990 \pm 0.002 \pm 0.0$
ϵ_{eye2}	$0.087 \pm 0.002 \pm 0.0$
$A_{210\rightarrow 2100}$	$0.710 \pm 0.001 \pm 0.030$
$\epsilon_{Evtx<30}$	$0.978 \pm 0.002 \pm 0.007$
$\epsilon_{e/\gamma}$	$0.91 \pm 0.01 \pm 0.02$
ϵ_{Road}	$0.924 \pm 0.010 \pm 0.011$
$\epsilon_{\theta^2<0.03}$	$0.994 \pm 0.001 \pm 0.031$
f_{wh}	$0.016 \pm 0.0 \pm 0.004$
n_{e-p}	$3.8 \pm 0.3 \pm 2.0$
N_e^{corr}	$221.9 \pm 30.0 \pm 17.2$

Table 4.4.1 Factors contributing to the corrected number of $\nu_\mu e \rightarrow \nu_\mu e$ events

After the propagation of the statistical and systematic errors the corrected number of $\nu_\mu e \rightarrow \nu_\mu e$ events is

$$N_e^{corr} = 221.9 \pm 30.0[stat] \pm 17.2[syst].$$

The statistical and systematic errors were propagated individually for each term. For each sum performed in the expression, the absolute errors for the terms involved were added in quadrature, *i.e.*

$$\epsilon_C = \sqrt{\epsilon_A^2 + \epsilon_B^2} \quad \text{for} \quad C = A + B.$$

For each product in the expression, the relative errors for the terms involved were added in quadrature, *i.e.*

$$\frac{\epsilon_C}{C} = \sqrt{(\frac{\epsilon_A}{A})^2 + (\frac{\epsilon_B}{B})^2} \quad \text{for} \quad C = A \times B.$$

Chapter 5.

Normalization

In order to determine the cross section for $\nu_\mu e \rightarrow \nu_\mu e$ scattering the total incident neutrino flux must be known. The incident neutrino flux was determined indirectly from the reaction rate for the quasi-eleastic reaction, $\nu_\mu n \rightarrow \mu^- p$ for the same experimental run which produced the signal sample. More directly, since the cross section for the quasi-elastic reaction is known from other sources [32–34], the cross section for $\nu_\mu e \rightarrow \nu_\mu e$ scattering is simply determined from the ratio of reaction rates for the signal and the normalization reaction.

In order to isolate the quasi-elastic neutrino events, the low Q^2 signature for the reaction was exploited (where Q^2 is defined as $Q^2 = -(k_\nu - k'_\nu)^2$). For low Q^2, the interactions appear in the detector as single prong events with a long forward muon track. The final state proton would not appear as a track owing to the low Q^2 constraint ($< 0.2GeV^2$). Several cuts were applied to the sample to minmize the background contributions while preserving this normalization signal. The final number of observed quasi-elastic events must be back corrected for Q^2 related acceptances and analysis inefficiences.

Into analysis from NUE	209,865
Run Kills	194,749
Microprocessor errors	187,913
Fiducial Volume	183,831
Length > 20 modules	101,217
$\theta_\mu < 20°$	59,021
Tube Cut	52,075
Prescaling (×3)	156,225

Table 5.1 Event flow for the quasi-elastic event selection

For event selection each event must have a single track topology. This reduces contributions from multi-pion reactions, understood to be the largest source of background. In addition, all events must have a track length of at least 20 modules

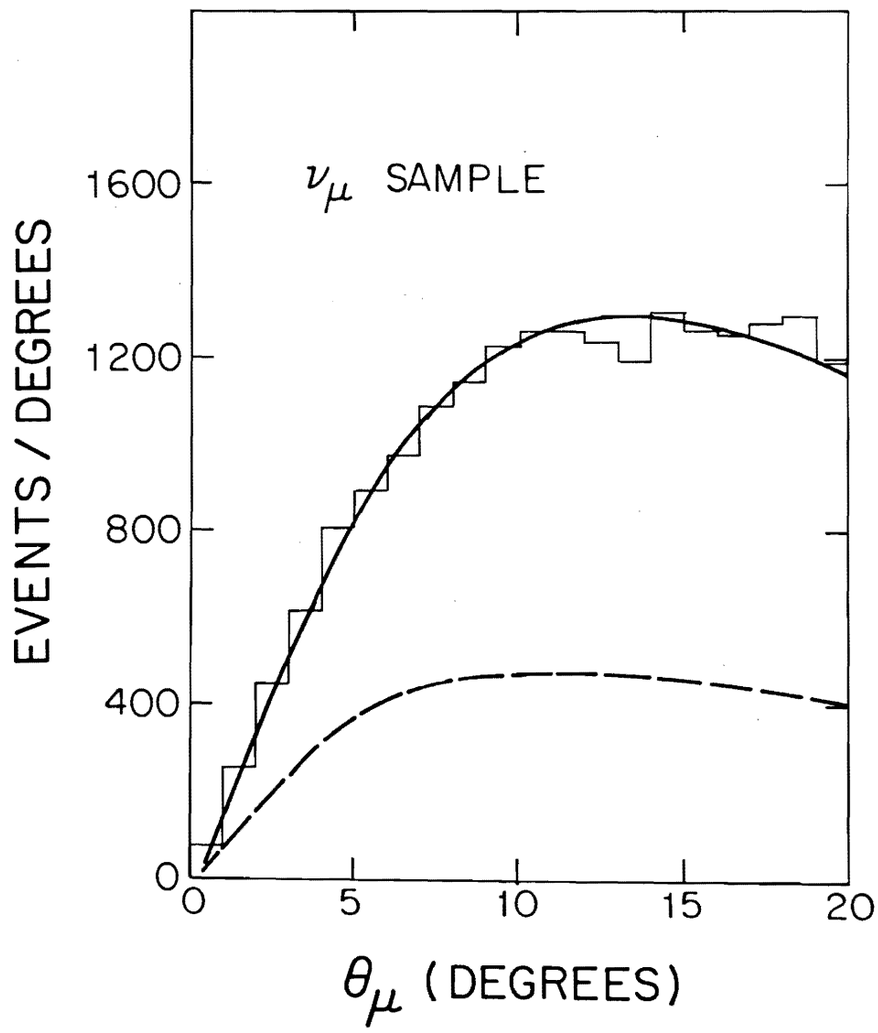

Figure 5.1 θ_μ for the normalization sample

and a track angle of less than 15° with respect to the beam direction (see Fig. 5.1). This would insure that the track was indeed a muon and not an energetic hadron. Most hadrons would range out or interact before 20 modules. Also the interaction vertex must be within the fiducial volume used in the electron analysis. This would eliminate unwanted side or front entering interactions and eliminate the need for beam profile correction when the electron sample is normalized to the quasi-elastic sample. Finally, calorimeter multiplicity and energy for the muon track were investigated to eliminate any showers or overlapping multiple track events. This was done by examining the number of hits per plane and the energy deposition per plane within a spatial cylindrical region surrounding the muon track away from the vertex. The average number of calorimeter hits per plane was required to be close to unity and the energy deposition to be consistent with that for a muon. Events with fatal microprocessor errors were removed. Any events which belonged to runs classified as having bad energy distributions were also removed. A bad energy distribuiton is any sets of runs where either the mean dE/dx or sigma for beam muons measured in modules of the detector is unstable or inconsistent from module to module. These criteria would serve to insure the validity of the information for each event. The event flow for the quasi-elastic event selection is shown in Table 5.1. The factor of 3 (prescaling) accounts for the sampling of 1 event in 3 for the normalization sampling performed by NUE. Since this sample is not statistically limited, the 1 in 3 sampling was a measure to reduce computing time and costs. The track recontruction involved in the normalization sample is the most time intensive component in NUE.

At this point it was determined that the normalization consisted mostly of quasi-elastic events (57%). The topological constraints eliminated most background channels exhibiting two or more visible tracks. However the extent of the remaining background contribution had to be determined as well as the acceptance and inefficiency effects on the quasi-elastic sample. In addition, the contribution from wrong helicity neutrinos also had to be accounted and corrected for in the normalization sample. The normalization sample could then be back corrected to

determine the actual number of quasi-elastic events. These correction factors were determined with Monte Carlo for both quasi-elastic and background events [30].

Monte Carlo events for both quasi-elastic and background events were generated. These events where then pass through NUE and the normalization selection described above. At each step in the process, the number of events that entered and the number that survived each step were counted to determine the acceptance or inefficiency correction.

Events before Subtraction	156,225
$\bar{\nu}_\mu n \rightarrow \mu^- p$ (3.5%)	5,468
Multi pion Events (4%)	6,030
$\nu_\mu p \rightarrow \mu^- p \pi^+$ (24%)	34,734
$\nu_\mu n \rightarrow \mu^- p \pi^0$ (6.9%)	9,986
$\nu_\mu n \rightarrow \mu^- n \pi^+$ (7.8%)	11,289
Total after Subtraction	88,718

Table 5.2 Normalization background subtraction

Three categories of corrections were identified. The first category were those corrections which were to account for the inefficiencies associated with NUE. This included tracking inefficiencies,and angular resolution effects, sampling losses and detector inefficiencies. The second category corresponded to the acceptance for the quasi-elastic reaction. This factor included the effects of the selection requirements used to isolate the normalization sample (i.e. angle cut, track length cut, etc.). The third category were the factors which corrected for the background events which survived the selection process to make it into the normalization sample. The background acceptances were weighted according to the value of their flux integrated cross sections and relative target populations (i.e. number of proton vs. number of neutrons). Table 5.2 shows the background subtraction for the normalization sample.

A check of the background determination was performed by examining pion decays near the event vertex in both the Monte Carlo and normalization samples. A pion decay is defined as any energy deposition near the event vertex found in

a later time cluster. The energy deposition cannot be associated with any track or interaction in that time cluster. The size of the background contribution as indicated by the presence of pion decay agreed to within 3% between the two sets. This served to verify the background prediction by Monte Carlo for the normalization sample.

Geometric Acceptance, A_{QE}	0.172
Angle Cut Efficiency, $\epsilon_{\theta<15^o}$	0.98 ± 0.02
Tracking Efficiency, ϵ_{Track}	0.85 ± 0.02
Tube Cut Efficiency, ϵ_{Tube}	0.974 ± 0.010
Processing Errors, η_{sample}	1.027

Table 5.3 Normalization correction factors

The tracking efficiency for NUE was determined by an eyescan of raw events entering the track finding procedure. The track finding efficiency represents the ability of the reconstruction program to locate and identify muon tracks within the length and angular region of interest. The inefficiency was due to several effects including PDT inefficiency, multiple scattering and noise. Table 5.3 shows the correction factors that apply to the normalization sample. Fig. 5.2 shows the systematic errors associated with the normalization [35] for both the neutrino and anti-neutrino cases. Also included is the systematic correlation between the two cases applied in the ratio.

The corrected number of quasi-elastic events is expressed as

$$N_{QE}^{corr} = \frac{N_{QE}^{obs} \times \eta_{sample}}{A_{QE} \times \epsilon_{\theta_\mu} \times \epsilon_{track} \times \epsilon_{tube}}.$$

This leads to the number

$$N_{QE}^{corr} = 6.54 \times 10^5.$$

In addition for use in the final determination of $\nu_\mu e \rightarrow \nu_\mu e$ cross section, the flux averaged cross section for $\nu_\mu n \rightarrow \mu^- p$ is determined from numerical calculation

	σ_ν	$\sigma_{\bar{\nu}}$	$\sigma_{\nu\bar{\nu}}$
νp Efficiencies			
Extra track cut	2.5%	1.1%	0%
Trackfinding	3.5%	3.3%	0%
Insufficient information	2.1%	2.2%	1%
PID	4%	4%	4%
Energy cuts	1.4%	1.3%	0%
Totals	6.4%	5.8%	4.1%
Q.E. Efficiencies			
Trackfinding	2%	2%	1%
Tube Cut	1%	1%	0%
Angle Cut	2%	2%	1%
Totals	2.9%	3.0%	1.4%
Misc. Factors			
Energy Scale	1%	1%	1%
Resolution	0%	0%	0%
Empirical background:			
$\pi - \mu$ decay	1%	.5%	.5%
Noise	2%	2%	0%
Monte Carlo:			
Nuclear Effects	4%	4%	4%
π-cross sections	3%	3%	3%
π scattering	2%	2%	2%
isospin mix	1%	1%	1%
Pauli exclusion	2%	2%	2%
Fermi momentum	0%	1%	0%
Beam spectra shape	6%	3%	2%
Wrong helicity beam contamination	0%	4%	0%
Totals	8.7%	8.1%	6.3%
Final Total	11.2%	10.4%	7.6%

Figure 5.2 Systematic errors for both the neutrino and antineutrino studies

to be

$$< \sigma_{QE} >= \frac{\int_{0.2GeV}^{5.0GeV} \sigma_{QE}(E_\nu)\phi_\nu(E_\nu)dE_\nu}{\int_{0.2GeV}^{5.0GeV} \phi_\nu(E_\nu)dE_\nu} = 0.881 \times 10^{-38} cm^2$$

for $\sin^2\theta_W = 0.225$ and the axial vector mass $M_A = 1.036$ in the theoretical quasi-elastic cross section, $\sigma_{QE}(E_\nu)$ and where $\phi_\nu(E_\nu)$ is the measured neutrino spectrum. The flux averaged neutrino beam energy is determined in a like fashion

$$< E_\nu >= \frac{\int_{0.2GeV}^{5.0GeV} E_\nu\phi_\nu(E_\nu)dE_\nu}{\int_{0.2GeV}^{5.0GeV} \phi_\nu(E_\nu)dE_\nu} = 1.28GeV.$$

Chapter 6.

Results and Conclusions

From the corrected number of electron events the total neutrino electron cross section can be calculated. A single cross section determination of the electroweak mixing parameter is performed. By combining anti-neutrino electron results[25] in the form of a ratio of cross sections, the vector and axial vector coupling constants for the electron can be determined in a model independent way. The results are shown to be consistent with the predictions of Weinberg-Salam with respect to the weak coupling constants and the electroweak mixing parameter is determined.

In addition, owing to the fine experimental angular resolution the y dependent nature of the electron θ^2 distribution can be inferred. From this, together with the value of the total cross section, a single experiment determination of the weak neutral current coupling constants for the electron can be performed. The results of this y dependent investigation are consistent with the previous two-cross section determination as well as being consistent with the predictions of Weinberg-Salam.

Finally, possible electromagnetic effects of the neutrino can be investigated as deviations of the measured cross section from the theoretical predictions of the Weinberg-Salam for a specific Weinberg angle determined from non-neutrino experiments. Gauge model predictions of the electromagnetic coupling of a magnetic moment or a charge radius for the muon neutrino are included as an additional modification to the cross section in performing least χ^2 fits of the measured cross sections to the theoretical predictions. The results of this procedure established new limits for the possible existence of a muon neutrino magnetic moment or charge radius.

1. The Cross Section

From the corrected number of neutrino electron events the cross section for neutrino electron elastic scattering can be calculated relative to the normalization reaction. The cross section, expressed in a model independent way, is

$$\sigma_{\nu_\mu e}(E_\nu) = \rho^2 \frac{G_F^2 m_e E_\nu}{2\pi}[(g_V + g_A)^2 + \frac{1}{3}(g_V - g_A)^2]$$

where $g_V = -1/2 + 2\sin^2\theta_W$ and $g_A = -1/2$ are the predictions of Weinberg-Salam. From this, a more useful form of the cross section can be expressed independent of incident neutrino energy

$$\sigma'_{\nu_\mu e} = \frac{\sigma_{\nu_\mu e}(E_\nu)}{E_\nu}.$$

The neutrino cross section can be expressed in terms of observable quantities as

$$\sigma_{\nu_\mu e}(E_\nu) = \frac{N_e}{n_e \phi_\nu(E_\nu)}$$

where N_e is the number of $\nu_\mu e \rightarrow \nu_\mu e$ events observed in the detector, n_e is the number of target electrons in the fiducial volume of the detector and $\phi_\nu(E_\nu)$ is the neutrino flux incident on the detector. The only term in this expression which is not directly known is the incident neutrino flux. However, this can be determined from the normalization reaction where the cross section is well known. The flux can then be expressed in terms of the reaction, $\nu_\mu n \rightarrow \mu^- p$ as

$$\phi_\nu(E_\nu) = \frac{N_{QE}}{n_n \sigma_{QE}(E_\nu)}$$

where N_{QE} is the number of quasi-elastic events observed in the detector, n_n is the number of target neutrons in the fiducial volume of the detector. The neutrino electron cross section can now be expressed as

$$\sigma_{\nu_\mu e}(E_\nu) = \frac{N_e}{N_{QE}} \frac{n_n}{n_e} \sigma_{QE}(E_\nu).$$

However, the values for the number of neutrino electron events and the number of quasi-elastic events are flux averaged over the entire beam energy spectrum.

To make valid use of these measured quantities, the appropriate flux averaged application of the cross section formula must be done. The energy integrated expression of the cross section becomes

$$\int \sigma_{\nu_\mu e}(E_\nu)\phi(E_\nu)dE_\nu = \frac{N_e}{N_{QE}}\frac{n_n}{n_e}\int \sigma_{QE}(E_\nu)\phi(E_\nu)dE_\nu.$$

By integrating out the energy dependence for $\sigma_{\nu_\mu e}(E_\nu)$, the cross section can be expressed as

$$\sigma'_{\nu_\mu e} = \frac{N_e}{N_{QE}}\frac{n_n}{n_e}\frac{< \sigma_{QE} >_\phi}{< E_\nu >_\phi}$$

where

$$< \sigma_{QE} >_\phi = \int \sigma_{QE}(E_\nu)\phi(E_\nu)dE_\nu$$

and

$$< E_\nu >_\phi = \int E_\nu\phi(E_\nu)dE_\nu.$$

A careful study of detector chemistry has determined the neutron to electron ratio to be $n_n/n_e = 0.794$. By combining the measured terms into the expression, the cross section is determined to be

$$\frac{\sigma_{\nu_\mu e \to \nu_\mu e}}{< E_\nu >} = (1.85 \pm 0.25[stat] \pm 0.27[syst]) \times 10^{-42} cm^2/GeV.$$

The acceptance factor, $A_{210\to 2100}$ for the electron events is dependent on the particular value of g_V and g_A. To determine g_V and g_A and $\sin^2\theta_W$ properly, the functional dependence of $A_{210\to 2100}$ must be included in the least χ^2 fits which extract $\sin^2\theta_W$ and the relational form of g_V and g_A. The functional form of the acceptance can be considered to be given by

$$A^{\nu}_{210\to 2100} = \frac{\int\int_{210<E_e<2100} dydE_\nu\phi_\nu(E_\nu)E_\nu[(g_V+g_A)^2 + (1-y)^2(g_V-g_A)^2]}{\int_0^1\int_0^\infty dydE_\nu\phi_\nu(E_\nu)E_\nu[(g_V+g_A)^2 + (1-y)^2(g_V-g_A)^2]}$$

for the neutrino case and

$$A^{\bar{\nu}}_{210\to 2100} = \frac{\int\int_{210<E_e<2100} dydE_{\bar{\nu}}\phi_{\bar{\nu}}(E_{\bar{\nu}})E_{\bar{\nu}}[(g_V-g_A)^2 + (1-y)^2(g_V+g_A)^2]}{\int_0^1\int_0^\infty dydE_{\bar{\nu}}\phi_{\bar{\nu}}(E_{\bar{\nu}})E_\nu[(g_V-g_A)^2 + (1-y)^2(g_V+g_A)^2]}$$

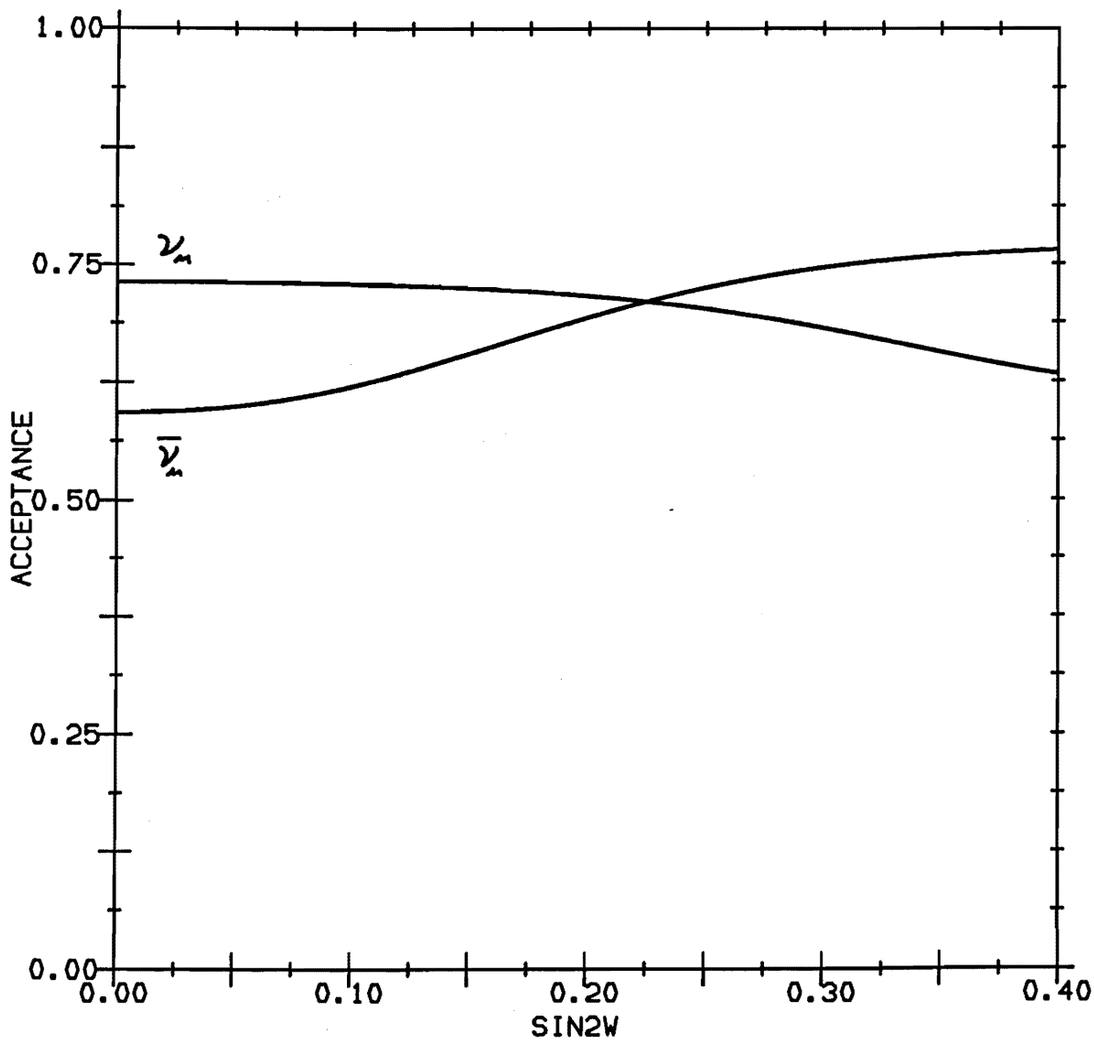

Figure 6.1.1 The acceptance, $A_{210\to 2100}$, as a function of $\sin^2\theta_W$

for the anti-neutrino case (see Fig. 6.1.1). An acceptance correction factor was determined by normalizing the energy acceptance value to the acceptance value determined by Monte Carlo at $\sin^2\theta_W = 0.225$,

$$A_{corr}(g_V, g_A) = \frac{A_{210\to 2100}(g_V, g_A)}{A_{210\to 2100}(\sin^2\theta_W = 0.225)}.$$

For accelerator energies ($E_\nu >> m_e$), $y = E_e/E_\nu$, the acceptance correction factors then by numerical integration over the neutrino beam fluxes become

$$A^{\nu}_{corr}(g_V, g_A) = \frac{1.0272(g_V + g_A)^2 + 0.2796(g_V - g_A)^2}{(g_V + g_A)^2 + 1/3(g_V - g_A)^2}$$

and

$$A^{\bar{\nu}}_{corr}(g_V, g_A) = \frac{1.0953(g_V - g_A)^2 + 0.2850(g_V + g_A)^2}{(g_V - g_A)^2 + 1/3(g_V + g_A)^2}.$$

By using the acceptance correction factors and the measured cross section, the relational form of g_V and g_A can be determined from a least χ^2 fit. The χ^2 function is expressed as

$$\chi^2 = \frac{(\sigma^{Th}(g_V, g_A) - \sigma^{Exp} \times A_{corr}(g_V, g_A))^2}{(\delta\sigma^{Exp} \times A_{corr}(g_V, g_A))^2}$$

where $\sigma^{Th}(g_V, g_A)$ is the theoretical prediction and σ^{Exp} is the experimental determination of the cross section, respectively. $\delta\sigma^{Exp}$ corresponds to the error on the experimental determination of the cross section and $A_{corr}(g_V, g_A)$ is the acceptance correction factor. The relational form is an ellipse (see Fig. 6.1.2) where the 68% confidence level contour corresponds to the region of

$$\Delta\chi^2 = 1.$$

With the predictions for g_V and g_A from Weinberg-Salam incorporated in to the χ^2 function, the electroweak mixing parameter, $\sin^2\theta_W$, is determined to be

$$\sin^2\theta_W = 0.189^{+0.032}_{-0.024}[stat]^{+0.035}_{-0.026}[syst]$$

where the statistical and systematic errors were treated separately. The resulting errors correspond to the limit of $\Delta\chi^2 = 1$. The χ^2 plot of this fit for $\sin^2\theta_W$ is shown in Fig. 6.1.3.

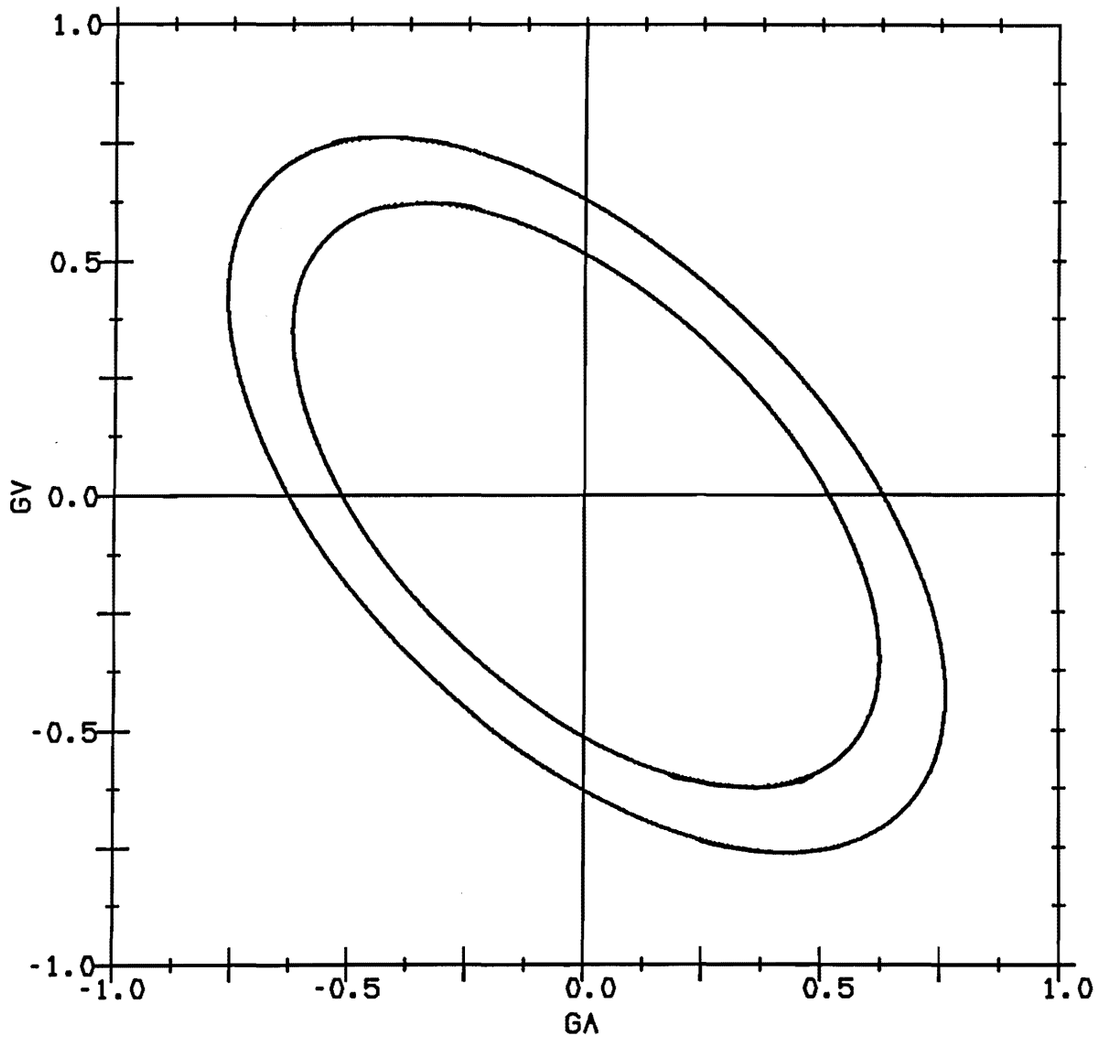

Figure 6.1.2 68% confidence level plot of g_V v. g_A for the cross section for $\nu_\mu e \rightarrow \nu_\mu e$ scattering

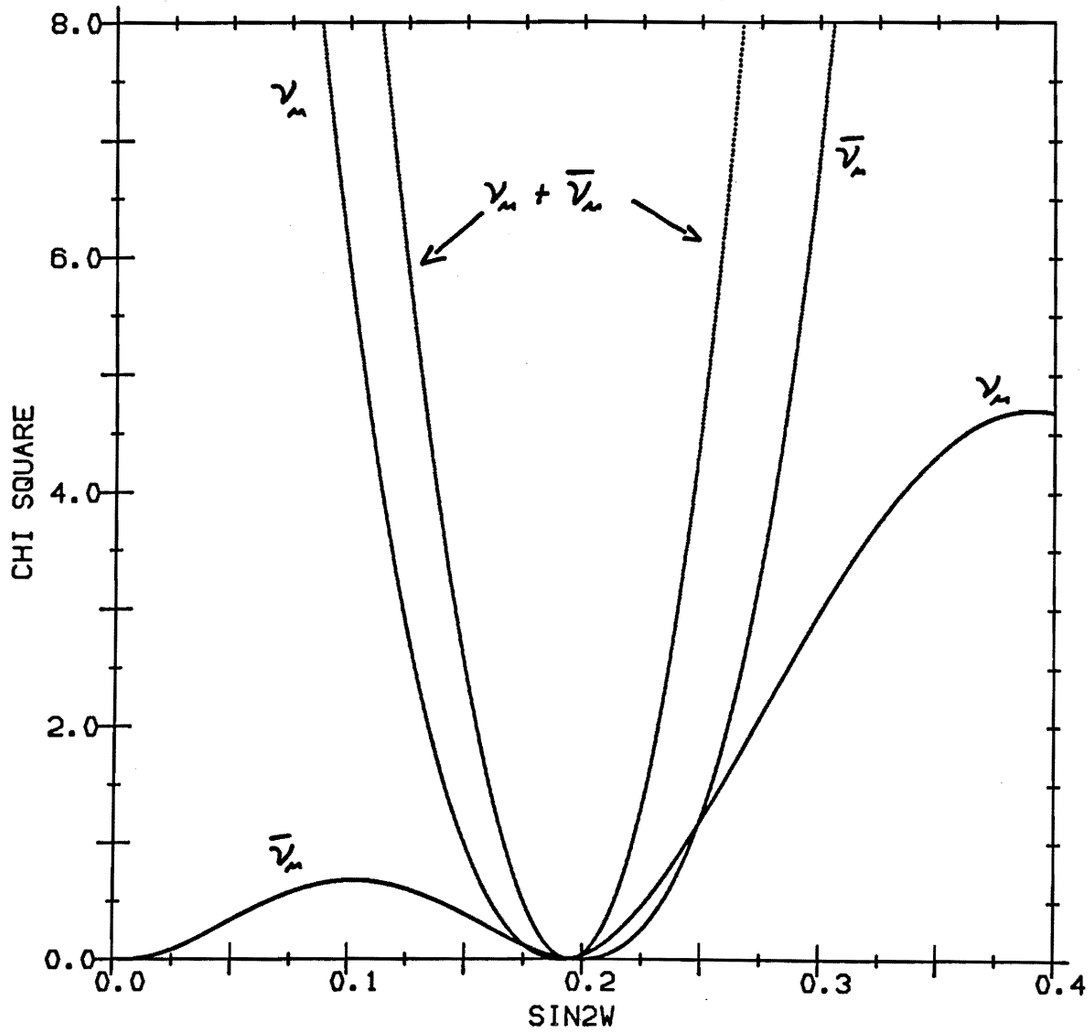

Figure 6.1.3 χ^2 plots for the fits to $\sin^2\theta_W$

2. The Ratio

By combining the results for neutrino electron elastic scattering with previous results for anti-neutrino electron elastic scattering [25] a more restrictive determination of g_V and g_A can be performed. By expressing results as the ratio of two cross sections

$$R = \frac{\sigma(\nu_\mu e \rightarrow \nu_\mu e)}{\sigma(\bar{\nu}_\mu e \rightarrow \bar{\nu}_\mu e)}$$

many advantages can be realized. The first advantage is the ratio is independent of the Z^0 coupling constant, ρ, as well as other physical constants leaving the weak coupling constants as the only parameters. Second, since the determination of each cross section was performed in a similar fashion, many systematic effects cancel thereby reducing the error in the final determination. Thirdly, the acceptable solutions for g_V and g_A are now constrained to within the intersection of the separate solutions for each cross section determination. And lastly, the error on $\sin^2\theta_W$ is less sensitive to the error on the ratio than on the individual cross sections (see Fig. 6.2.1),

$$\delta \sin^2\theta_W \approx \frac{1}{8}\frac{\delta R}{R}.$$

The ratio can be expressed in terms of g_V and g_A by the Standard Model as

$$R = \frac{(g_V + g_A)^2 + 1/3(g_V - g_A)^2}{(g_V - g_A)^2 + 1/3(g_V + g_A)^2}$$

and in terms of $\sin^2\theta_W$ as

$$R = 3\left(\frac{1 - 4\sin^2\theta_W + 16/3\sin^4\theta_W}{1 - 4\sin^2\theta_W + 16\sin^4\theta_W}\right).$$

The experimental determination of the ratio and the corresponding statistical error is straightforward. However, the systematic error determination takes some investigation. As mentioned, certain systematic effects will tend to cancel in the ratio. These systematic correlations can be isolated into two groups, those systematics associated with the corrected number of electron events and those systematics associated with the determination of the normalization.

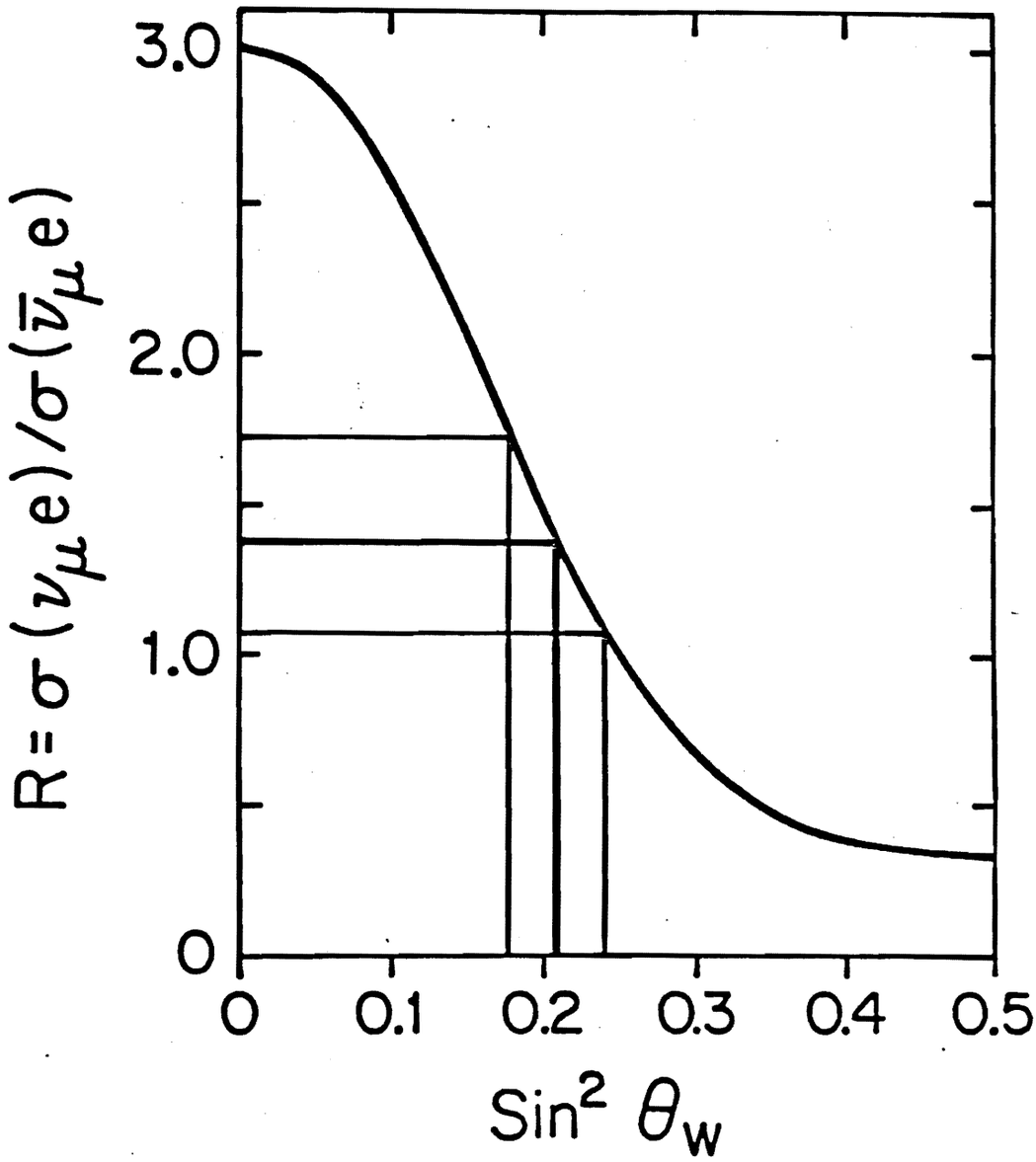

Figure 6.2.1 The Ratio v. $\sin^2 \theta_W$

Systematic Error	$\epsilon_{\nu\nu}$	$\epsilon_{\bar{\nu}\bar{\nu}}$	$\epsilon_{\nu\bar{\nu}}$
N_e	5.0	1.3	uncorrelated
ϵ_{eye1}	-	-	-
ϵ_{eye2}	-	-	-
ϵ_{PDT}	0.012	*	-
$\epsilon_{\theta<0.2}$	0.003	0.022	0.018
$A_{210\rightarrow 2100}$	0.042	0.014	0.024
$\epsilon_{Evtx<30}$	0.007	-	uncorrelated
$\epsilon_{e/\gamma}$	0.022	0.022	0.022
ϵ_{Road}	0.012	0.011	0.011
$\epsilon_{\theta^2<(0.01,0.03)}$	0.031	0.031	0.031
f_{wh}	0.004	0.01	uncorrelated
$n_{(e^-p,e^+n)}$	2.0	2.0	uncorrelated
Total	0.060	0.047	0.050

* (ϵ_{PDT} and $\epsilon_{\theta<0.2}$ are combined in $\epsilon_{\bar{\nu}\bar{\nu}}$)

Table 6.2.1 Systematic errors for the neutrino and anti-neutrino electron analysis

The first group of systematic errors stems from the individual contributions of each factor contributing to the corrected number of electron events for both the neutrino and anti-neutrino determination. Each factor in the neutrino case is checked for possible correlation in the corresponding anti-neutrino case. If the determination of each factor involved an identical procedure in the neutrino case as the anti-neutrino case, the systematics were said to be fully correlated ($\rho_{\nu\bar{\nu}} = 1$). If the procedures were different, then the systematics were considered fully uncorrelated ($\rho_{\nu\bar{\nu}} = 0$). This was repeated for all factors involved in the determination of the corrected number of electron events (see Table 6.2.1). The total systematic error associated with this group is then the appropriate convolution for correlated errors.

The second group of systematic errors arise from the determination of the number of normalization events. The determination of the level of correlation for this group was done in a procedure simliar to the first group. Term by term investigation was performed and the correlated errors tabulated (see Fig. 5.2). The ratio is then determined from a least χ^2 fit. The χ^2 function is expressed as

$$\chi^2 = \frac{(\sigma_{\nu_\mu e} - \sigma_{\bar{\nu}_\mu e} R)^2}{\delta\sigma^2_{\nu\nu} - 2\delta\sigma^2_{\nu\bar{\nu}} R + \delta\sigma^2_{\bar{\nu}\bar{\nu}} R^2}$$

where $\sigma_{\nu_\mu e}$ and $\sigma_{\bar{\nu}_\mu e}$ are the measured cross sections for $\nu_\mu e \rightarrow \nu_\mu e$ and $\bar{\nu}_\mu e \rightarrow \bar{\nu}_\mu e$ scattering, respectively. $\delta\sigma_{\nu\nu}$ and $\delta\sigma_{\bar{\nu}\bar{\nu}}$ are the experimental errors associated with the measured $\nu_\mu e \rightarrow \nu_\mu e$ and $\bar{\nu}_\mu e \rightarrow \bar{\nu}_\mu e$ cross sections, respectively. $\delta\sigma_{\nu\bar{\nu}}$ is the correlated (systematic) error associated with the two cross section determinations. The results for the ratio, R, from the χ^2 fit is

$$R = 1.60^{+0.41}_{-0.31}[stat]^{+0.19}_{-0.19}[syst]$$

where the error limits correspond to $\Delta\chi^2 = 1$.

Once the error relationships have been established, the Z^0 coupling constant ρ, the weak coupling constants g_V and g_A and the electroweak mixing parameter $\sin^2\theta_W$ could be determined from least square fit in the form

$$\chi^2 = (\,\Delta x \quad \Delta y\,)\begin{pmatrix} t_{xx} & t_{xy} \\ t_{xy} & t_{yy} \end{pmatrix}\begin{pmatrix} \Delta x \\ \Delta y \end{pmatrix}$$

where

$$\Delta x = \sigma^{Th}_{\nu_\mu e} - \sigma^{Exp}_{\nu_\mu e},$$

$$\Delta y = \sigma^{Th}_{\bar{\nu}_\mu e} - \sigma^{Exp}_{\bar{\nu}_\mu e},$$

and

$$\begin{pmatrix} t_{xx} & t_{xy} \\ t_{xy} & t_{yy} \end{pmatrix} = \begin{pmatrix} \epsilon^2_\nu & \epsilon^2_{\nu\bar{\nu}} \\ \epsilon^2_{\nu\bar{\nu}} & \epsilon^2_{\bar{\nu}} \end{pmatrix}^{-1}.$$

The elements, ϵ_ν and $\epsilon_{\bar{\nu}}$ correspond to the total errors associated with the neutrino and anti-neutrino cross sections respectively. The element, $\epsilon_{\nu\bar{\nu}}$ corresponds to the fully correlated errors between the neutrino and anti-neutrino cross sections. By performing the matrix multiplication, the form of the χ^2 becomes

$$\chi^2 = (\sigma^{Th}_{\nu_\mu e} - \sigma^{Exp}_{\nu_\mu e})^2 t_{xx} + 2(\sigma^{Th}_{\nu_\mu e} - \sigma^{Exp}_{\nu_\mu e})(\sigma^{Th}_{\bar{\nu}_\mu e} - \sigma^{Exp}_{\bar{\nu}_\mu e})t_{xy} + (\sigma^{Th}_{\bar{\nu}_\mu e} - \sigma^{Exp}_{\bar{\nu}_\mu e})^2 t_{yy}.$$

MINUIT is used to minimize the χ^2 to determine the "best" value for ρ, g_V and g_A in the theoretical expression for the respective cross sections; again with consideration for the functional dependence of the the acceptance term, $A_{210\rightarrow 2100}$ on g_V and g_A (as discussed in the previous section). The 68% C.L. χ^2 contour

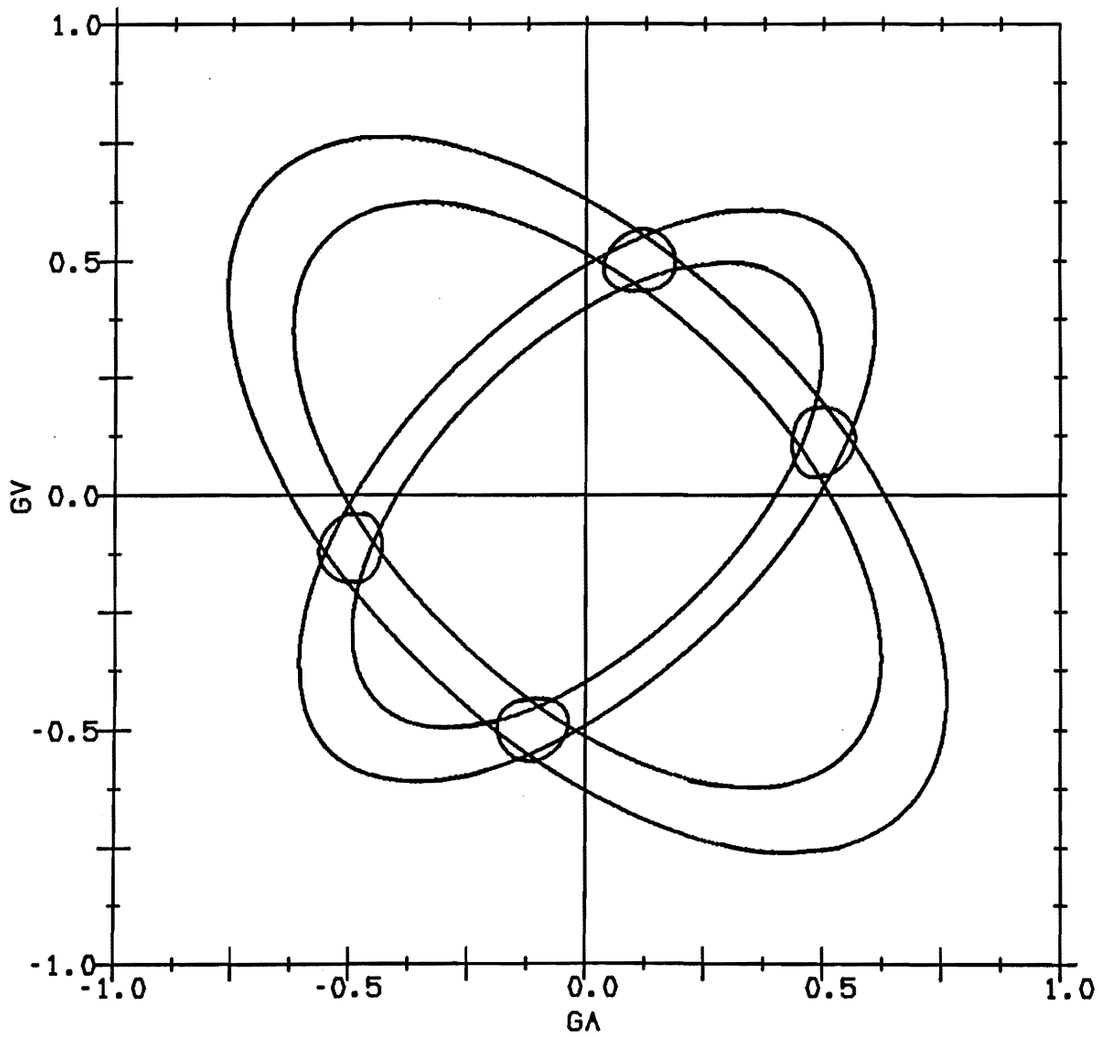

Figure 6.2.2 68% confidence level plot of g_V v. g_A for the combined cross sections for $\nu_\mu e \rightarrow \nu_\mu e$ and $\bar{\nu}_\mu e \rightarrow \bar{\nu}_\mu e$ scattering

for the combined cross sections from the fit is shown in Fig. 6.2.2 where the limits correspond to $\Delta\chi^2 = 1.65$ for two degrees of freedom. The fitting results in four possible solutions for g_V and g_A. Results from $e^+e^- \rightarrow l^+l^-$ experiments [36] eliminate two of the possible solutions and results from a $\bar{\nu}_e$ reactor experiment [37] eliminate the third possible solution. From the remaining minimized χ^2 solution, the results are

$$g_V = -0.112 \pm 0.048$$

$$g_A = -0.508 \pm 0.038$$

and

$$\rho = 0.993 \pm 0.067.$$

If the Weinberg-Salam prediction of $g_V = -1/2 + 2\sin^2\theta_W$ and $g_A = -1/2$ is applied, the electroweak mixing parameter is determined to be

$$\sin^2\theta_W = 0.192^{+0.027}_{-0.022}[stat]^{+0.015}_{-0.012}[syst].$$

The χ^2 plots of the fits to the cross sections and the ratio for $\sin^2\theta_W$ are shown in Fig. 6.1.3.

3. Y-Distribution Fits

By exploiting the shape of the angular distribution of electron events an additional constraint could be applied to the g_V g_A solutions. The differential cross section for neutrino electron elastic scattering contains two parts, a y independent (or "flat") term and a y dependent term. The terms may be expressed as follows

$$d\sigma/dy = d\sigma^{flat}/dy + d\sigma^{y}/dy$$

where

$$d\sigma^{flat}/dy \equiv \frac{G_F^2 m_e E_\nu}{2\pi}(g_V + g_A)^2$$

and

$$d\sigma^{y}/dy \equiv \frac{G_F^2 m_e E_\nu}{2\pi}(g_V - g_A)^2(1-y)^2.$$

The particular value of g_V and g_A determine the relative and absolute amounts of each term contributing to the number of neutrino electron events. By studying the angular shapes of each of these $d\sigma/dy$ terms the relative and absolute amounts each of these terms contributing to the angular distribution of neutrino electrons events can be determined. Therefore the particular values of g_V and g_A can be inferred.

To begin, Monte Carlo neutrino electron events were generated according to the respective differential cross section representing the y dependent and y independent term. Plots of the angular distribution in θ^2 are shown in Fig. 6.3.1 and Fig. 6.3.2. A least square fit was performed where each term was weighted according the particular values of g_V and g_A and combined with the background distribution and fit against the angular distribution of the data. The background distribution used was the same Monte Carlo modeled background data used in the determination of the number of signal electron events described in the previous chapter.

The y distribution fits were performed using a maximum likelihood fit. MINUIT was used to minimize the negative of the log-likelihood function to find g_V, g_A and the number of background events. The form of the log-likelihood function is

$$\ln \phi = \sum_i (n_i^{data} \ln \bar{n}_i - \bar{n}_i)$$

with

$$\bar{n}_i = \frac{G_F^2 m_e < E_\nu >_\phi}{2\pi}[(g_V + g_A)^2 n_i^{flat} A^{flat} + \frac{1}{3}(g_V - g_A)^2 n_i^y A^y] n_e + N_B n_i^B$$

where n_i^{data} is the θ^2 distribution for the data and n_i^{flat}, n_i^y and n_i^B are the θ^2 distributions for the "flat", "y" and background components. A^{flat} and A^y are the acceptances for the "flat" and "y" components, respectively.

$$< E_\nu >_\phi = \int \phi_\nu(E_\nu) E_\nu dE_\nu$$

is the flux integrated neutrino energy. n_e is the number of target electrons in the detector fiducial volume. g_V, g_A and N_B (the number of background events) are the free parameters of the fit.

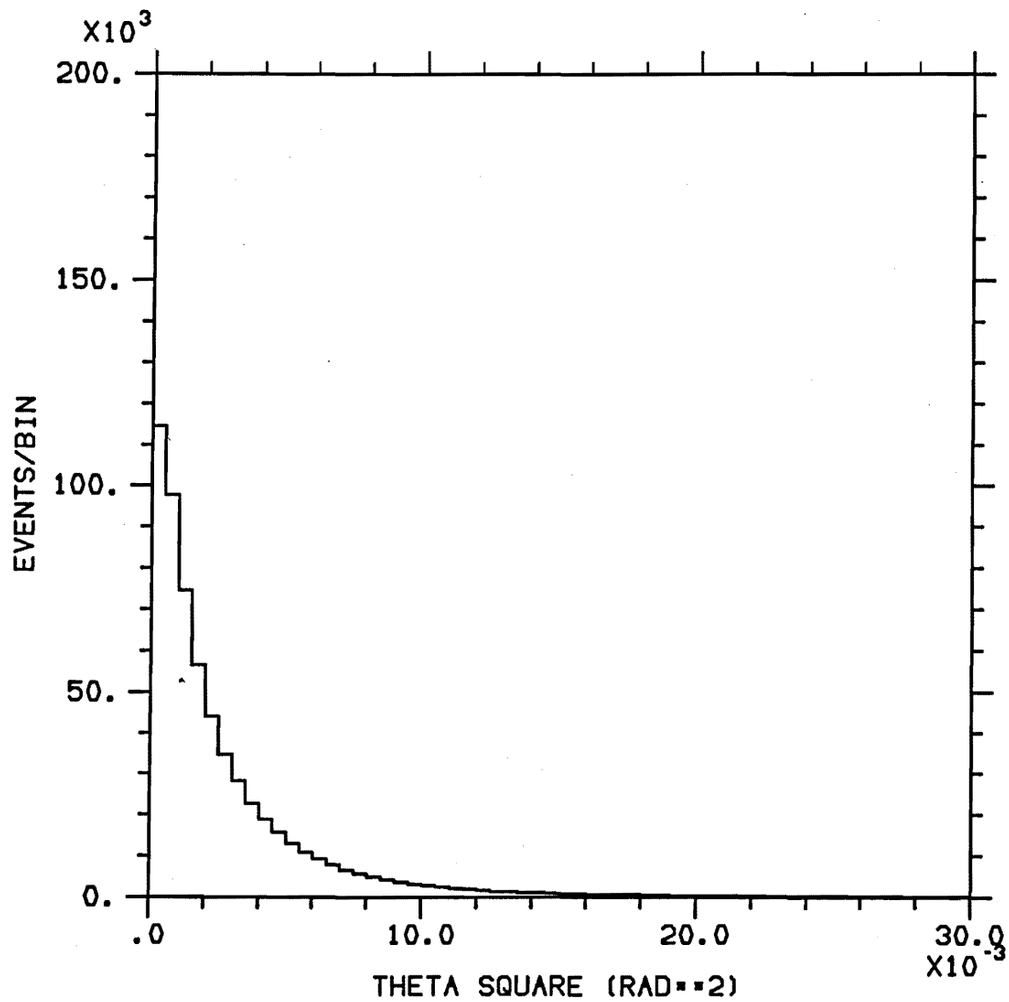

Figure 6.3.1 θ^2 distribution for the y dependent term

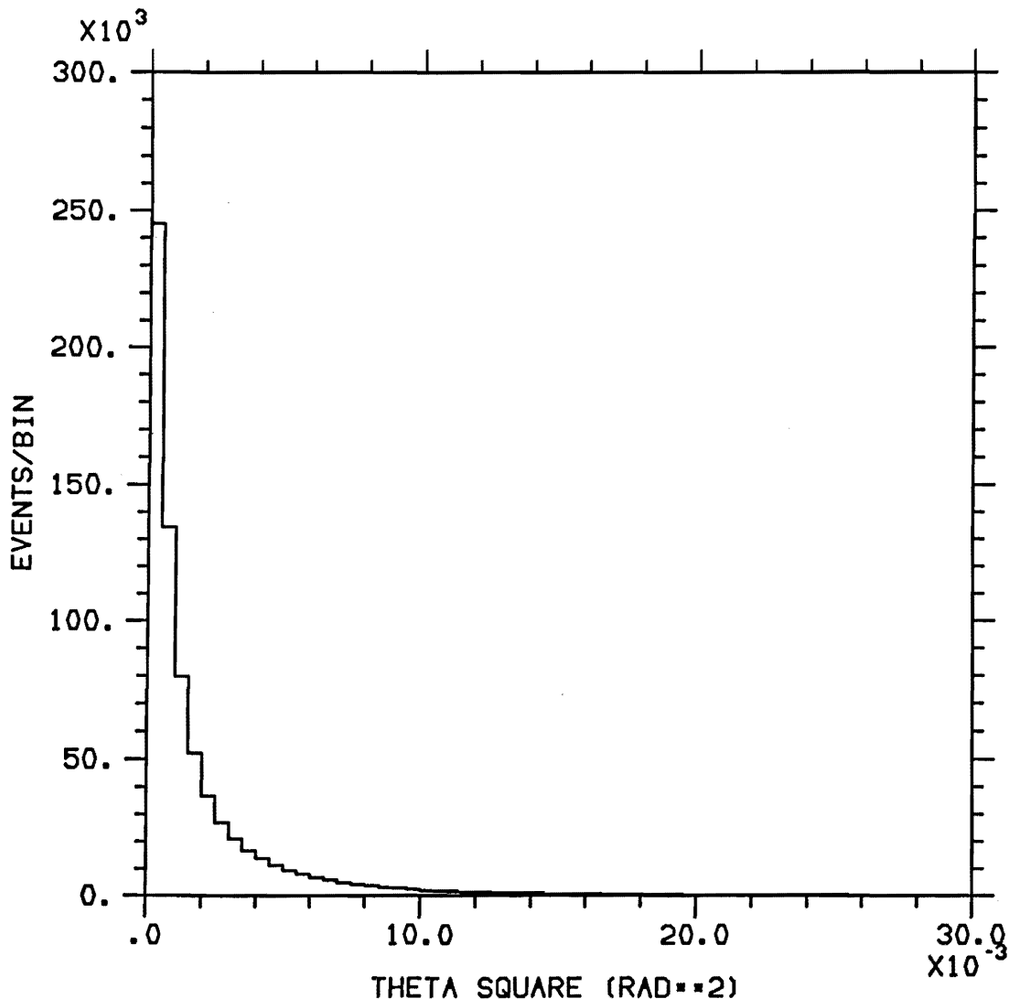

Figure 6.3.2 θ^2 distribution for the y independent term

Bins in θ^2	N^{flat}	N^y	N_e^{obs}	$\sin^2\theta_W$
15	0 ± 237	131.9 ± 18.6	131.9	0.194 ± 0.030
30	72.0 ± 44.7	51.3 ± 55.2	123.3	0.185 ± 0.028
60	89.0 ± 39.9	28.6 ± 49.5	117.6	0.184 ± 0.027

(all errors are statistical only)

Table 6.3.1 Respective contributions from "flat" and "y" components to the signal for various binnings in θ^2

Fits were performed for various binnings in θ^2. The results are summarized in Table 6.3.1 along with the Weinberg angle determined from each fit. However, to fully exploit the angular nature of this y dependence, the finest possible binning in θ^2 must be used. 60 bins in θ^2 was established as the maximum number of bins for the resolution limit in θ^2 at these energies. The results of the maximum likelihood fit for 60 bins in θ^2 is shown in Fig. 6.3.3. The resulting χ^2 contour for g_V and g_A is shown in Fig. 6.3.4 where the indicated cross corresponds to the expected value from the predictions of the standard model with $\sin^2\theta_W = 0.229$. These results are consistent with previous multi-experiment determinations of g_V and g_A.

4. Electromagnetic Effects

Several gauge theories[14,38–39] propose possible electromagnetic properties for the neutrino. The properties may manifest themselves in the form of a magnetic moment or a charge radius. The properties can then be tested for as modifications to the theoretical prediction for the cross section for neutrino interactions.

Deviations of the cross sections for $\nu_\mu e \rightarrow \nu_\mu e$ and $\bar{\nu}_\mu e \rightarrow \bar{\nu}_\mu e$ scattering from the prediction of the Standard Model for a specific Weinberg angle determined from non-neutrino experiments can be considered as limits on the existence of electromagnetic effects for the muon neutrino. These limits can be established by performing least squares fits of the electromagnetic predictions to the experimental determination of the cross sections where the free parameters are the magnitudes of the proposed magnetic moment, f and charge radius, $< r^2 >$ for the muon neutrino. If both the neutrino and anti-neutrino cases are combined, a more restrictive determination of these properties can be made.

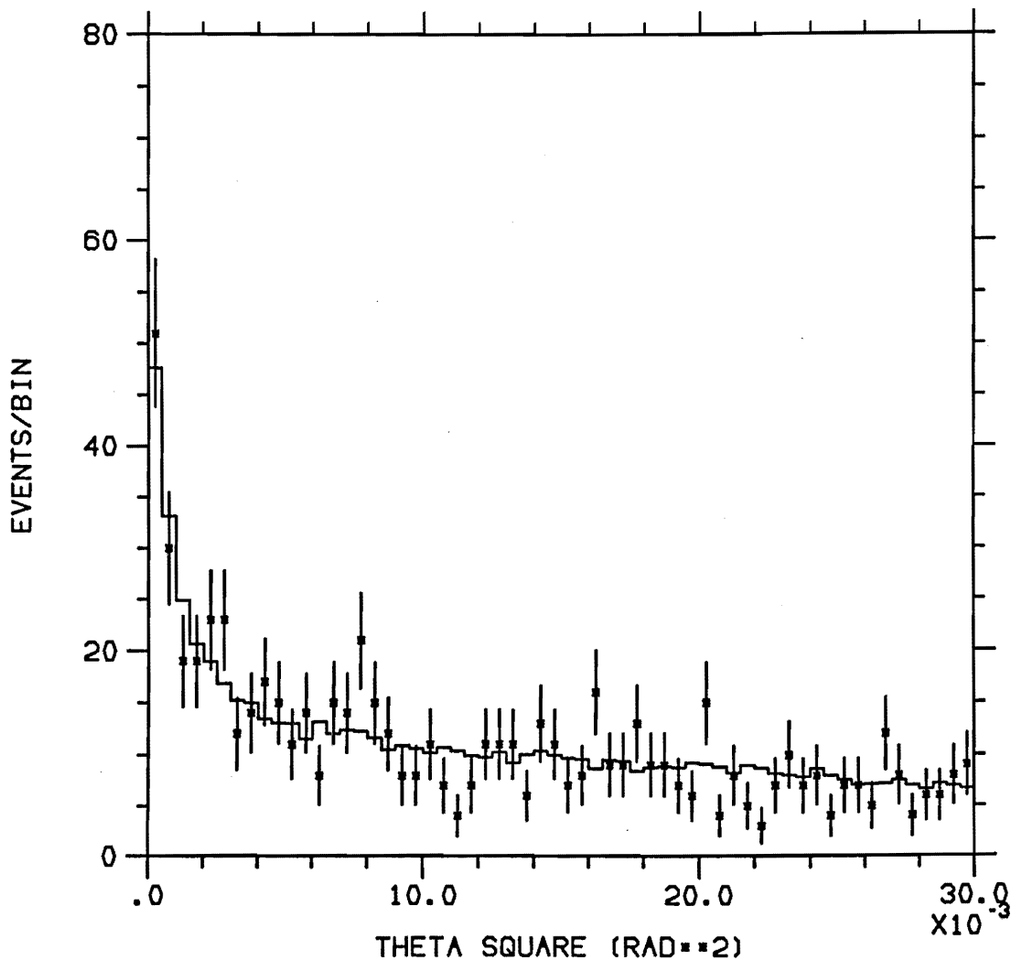

Figure 6.3.3 θ^2 fit to the data (error bars) in 60 bins with a combination of y dependent, y independent and background contributions (solid line)

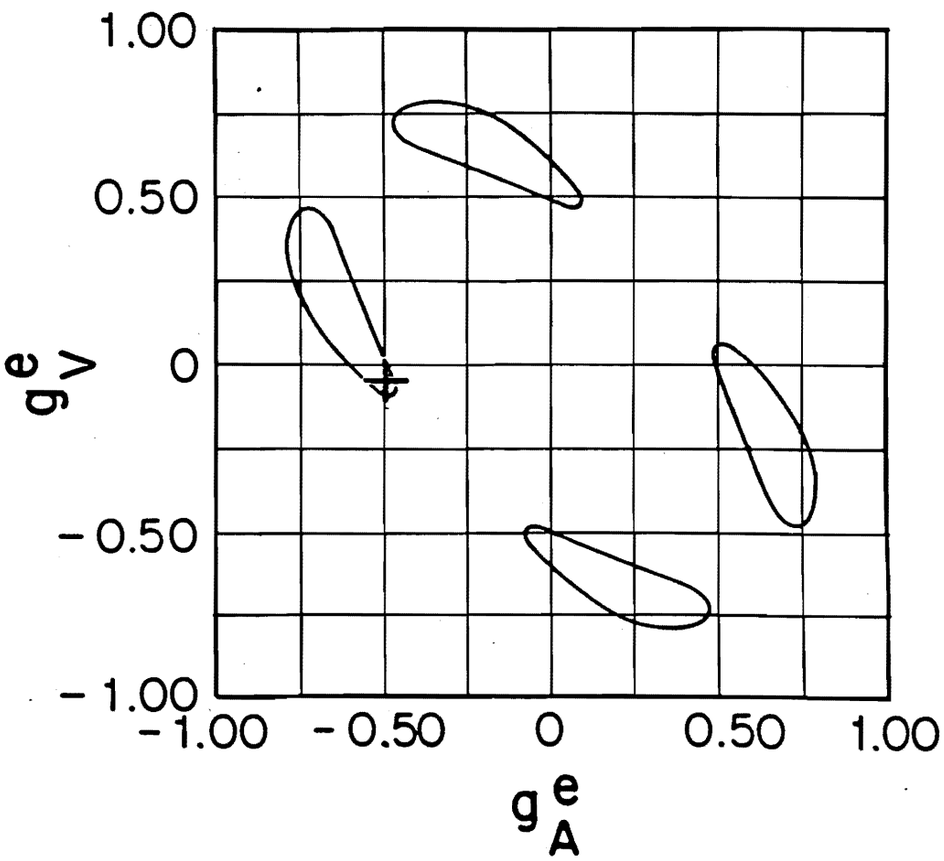

Figure 6.3.4 68% confidence level plot of g_V v. g_A for the y dependence fit

The neutrino magnetic moment is understood to manifest itself as an additive modification to the total cross section for $\nu_\mu e \rightarrow \nu_\mu e$ and $\bar{\nu}_\mu e \rightarrow \bar{\nu}_\mu e$ scattering

$$\sigma^{Th} = \sigma^{WS}(\sin^2\theta_W) + \frac{\pi\alpha^2}{m_e^2} f^2[\ln(E_\nu/E_e^{min}) - 1 + E_e^{min}/E_\nu]$$

where $\sigma^{WS}(\sin^2\theta_W)$ is the Weinberg-Salam cross section prediction without electromagnetic modifications, f is the strength of the magnetic moment for the muon neutrino and $E_e^{min} = 0.2GeV$ is the experimental low energy cut-off on the recoil electron energy. The multiplicative constant,

$$\frac{\pi\alpha^2}{m_e^2} = 2.49 \times 10^{-25} cm^2.$$

For purposes of this test, the Weinberg-Salam cross section, $\sigma^{WS}(\sin^2\theta_W)$ is evaluated at

$$\sin^2\theta_W = 0.232 \pm 0.004[stat] \pm 0.008[syst].$$

This particular value [40] of $\sin^2\theta_W$ represents the best non-neutrino determination and therefore is unbiased by possible neutrino electromagnetic effects.

The form of the χ^2 function is (as derived from a previous section)

$$\chi^2 = (\sigma^{Th}_{\nu_\mu e} - \sigma^{Exp}_{\nu_\mu e})^2 t_{xx} + 2(\sigma^{Th}_{\nu_\mu e} - \sigma^{Exp}_{\nu_\mu e})(\sigma^{Th}_{\bar{\nu}_\mu e} - \sigma^{Exp}_{\bar{\nu}_\mu e}) t_{xy} + (\sigma^{Th}_{\bar{\nu}_\mu e} - \sigma^{Exp}_{\bar{\nu}_\mu e})^2 t_{yy}$$

where the error matrices, t_{xx}, t_{xy}, t_{yy} have the same definition as indicated in previous sections. The errors indicated on $\sin^2\theta_W$ were propagated into the error matrices, but were found to not influence the results.

The expression for the χ^2 was numerically minimized by a convergent step algorithm which established the 90% confidence level limit for the magnitude of the magnetic moment, f. The 90% confidence level limit corresponds to

$$\Delta\chi^2 = 1.65.$$

A plot of χ^2 as a function of f^2 is shown in Fig. 6.4.1. The 90% C.L. limit established for the magnetic moment of the muon neutrino is

$$f < 0.95 \times 10^{-9}$$

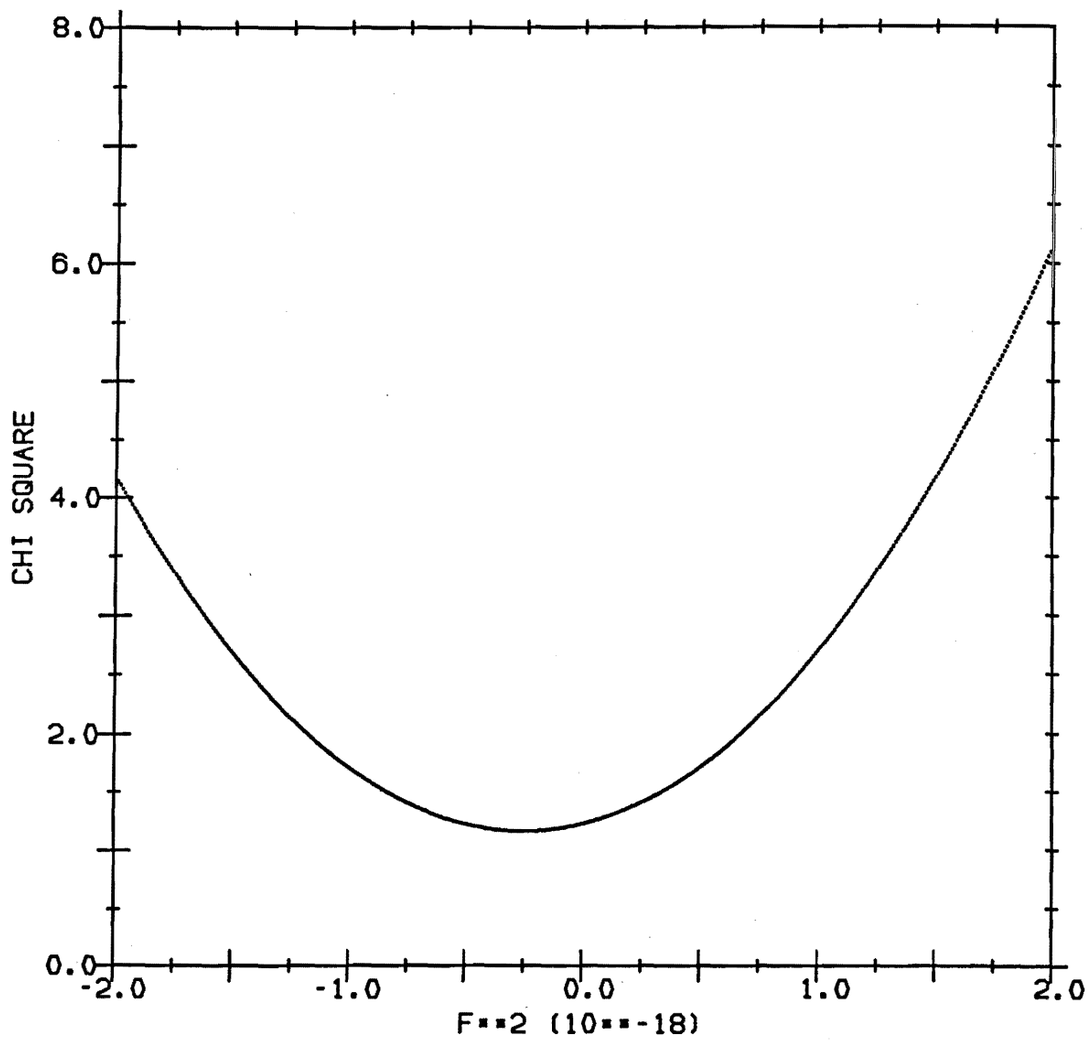

Figure 6.4.1 Plot of χ^2 v. the square of the magnetic moment, f^2

in units of Bohr magnetons.

Gauge theories[38,14] for weak and electromagnetic interactions involving neutrinos permit the replacement of the neutral intermediate vector boson, Z^0 by the photon, γ as the mechanism by which neutrinos manifest a charge radius. This can be observed in the cross section for $\nu_\mu e \rightarrow \nu_\mu e$ and $\bar{\nu}_\mu e \rightarrow \bar{\nu}_\mu e$ scattering as a modification to the electroweak mixing parameter, $\sin^2\theta_W$. The theoretical predictions for the cross sections can be expressed as

$$\sigma^{Th} = \sigma^{WS}(\sin^2\theta_W + \delta)$$

where

$$\delta = \frac{\pi\alpha}{3\sqrt{2}G_F} < r^2 >$$

and

$$\frac{\pi\alpha}{3\sqrt{2}G_F} = 1.19 \times 10^{30} cm^2.$$

Again, the value of

$$\sin^2\theta_W = 0.232 \pm 0.004[stat] \pm 0.008[syst]$$

is used in the χ^2 minimization.

The form of the χ^2 function is as before in the magnetic moment case. The minimization established the two values of the 90% confidence level limit for the charge radius. The 90% confidence level limit corresponds to

$$\Delta\chi^2 = 2.65.$$

Two values are possible since the charge radius is free to be positive or negative. The plot of χ^2 as a function of charge radius, $< r^2 >$ is shown in Fig. 6.4.2. The 90% C.L. level limts for the two values of the charge radius are, for the positive case

$$< r^2 >< 0.81 \times 10^{-32} cm^2,$$

and for the negative case,

$$< r^2 >> -7.3 \times 10^{-32} cm^2.$$

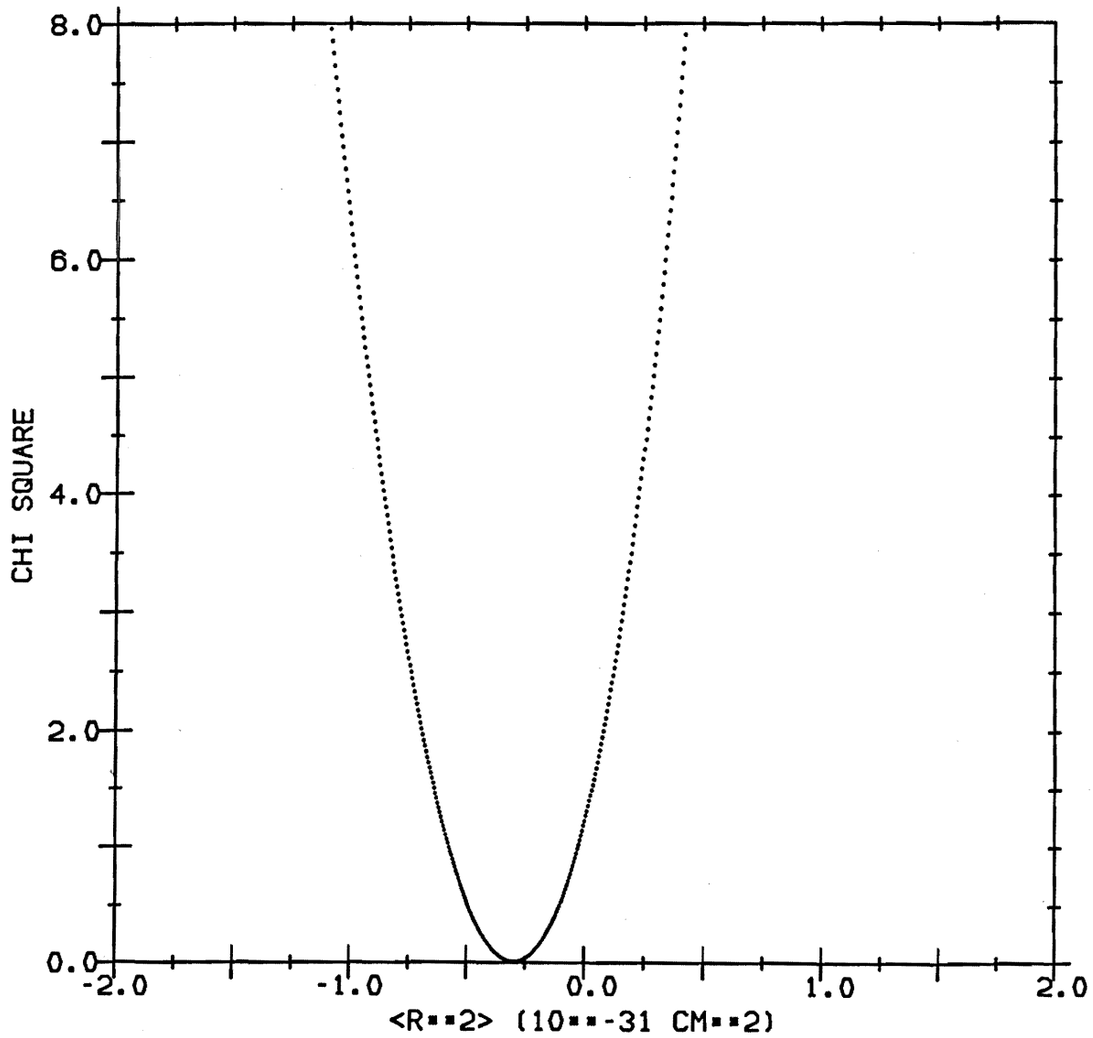

Figure 6.4.2 Plot of χ^2 v. charge radius, $< r^2 >$

Group	Beam	Total	Signal	$\sigma/E[\times 10^{-42} cm^2/GeV]$
GGM	CERN PS	1	0.7	$< 3(90\%CL)$
AC-PD	CERN PS	11	7.1	1.1 ± 0.6
GGM	CERN SPS	9	8.6	$2.4^{+1.2}_{-0.9}$
VMNOP	FNAL	46	34	1.4 ± 0.3
FMMN	FNAL	11	5.7	
E734	BNL AGS	76	51 ± 9	$1.6 \pm 0.29 \pm 0.26$*
BNL-COL	FNAL 15'	22	20.5	1.6 ± 0.4
CHARM	CERN SPS	195	83 ± 16	$1.8 \pm 0.3 \pm 0.4$
E734	BNL AGS	716	107 ± 16	$1.85 \pm 0.25 \pm 0.27$

* (previous analysis of data set)

Table 6.5.1 $\nu_\mu e \rightarrow \nu_\mu e$ cross section measurements

Group	Beam	Total	Signal	$\sigma/E[\times 10^{-42} cm^2/GeV]$
GGM	CERN PS	3	2.6	$1.0^{+2.1}_{-0.9}$
AC-PD	CERN PS	8	6.3	2.3 ± 1.1
BEBC-TST	CERN PS	1	0.5	$< 3.4(90\%CL)$
CHARM	CERN SPS	332	112 ± 21	$1.4 \pm 0.3 \pm 0.3$
E734	BNL AGS	145	52.5 ± 9.6	$1.16 \pm 0.20 \pm 0.14$

Table 6.5.2 $\bar{\nu}_\mu e \rightarrow \bar{\nu}_\mu e$ cross section measurements

Experiment	$\sin^2\theta_W$	Rad. Corr.
ATOMIC P.V. (Paris)	0.230 ± 0.030	+0.009
e^-D (SLAC)	0.218 ± 0.020	−0.010
Deep Inelastic (†)	$0.233 \pm 0.003 \pm 0.006$	−0.011
m_W, m_Z (UA1,UA2)	$0.227 \pm 0.003 \pm 0.008$	+0.016
$1 - m_W^2/m_Z^2$ (UA1,UA2)	0.218 ± 0.022	-
$\nu_\mu e, \bar{\nu}_\mu e$ (CHARM,BNL)	0.212 ± 0.023	small
$\nu_\mu p, \bar{\nu}_\mu p$ (BNL)	$0.220 \pm 0.016^{+0.023}_{-0.031}$	small
$\nu_\mu e, \bar{\nu}_\mu e$ (E734)	$0.192^{+0.027}_{-0.022}{}^{+0.015}_{-0.012}$	small
World Average	$0.227 \pm 0.003 \pm 0.006$	-

† (CDHSW,CHARM,CCFRR,FMM)

Table 6.5.3 $\sin^2\theta_W$ determinations

5. Conclusion

The cross section for $\nu_\mu e \rightarrow \nu_\mu e$ elastic scattering has been determined. Several other experiments have measured the cross sections for $\nu_\mu e \rightarrow \nu_\mu e$ and

$\bar{\nu}_\mu e \rightarrow \bar{\nu}_\mu e$ elastic scattering. The results are summarized in Table 6.5.1 and Table 6.5.2, [41]. Included are the cross section determinations from this experiment.

The weak neutral current coupling constants have been determined in a model independent way to within a four fold ambiguity. By application of the results from independent experiments, the ambiguity is removed. The results for g_V and g_A are found to be consistent with the predictions of the Standard Model where $g_V = -1/2 + 2\sin^2\theta_W$ and $g_A = -1/2$ resulting in a determination of $\sin^2\theta_W$. Determinations of $\sin^2\theta_W$ from several experiments are given in Table 6.5.3 [42] along with the estimate of the radiative correction.

A single experiment determination of the weak neutral current coupling constants has been performed utilizing the total and differential cross section for $\nu_\mu e \rightarrow \nu_\mu e$ elastic scattering. The results are consistent with the previous two-cross section determination. This represents the first time that a single experiment determination has been done.

Group	Reaction	$E_\nu[GeV]$	$x = 0.23$	$x = 0.233$	$x = 0.25$
GGM	$\bar{\nu}_\mu e$	2.0	7.43	7.42	7.37
AC-PD	$\bar{\nu}_\mu e$	2.0	2.89	2.87	2.78
GGM	$\nu_\mu e$	2.2	2.84	2.85	2.96
AC-PD	$\nu_\mu e$	2.2	1.15	1.19	1.36
E734	$\nu_\mu e + \bar{\nu}_\mu e$	1.3		0.95	

(units of $\times 10^{-9}$ Bohr magnetons)

Table 6.5.4 Upper bound determinations for the magnetic momnet

A limit has been established for the upper bound on the magnetic moment and charge radius for the muon neutrino. Determinations on the upper bound for the magnetic moment from this and several other experiments are given in Table 6.5.4[16] for various values of $\sin^2\theta_W$. Astrophysical arguments[43] imply,

$$f < 8.5 \times 10^{-11}$$

(for $m_{\nu_\mu} < 10keV$), while gauge theories establish upper limts of

$$f < 5.4 \times 10^{-12}$$

for the magnetic moment[44] and

$$< r^2 > \sim 10^{-33} - 10^{-34} cm^2$$

for the charge radius[45].

Appendix 1.

Eyescan Rules

The following is a summary of the rules followed for each eyescan.

6. First Eyescan Rules

Shower definition - A "good" shower is a forward electromagnetic shower with a "clean" vertex. A "good" shower should not look hadronic or have kinks. Do not use any energy, angle of fiducial volume criteria for the first scan.

While scanning, use the above definition and follow this algorithm:
Is there a "good" shower in the events?

Yes - continue

No - go to next event

Is the shower associated (points back to a common point) with any interaction greater than 3 modules in size?

Yes - if shower is associated with another shower, mark off 9 (gamma event); go to next event

No - continue

Is the shower larger than 6 modules and clean ("no kinks")?

Yes - mark off 1,3

No - mark off 2,4

Is the shower associated with any interaction less than or equal to 3 modules in size?

Yes - if up stream mark off 5 (stub up), if down stream mark off 6 (stub down)

No - continue

Is there a short track (less than 10 modules) coming from the vertex of the shower?

Yes - mark off 8 (ep event)

No - continue

Is there an unassociated interaction (muon or track) in the event?

Yes - mark off 7 (2 in 1 event); go to next event

No - go to next event

Summary of flag codes:

1,3 - good, large electromagnetic shower

2,4 - poor, small electromagnetic shower

5 - up stream stub

6 - down stream stub

7 - 2 in 1 event

8 - e^-p event

9 - 2 gamma event

7. Second Eyescan Rules

Shower definition - A "good" shower is deined as any forward electromagnetic shower (non-hadronic, no kinks) with a "clean" vertex (no extra prongs, no extra hits) satisfying the following fiducial and energy constraints

$$4 < X_{PDT} < 53$$

$$4 < Y_{PDT} < 53$$

$$3 < Z_{MOD} < 101$$

$$E_{cal1} < 60MeV$$

$$E_{cal2} < 60MeV$$

$$E_{tot} > 100MeV.$$

Kept Events:

Any "good" shower event not failing the listed criteria with no associated interactions should be flagged with CODE 1 ("Keep Event") and its vertex noted. (CODE 1 is exclusive with CODE 3.)

Need Study Events:

Any shower event with "substantial" bad energy information (e.g. "***") or

with another "event" (muon, etc.) in the same time cluster which will "complicate" the shower event (e.g. no clear separation) should be flagged with CODE 2 ("Needs Study").

Good Stub Events:

Any shower event with an associated (both views) up stream stub (at least one calorimeter hit of greater than 5 MeV and one PDT hit) within 20 modules of the shower vertex should be flagged as a photon with CODE 3 ("Good Stub") and its vertex noted. (CODE 3 is exclusive with CODE 1.)

Extra Up Stream Energy:

Any shower event with unassociated extra up stream energy within 20 modules of the vertex should be flagged with CODE 4 ("Extra Up").

Extra Down Stream Energy:

Any shower event with extra down stream energy outside of the shower "road" and within 20 modules of the vertex should be flagged with CODE 5 ("Extra Down").

2 in 1 Events:

Any shower event with an unassociated "activity" of greater than 2 calorimter calls (e.g. tracks, interactions, noise) anywhere in the event frame should be flagged with CODE 6 ("2 in 1").

Appendix 2.

Monte Carlo

Many effects in the experiment, such as acceptance or detection efficiency, could not be directly measured. However, their determination is necessary for complete analysis of the data. To study and quantify these effects, Monte Carlo generated events were used. The Monte Carlo events served as a controlled sample by which theses complicated effects could be scrutinized.

The production of Monte Carlo events is divided into two parts. The first part involves the generation of events consistent with the distribution of neurino flux, theorectical differential cross sections and target nuclei properties. From this generation, the four vectors of all particles involved in the reaction are known.

The second part of Monte Carlo production involved the translation of all particle four vectors for each event into a simulated hit pattern in the detector. Knowledge of detector materials and geometery is used to produce a hit pattern with energies and times representative of the reaction particles moving through the detector. In addition, ionization effects and nuclear scattering as well as measured resolution functions are also included in the translation of the reaction particles within the detector. The output format of the Monte Carlo production is in a format compatible with the raw data format. The Monte Carlo events could then be analyzed with the same analysis programs used for real data. This enables the study and evaluation of analysis performance with events of known kinematics. A detailed discription on the Monte Carlo is contained in Ref. 46.

References

1. Reines,F. and Cowan,C.L., Phys. Rev. **90**, 493, (1953).

2. Reines,F. and Cowan,C.L., Phys. Rev. **113**, 273, (1954).

3. Weinberg,S., Phys. Rev. Lett. **19**, 1264, (1967).

4. Salam,A., *Elementary Particle Theory*, ed. N.Svartholm, Almqvist and Wiksell, Stockholm, (1968).

5. Glashow,S.L., Nucl. Phys. **22**, 579, (1961).

6. t'Hooft,G., Nucl. Phys. **B35**, 167, (1971).

7. Hasert,F.J., *et al.*, Phys. Lett. **46B**, 138, (1973).

8. Bagnaia,P., *et al.*, Phys. Lett. **129B**, 130, (1983).

9. Arnison,G., *et al.*, Phys. Lett. **129B**, 273, (1983).

10. Georgi,H. and Glashow,S.L., Phys. Lett. **33**, 438, (1974).

11. Commins,E.,D. and Bucksbaum,P.H., *Weak interactions of leptons and quarks*, Cambridge University Press, Cambridge, (1983).

12. Kim,J.E., *et al.*, Rev. Mod. Phys., **53**, 211, (1981).

13. t'Hooft,G., Phys. Lett. **37B**, 195, (1971).

14. Grau,A. and Grifols,J.A., Phys. Lett. **166B**, 233, (1986).

15. Kim,J.E., Mathur,V.S. and Okubo,S., Phys. Rev. **D9**, 3050, (1974).

16. Kyuldjiev,A.V., Nucl. Phys. **B243**, 387, (1984).

17. Weng,W.T., Procedings of Particle Accelerator Conference, Santa Fe, N.M., (1983); Weng,W.T. *et al.*, BNL Report 51310 (1979).

18. Palmer,R., Procedings of an Informal Conference on Experimental Neutrino Physics, CERN, 1965 (ed. by C.Franzinetti).

19. L. A. Ahrens, *et al.*, *Precise Determination of the Neutrino Fluxes in the Brookhaven Wide Band Beams*, Phys. Rev. **D34**, 75 (1986).

20. L. A. Ahrens, *et al.*, Phys. Rev. **D31**, 2732 (1985).

21. Ahrens, L. A.,*et al.*, *A Massive Fine-Grained, Detector for the Elastic Reactions Induced by Neutrinos in the GeV Energy Region*, Nucl. Instr. & Meth. subm.

22. Sauli, F., *Principles of Operation of Multiwire Proportional and Drift Chambers*, CERN 77-09, May 1977; Wilkinson, Denys Haigh,"Ionization Chambers and Counters", Cambridge University Press 1950.

23. See Program Notes PN97, PN98, PN100, Fermilab Computer Department.

24. Connolly, P. L. and Cutts, D., "The Use of Microprocessors in a Neutrino Experiment", Proc. of the CERN Topical Conference on the Applications of Microprocessors to High Energy Physics Experiments, CERN, Geneva, Switzerland, May, 1981 (unpublished).

25. Hurley, M. B., Ph.D. thesis, University of Pennsylvania, (1984) unpublished.

26. Ahrens, L. A., *et al.*, Measurement of the cross section of $\nu_\mu e \rightarrow \nu_\mu e$, Phys. Rev. Lett. **51**, 1514, (1983).

27. Tatsumi,S., Ph.D. Thesis, Osaka University (1984), unpublished.

28. Ahrens, L. A., *et al.*, Measurement of the ratio of cross sections for neutrino and anti-neutrino scattering from electrons, Phys. Rev. Lett. **54**, 18, (1985).

29. Hughlock,B.W. Ph.D. Thesis, Brown University (1983), unpublished.

30. Rein, D. and Sehgal, L. M., Neutrino-Excitation of Baryon Resonances and Single Pion Production, Annals of Phys., **133**, 79, (1981).

31. James, F. and Ross, M., Computer Physics Communications, **10**, 343, (1975).

32. Llewellyn-Smith, C. H., Phys. Rep. **3C**, 261, (1972).

33. Barnett, R. M., Phys. Rev. **D15**, 97, (1977).

34. Baker,N.J., *et al.*, Phys. Rev. **D23**, 2499, (1981).

35. Ahrens,L.A., *et al.*, Phys. Rev. D, subm. 6/86.

36. Panman,J., Rappoteur's talk, Proc. Neutrino '84, Dortmound, (1984) to be published.

37. Reines,F., Gurr,H.S., and Sobel,H.W., Phys. Rev. Lett. **37**, 315, (1976).

38. Beg,M.A.B., Marciano,W.J., Ruderman,M., Phys. Rev. **D17**, 1395, (1978).

39. Grosser,D., Phys. Lett. **166B**, 340, (1986).

40. Roussarie,A., XII Int. Conf. on High Energy Phys. Berkeley, 1986.

41. Murtagh,M.J., "Review of Neutrino-Electron and Antineutrino-Electron Elastic Scattering Experiments", talk given at NEUTRINO '84, XIth International Conf. on Neutrino Physics and Astrophysics, Nordkirchen, FRG (1984).

42. Altarelli,G., Talk presented at the 23rd Int. Conf. on High Energy Physics, Berkeley, (1986).

43. Sutherland,P., Ng,J.N., Flowers,E., Ruderman,M. and Inman,C., Phys. Rev. **D13**, 2700, (1976).

44. Beg,M.A., Marciano,W.J. and Ruderman,M., Phys. Rev. **D17**, 1395, (1978).

45. Kim,J.E., Phys. Rev. **D14**, 3000, (1976); Marciano,W.J. and Sanda,A.I., Physc. Lett. **67B**, 303, (1977).

46. Stern, E. G., Ph.D. thesis, State University of New York at Stonybrook, (1986), unpublished.